Suppression of exciton quenching in organic semiconductor devices

井上, 棟智

https://doi.org/10.15017/1654827

出版情報：九州大学, 2015, 博士（工学）, 課程博士
バージョン：
権利関係：全文ファイル公表済

2015

Doctor thesis

Suppression of exciton quenching in organic semiconductor devices

Munetomo Inoue

Department of Chemistry and Biochemistry
Graduate School of Engineering
Kyushu University

Table of contents

Chapter 1

Introduction to this thesis

Chapter 2

Effect of reverse intersystem crossing on exciton annihilation in organic light-emitting diodes with thermally-activated delayed fluorescence emitters

Chapter 3

Incorporation of oxygen into organic thin films with the aim of suppressing singlet-triplet annihilation

Chapter 4

Low amplified spontaneous emission threshold and suppression of singlet exciton quenching in layers doped with ter(9,9’-spirobifluorene)

Chapter 5

Chapter 1

Introduction to this thesis

1-1. Background and motivation

Since the two-layer structure for organic light-emitting diodes (OLEDs) was reported by C. W. Tang and S. A. VanSlyke [1], OLED performance has been rapidly improved, leading to the realization of OLEDs that reached the theoretical maximum internal quantum efficiency (η_{IQE}) of 100% [2]. OLEDs have many attractive advantages such as a wide variety of emission wavelengths in the visible region, low power consumption, high contrast, fast response, mechanical flexibility, and solution processability [3], making it possible to fabricate thin, light, and flexible displays and lighting at low cost.

Figure 1-1 shows the basic structure of an OLED, containing three organic layers sandwiched between a cathode and an anode under electrical operation. The organic region is generally composed of several organic layers with different functions, for example, a hole-transport layer, an emitting layer, and an electron-transport layer. When a high electric field is applied between the cathode and the anode, holes are injected from the anode into the organic hole-transport layer and electrons are injected from the cathode into the organic electron-transport layer. Injected holes and electrons are transported to the emitting layer, where the electrons and holes recombine to generate molecular excitons for emission.

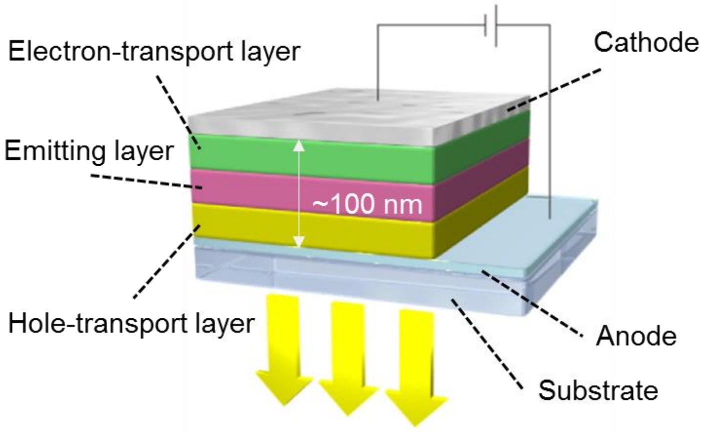

Figure 1-1. Schematic illustration of an OLED structure. (This picture was obtained from the web page of Adachi laboratory: http://www.cstf.kyushu-u.ac.jp/~adachilab/).

Figure 1-2(a) illustrates the emission mechanisms of OLEDs. Three-times as many triplet excitons (75%) as singlet excitons (25%) are generated after recombination of injected electrons and holes in OLEDs because of the law of spin statistics [4,5]. For OLEDs using fluorescent materials, η_{IQE} is intrinsically limited to 25% because only 25% of excitons that are generated as singlets are harvested to emit light under electrical excitation [4,5]. In contrast, phosphorescent materials such as tris(2-phenylpyridinato)iridium(III) [Ir(ppy)$_3$] show efficient room-temperature phosphorescence on the basis of an efficient heavy atom effect, providing nearly a 100% η_{IQE} because both singlet and triplet excitons can be harvested [6]. Recently, Adachi's group proposed a unique triplet harvesting process in OLEDs, namely, thermally activated delayed fluorescence (TADF) [7-9]. In OLEDs using TADF molecules as emitters (TADF-OLEDs), a maximum η_{IQE} of nearly 100% has been achieved without rare metals through efficient reverse intersystem crossing (RISC).

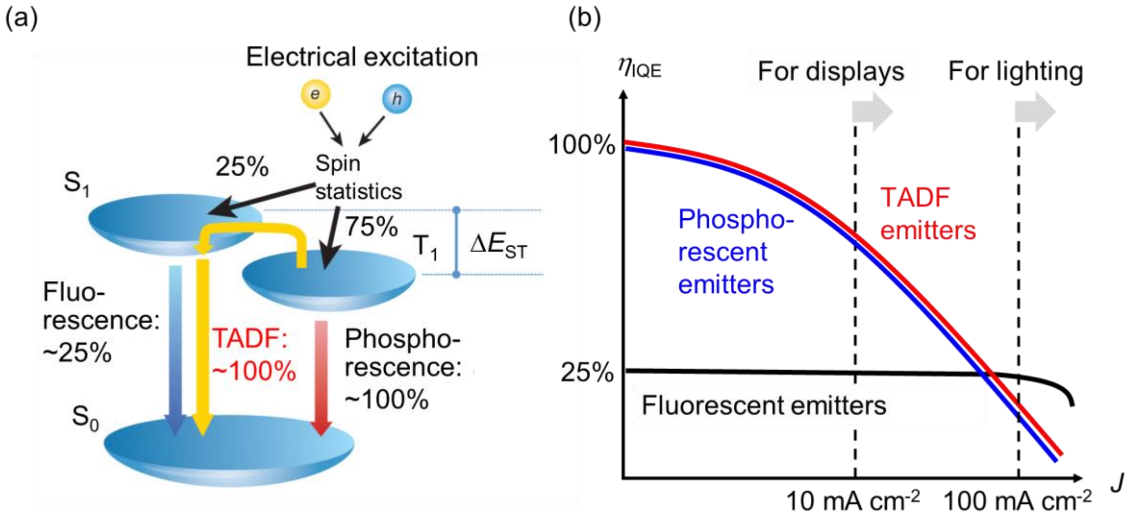

Figure 1-2. (a) Emission mechanisms of three types of OLEDs (fluorescence OLEDs, phosphorescence OLEDs, and TADF-OLEDs) and (b) illustrations of efficiency roll-off of the OLEDs. S_1, T_1, S_0, and ΔE_{ST} stand for a lowest singlet excited state, lowest triplet excited state, singlet ground state, and energy gap between S_1 and T_1, respectively. The illustration of (a) was obtained from reference [7].

In all OLED types, a rapid decrease in external quantum efficiency (η_{EQE}) is observed as current increases [Fig. 1-2(b)] because of singlet-triplet annihilation (STA), singlet-polaron annihilation (SPA), triplet-triplet annihilation (TTA), triplet-polaron annihilation (TPA), carrier imbalance, electric-field induced exciton quenching, and singlet-heat quenching (SHQ) [10-16]. The mechanisms of STA, SPA, TTA, and TPA are shown in Fig. 1-3 [12-17]. In STA and TTA, a singlet or a triplet exciton is quenched by a triplet exciton through Förster or Dexter energy transfer. In SPA and TPA, a singlet or a triplet exciton is quenched by a polaron through Förster energy transfer. In general, roll-off characteristics of fluorescence-based OLEDs are weaker than those of phosphorescence and TADF-OLEDs, although their maximum η_{IQE} and η_{EQE} are lower than those of phosphorescence and TADF-OLEDs [2,4,6,7,9,10,15,18,19]. On the other hand, much stronger roll-off is observed in phosphorescence and TADF-OLEDs due to longer triplet exciton lifetime than singlet exciton lifetime [2,4,6,7,9,10,15,18,19]. Efficiency roll-off has been ascribed to mainly TTA in OLEDs containing $Ir(ppy)_3$ as a phosphorescent emitter [15,20] and STA and TTA in TADF-OLEDs [7,9,19], although the detailed quenching mechanisms are still under investigation. Efficiency roll-off at high current density is one of the crucial problems for high-bright lighting OLEDs in terms of power consumption and device lifetime [15,18] and, therefore, needs to be suppressed for the further development of OLEDs.

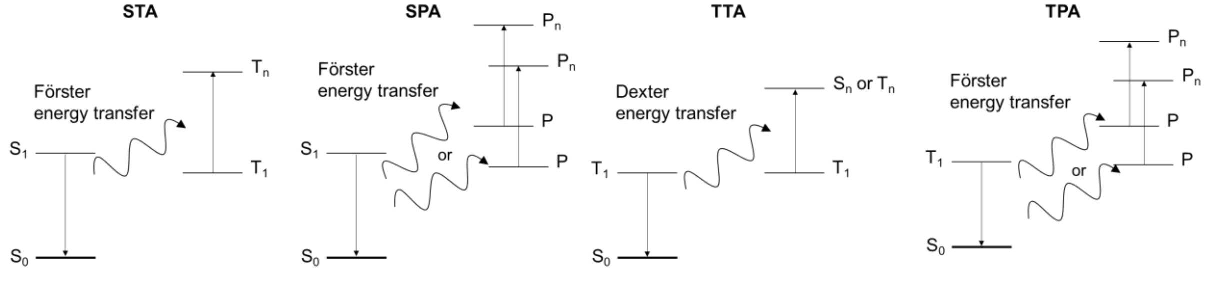

Figure 1-3. The mechanisms of STA, SPA, TTA, and TPA [12-17].

Figure 1-4 shows relationships between the intramolecular relaxation and quenching processes using rate constants. Here, k_r, k_{nr}, k_{ISC}, k_{RISC}, k_r^T, k_{nr}^T, k_{STA}, k_{SPA}, k_{TTA}, k_{TPA}, and k_q represent the rate constants of radiative emission from a lowest singlet excited state (S_1) to a ground state (S_0), non-radiative decay from S_1 to S_0, intersystem crossing (ISC) from S_1 to a lowest triplet excited state (T_1), RISC from T_1 to S_1, radiative emission from T_1 to S_0, non-radiative decay from T_1 to S_0, STA, SPA, TTA, TPA, and quenching by electric field and Joule heating. N_T and N_P are the densities of triplet excitons and polarons. It can be found in Fig. 1-4 that the quenching rates of STA (k_{STA} N_T), SPA (k_{SPA} N_P) TTA (k_{TTA} N_T), and TPA (k_{TPA} N_P) are in proportional to the densities of quenching species (triplet excitons and polarons in this case) and compete with the intramolecular relaxation processes, indicating that a reduction of quenching species and enhancement of intramolecular relaxation are very important to suppress the quenching processes.

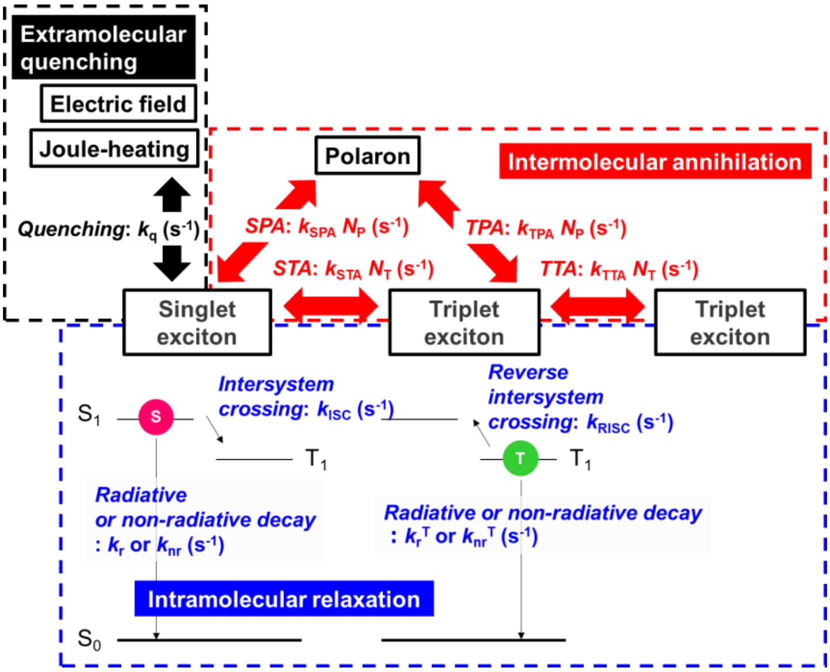

Figure 1-4. Relationships between the intramolecular relaxation and quenching processes. The quenching and intramolecular relaxation processes compete each other.

Table 1-1 summarizes the history of lasing and amplified spontaneous emission (ASE) from organic materials. Since the first observation of optically pumped lasing and continuous-wave (CW) lasing from organic solutions containing organic laser dyes in 1966 and 1970, organic dye lasers have been rapidly progressed and applied for analytical sources and medical uses [21,22]. After that, lasing from organic solid-state films was firstly demonstrated under optical pulse pumping in 1996 [23]. Optically pumped quasi-CW lasers from organic solid-state films was realized in 2006 [24]. In 2008, LED pumped lasing from organic solid-state films was demonstrated [25]. In the background of the above optically pumped organic lasers, the realization of electrically pumped organic semiconductor laser diodes (OSLDs) has been strongly desired.

Table 1-1. History of organic lasers and progress for the realization of OSLDs.

History of optically pumped organic lasers	Progress for the realization of OSLDs		
	(1) Reduction of ASE or lasing threshold	(2) Injection of high current density into OLEDs	(3) Suppression of efficiency roll-off at high current density
1966 [21] First observation of lasing from organic solutions 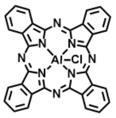 **1970 [22]** CW-lasing from organic solutions 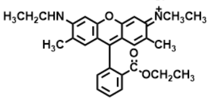 **1996 [23]** Lasing from organic solid state films 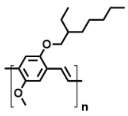 **2006 [24]** Quasi-CW lasing from organic solid state films 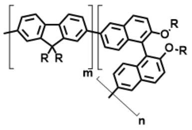 **2008 [25]** LED pumped lasing from organic solid state films 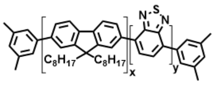	**2005 [26]** 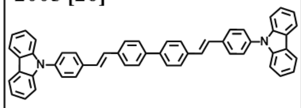 BSB-Cz: 0.32 μJ cm^{-2} **2007 [27]** 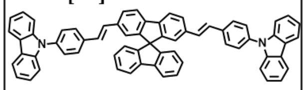 Spiro-SBCz: 0.11 μJ cm^{-2} **2007 [29]** 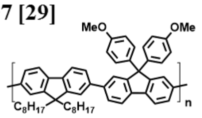 F8DP: 0.032 μJ cm^{-2} with mixed order DFB **2014 [28]** 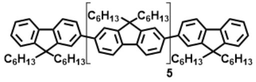 Terfuluorene: 0.40 μJ cm^{-2}	**2003 [30]** 1.0 kA cm^{-2} in small-area single-layer CuPc diodes **2005 [31]** 1.1 kA cm^{-2} in small area OLEDs fabricated on sapphire substrates and operated under short pulse voltages **2007 [32]** 6.0 MA cm^{-2} in small-area single-layer CuPc diodes fabricated on Si substrates **2015 [16]** 2.0 kA cm^{-2} in nano-patterned OLEDs operated under short pulse voltages	**2000 [33]** Investigation of polaron induced waveguide loss **2007 [34]** Investigation of annihilation processes at threshold current density **2008 [11]** Energy level alignment in OLEDs: Suppression of SPA **2010 [12]** Single layer device: Suppression of SPA **2010 [14]** Introduction of triplet quencher: Suppression of STA **2015 [16]** Nano-patterned device: Suppression of SPA
Next Electrically pumped OSLDs	**Next** Reduction of ASE or lasing threshold in OLEDs	**Next** Injection of high current density into OLEDs	**Next** Suppression of efficiency roll-off over 1 kA cm^{-2}

There are multiple requirements to realize OSLDs, including (1) reduction of ASE or lasing threshold, (2) injection of high current density in OLEDs containing organic laser dyes, and (3) suppression of efficiency roll-off at high current density. The progress regarding (1), (2), and (3) are also summarized in the second, third, and forth columns in Table 1-1. For (1), organic laser dyes of 4,4'-bis[(*N*-carbazole)styryl]biphenyl (BSB-Cz) and 2,7-bis[4-(*N*-carbazole)phenyl-vinyl]-9,9'-spirobifluorene (spiro-SBCz) having ultimately low ASE thresholds of 0.32 and 0.11 μJ cm^{-2}, respectively, were developed in Adachi's group [26,27]. E. Y. Choi et al. also reported a low ASE threshold of 0.4 μJ cm^{-2} in terfluorene [28]. C. Karnutsch et al. observed an extremely low lasing threshold of 0.032 μJ cm^{-2} by combining poly[9,9-dioctylfluorene-co-9,9-di(4-methoxy-phenyl)fluorene] (F8DP) with a mixed order distributed-feedback (DFB) system [29]. However, in most cases, ASE and lasing thresholds go up significantly in OLED structures because of a large propagation loss coming from metal electrodes [35-37] while very low ASE and lasing thresholds have easily been obtained in organic solutions and films alone. Therefore, the next challenge is to reduce ASE and lasing thresholds in OLED structures to similar levels obtained in solo layers. For (2), the injection of high current densities of up to 2 kA cm^{-2} into OLEDs has been demonstrated through suppressing Joule heating-induced breakdown by a reduction of device active areas and the use of high-thermal-conductivity substrates and short pulse voltages [16,30-32,38,39]. Extremely high current injection on the order of MA cm^{-2} into single-layer diodes of copper phthalocyanine (CuPc) with nano-size active areas, not OLEDs, was demonstrated by managing Joule heating [32]. To realize OSLDs, injection of much higher current density into OLEDs or reduce ASE or lasing threshold are needed. For (3), Y. Zhang et al., successfully suppressed roll-off induced by STA by reducing triplet population through triplet management using 9,10-di(naphth-2-yl)anthracene [14]. T. Matsushima and C. Adachi showed that the energy level alignment of HOMO and LUMO levels of dopant and host molecules leads to perfectly suppressed efficiency roll-off induced by SPA [11]. Y. Setoguchi and C. Adachi demonstrated suppressed efficiency roll-off in non-heterostructured single-layer OLEDs because this single-layer device architecture does not include heterointerfaces that cause carriers to be accumulated [12]. K. Hayashi et al., suppressed SPA-induced efficiency roll-off using nano-patterned OLEDs where excitons are spatially separated from polarons [16]. Although many device architectures have been tested to solve the efficiency roll-off problem to date, the investigation for the suppression of efficiency roll-off, especially in terms of materials, is not enough. Moreover, the suppression of efficiency roll-off in a current region over 1 kA cm^{-2} has not been achieved. A further investigation to suppress the efficiency roll-off and deeply understand hidden roll-off mechanisms are needed.

Figure 1-5 shows the relationship between exciton density and current density for OLEDs with a laser dye as an emitting dopant [12]. In this figure, the red solid line represents exciton density measured from ASE threshold under optical excitation, red symbols represent exciton density measured from the OLEDs, and black solid line represents exciton density when the efficiency roll-off does not happen. The current density where the red and black solid lines cross is the threshold current density required to obtain ASE under electrical excitation. Without efficiency roll-off, the threshold current density is about 1 kA cm^{-2}, which is possible to be injected into organic devices. However, the actual exciton density is predicted to follow the black dashed line because of the presence of efficiency roll-off. The threshold current density when including efficiency roll-off is estimated to be 100 kA cm^{-2}

from the crossing point of the red solid and black dashed lines. Although extremely high current injection on the order of MA cm^{-2} into CuPc was demonstrated by managing Joule heating [32], the highest current density ever achieved in OLEDs was as high as 2 kA cm^{-2} [16,38,39]. Therefore, the suppression of efficiency roll-off is required to reduce the threshold current density to an achievable level for the realization of OSLDs.

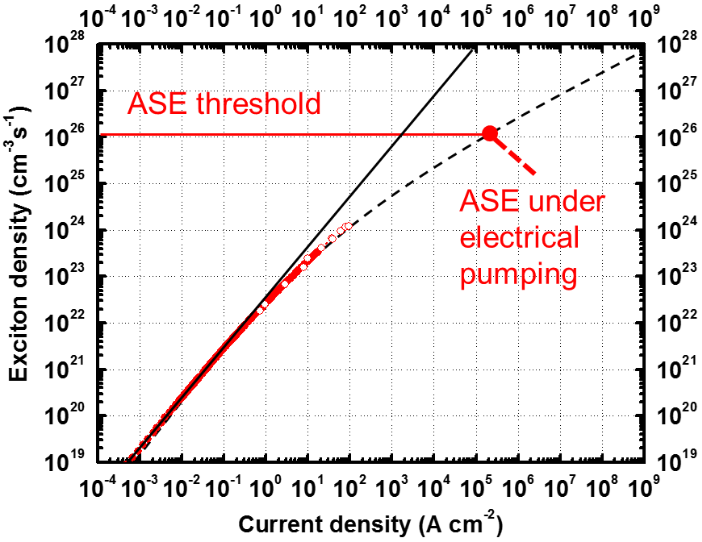

Figure 1-5. Exciton density-current density characteristics in single-layer OLEDs reported in reference [12].

1-2. Purpose and outline

The purpose of this study is to suppress efficiency roll-off observed in OLEDs through an understanding of efficiency roll-off mechanisms with the aim of realizing high-brightness OLEDs and OSLDs in future. This thesis is organized as follows. In Chapter 2, efficiency roll-off in OLEDs with the TADF emitters 1,2-bis(carbazol-9-yl)-4,5-dicyanobenzene (2CzPN) and 3-(9,9-dimethylacridin-10(9H)-yl)-9H-xanthen-9-one (ACRXTN) is investigated by considering intramolecular exciton relaxation processes. Efficiency roll-off at high current density is dramatically suppressed using ACRXTN as an emitter instead of 2CzPN because of suppressed STA and TTA. The rate constant of RISC from T_1 to S_1 for ACRXTN is about 300 times higher than that of 2CzPN, leading to a decrease of triplet exciton density and the suppression of exciton annihilation processes under optical and electrical excitation. In Chapter 3, to suppress STA, the efficient incorporation of oxygen as a triplet quencher into solid-state organic films is demonstrated by applying a high oxygen pressure of 200 MPa to the films. The oxygen-incorporated films show strong suppression of STA because triplet excitons are quenched by the incorporated oxygen. In Chapter 4, a ter(9,9’-spirobifluorene) (TSBF)-doped emitting layer is demonstrated to show a remarkably low ASE threshold and suppressed efficiency roll-off at high current densities. One of the origins of suppressed efficiency roll-off is perfectly suppressed STA in the TSBF-doped emitting layer. In addition, SPA, SHQ, and electric field-induced quenching are also possible to be suppressed due to small carrier density on a recombination zone, which is caused by small trap depth of TSBF in the emitting layer, and its quite large radiative rate constant. In Chapter 5, the summary of this thesis and future prospects are introduced.

References

[1] C. W. Tang, S. A. VanSlyke, Appl. Phys. Lett. **51** (1987) 913.

[2] C. Adachi, M. A. Baldo, M. E. Thompson, S. R. Forrest, J. Appl. Phys. **90** (2001) 5048.

[3] C. D. Müller, A. Falcou, N. Reckefuss, M. Rojahn, V Wiederhirn, P. Rudati, H. Frohne, O. Nuyken, H. Becker, K. Meerholz, Nature **421** (2003) 829.

[4] M. Pope, H. P. Kallmann, P. Magnante, J. Chem. Phys. **38** (1963) 2042.

[5] L. J. Rothberg, A. J. Lovinger, J. Mater. Res. **11** (1996) 3174.

[6] H. Uoyama, K. Goushi, K. Shizu, H. Nomura, C. Adachi, Nature **492** (2012) 234.

[7] C. Adachi, M. A. Baldo, S. R. Forrest, M. E. Thompson, Appl. Phys. Lett. **77** (2000) 904.

[8] A. Endo, M. Ogasawara, A. Takahashi, D. Yokoyama, Y. Kato, C. Adachi, Adv. Mater. **21** (2009) 4802.

[9] S. Y. Lee, T. Yasuda, H. Nomura, C. Adachi, Appl. Phys. Lett. **101** (2012) 093306.

[10] H. Nakanotani, H. Sasabe, C. Adachi, Appl. Phys. Lett. **86** (2005) 213506.

[11] T. Matsushima, C. Adachi, Appl. Phys. Lett. **92** (2008) 063306.

[12] Y. Setoguchi, C. Adachi, J. Appl. Phys. **108** (2010) 064516.

[13] Y. Zhang, M. Whited, M. E. Thompson, S. R. Forrest, Chem. Phys. Lett. **495** (2010) 161.

[14] Y. Zhang, M. Slootsky, S. Forrest, Appl. Phys. Lett. **99** (2011) 223303.

[15] C. Murawski, K. Leo, M. C. Gather, Adv. Mater. **25** (2013) 6801.

[16] K. Hayashi, H. Nakanotani, M. Inoue, K. Yoshida, O. Mikhnenko, T. Q. Nguyen, C. Adachi, Appl. Phys. Lett. **106** (2015) 093301.

[17] H. Ikeda, J. Photopolym. Sci. Technol. **28** (2015) 611.

[18] N. C. Giebink, S. R. Forrest, Phys. Rev. B **77** (2008) 235215.

[19] K. Masui, H. Nakanotani, C. Adachi, Org. Electron. **14** (2013) 2721.

[20] M. A. Baldo, C. Adachi, S. R. Forrest, Phys. Rev. B **62** (2000) 10967.

[21] P. P. Sorokin, J. R. Lankand, IBM J. Res. Develop. **10** (1966) 162.

[22] O. G. Peterson, S. A. Tuccio, B. B. Snavely, Appl. Phys. Lett. **17** (1970) 245.

[23] F. Hide, B. J. Shwartz, M. A. Díaz-García, A. J. Heeger, Chem. Phys. Lett. **256** (1996) 424.

[24] T. Rabe, K. Gerlach, T. Riedl, H. H. Johannes, W. Kowalsky, J. Niederhofer, W. Gries, J. Wang, T. Weimann, P. Hinze, F. Galbrecht, U. Scherf, Appl. Phys. Lett. **89** (2006) 081115.

[25] Y. Yang, G. A. Turnbull, I. D. W. Samuel, Appl. Phys. Lett. **92** (2008) 163306.

[26] T. Aimono, Y. Kawamura, K. Goushi, H. Yamamoto, H. Sasabe, C. Adachi, Appl. Phys. Lett. **86** (2005) 071110.

[27] H. Nakanotani, S. Akiyama, D. Ohnishi, M. Moriwake, M. Yahiro, T. Yoshihara, S. Tobita, C. Adachi, Adv. Funct. Mater. **17** (2007) 2328.

[28] E. Y. Choi, L. Mazur, L. Mager, M. Gwon, D. Pitrat, J. C. Mulatier, C. Monnereau, A. Fort, A. J. Attias, K. Dorkenoo, J. E. Kwon, Y. Xiao, K. Matczyszyn, M. Samoc, D. W. Kim, A. Nakao, B. Heinrich, D. Hashizume, M. Uchiyama, S. Y. Park, F. Mathevet, T. Aoyama, C. Andraud, J. W. Wu, A. Barsell, J. C. Ribierre, Phys. Chem. Chem. Phys. **16** (2014) 16941.

[29] C. Karnutsch, C. Pflumm, G. Heliotis, J. C. deMello, D. D. C. Bradley, J. Wang, T. Weimann, V. Haug, C. Gärtner, U. Lemmer, Appl. Phys. Lett, **90** (2007) 131104.

[30] H. Yamamoto, T. Oyamada, H. Sasabe, C. Adachi, Appl. Phys. Lett. **84** (2004) 1401.

[31] H. Nakanotani, T. Oyamada, Y. Kawamura, H. Sasabe, C. Adachi, Jpn. J. Appl. Phys. **44**

(2005) 3659.

[32] T. Matsushima, C. Adachi, Jpn. J. Appl. Phys. Part II **46** (2007) L1179.

[33] V. G. Kozlov, G. Parthasarathy, P. E. Burrows, V. B. Khalfin, J. Wang, S. Y. Chou, S. R. Forrest, IEEE J. Quantum. Electron. **36** (2000) 18.

[34] C. Gärtner, C. Karnutsch, U. Lemmer, C. Pflumm, J. Appl. Phys. **101** (2007) 023107.

[35] M. Stoessel, G. Wittmann, J. Staudigel, F. Steuber, J. Blässing, W. Roth, H. Klausmann, W. Rogler, J. Simmerer, A. Winnacker, M. Inbasekaran, E. P. Woo, J. Appl. Phys. **87** (2000) 4467.

[36] A. L. Burin, M. A. Ratner, J. Phys. Chem. A **104** (2000) 4704.

[37] H. Yamamoto, T. Oyamada, H. Sasabe, C. Adachi, Appl. Phys. Lett. **84** (2004) 1401.

[38] H. Yamamoto, H. Kasajima, W. Yokoyama, H. Sasabe, C. Adachi, Appl. Phys. Lett. **86** (2005) 083502.

[39] T. Matsushima, C, Adachi, Jpn. J. Appl. Phys. Part II **46** (2007) L861.

Chapter 2

Effect of reverse intersystem crossing on exciton annihilation in organic light-emitting diodes with thermally-activated delayed fluorescence emitters

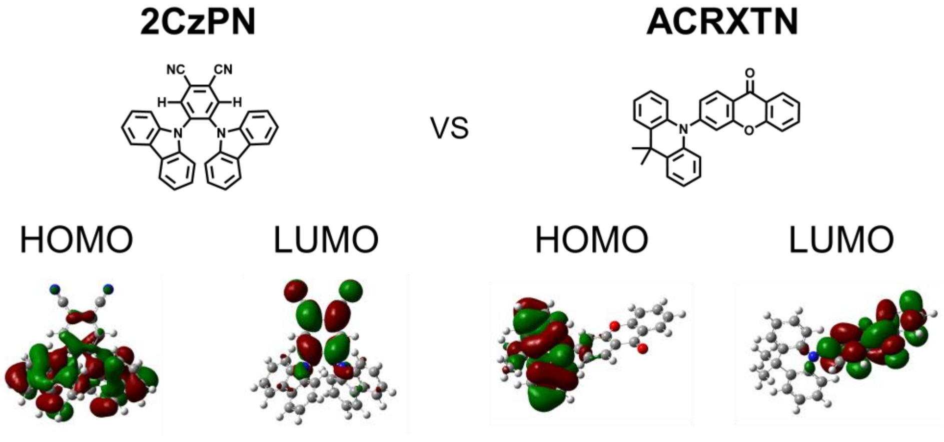

Munetomo Inoue, Tomas Serevičius, Hajime Nakanotani, Kou Yoshida,
Toshinori Matsushima, Saulius Juršėnas, and Chihaya Adachi

Chemical Physics Letters, **644** (2016) 62-67.

Abstract

Electroluminescence (EL) efficiency roll-off in OLEDs with TADF emitters 1,2-bis(carbazol-9-yl)-4,5-dicyanobenzene (2CzPN) and 3-(9,9-dimethylacridin-10(9H)-yl)-9H-xanthen-9-one (ACRXTN) is investigated by considering intramolecular exciton relaxation processes. EL efficiency roll-off at high current density is dramatically suppressed using ACRXTN as an emitter instead of 2CzPN because of suppressed bimolecular exciton annihilation processes such as STA and TTA. The rate constant of reverse intersystem crossing from T_1 to S_1 of ACRXTN is about 300 times higher than that of 2CzPN, decreasing triplet exciton density and suppressing exciton annihilation processes under optical and electrical excitation.

2-1. Introduction

Because OLEDs can exhibit nearly 100% η_{IQE}, they are attractive for next-generation lighting sources as well as display applications. Although nearly 100% η_{IQE} has been achieved, the decrease of EL efficiency, known as roll-off, at high brightness [1] is a serious problem, limiting the development of high-brightness OLEDs. Over the past two decades, two types of organic luminescent compounds have mainly been developed as emitters for OLEDs. OLEDs using fluorescent materials as emitters exhibit rather weak roll-off characteristics, although their η_{IQE} is intrinsically limited to 25% because only 25% of excitons, corresponding to singlet excitons, can be harvested under electrical excitation [1,2]. In contrast, although efficient room-temperature phosphorescent materials such as $\mathrm{Ir(ppy)_3}$ can provide nearly 100% η_{IQE}, the large accumulation of triplet excitons in an emitting layer causes considerable bimolecular deactivation, *i.e.*, TTA, because of the rather long lifetimes of triplet excitons (a few μs) compared with those of typical singlet excitons (a few ns) [1–5]. In fact, according to the reported simulations [1,4,6], the efficiency roll-off of OLEDs using (*E*)-2-(2-(4-(dimethylamino)styryl)-6-methyl-4*H*-pyran-4-ylidene)malononitrile as a fluorescent emitter and $Ir(ppy)_3$ as a phosphorescent emitter has been ascribed to mainly STA [1,6] and TTA [1,4], respectively.

Recently, Adachi et al., proposed a unique triplet harvesting process in OLEDs, namely TADF [7–9]. In TADF-OLEDs, although a maximum η_{IQE} of nearly 100% has been achieved, they also exhibit substantial roll-off behavior similar to that of phosphorescence-based OLEDs [8–10]. To understand the origin of the roll-off of TADF-OLEDs, here the author investigates the exciton annihilation processes in OLEDs containing the sky-blue TADF molecules 2CzPN and ACRXTN, and reveal that both STA and TTA contribute to the roll-off of TADF-OLEDs. The author demonstrates that the rate constant of RISC from T_1 to S_1 (k_{RISC}) of ACRXTN (k_{RISC} = ~10^5 s^{-1}) is about 300 times higher than that of 2CzPN (k_{RISC} = ~10^3 s^{-1}), and this larger k_{RISC} of ACRXTN decreases the triplet exciton density, suppressing STA and TTA under electrical excitation.

2-2. Experimental

The molecular structures of TADF emitters 2CzPN and ACRXTN are shown in Fig. 2-1(a). OLEDs containing 2CzPN and ACRXTN as emitters were fabricated by conventional vacuum deposition on glass substrates coated with a 100-nm-thick indium tin oxide (ITO) layer under a base pressure of around 7 × 10^{-4} Pa. The OLEDs possessed the structure of glass substrate / ITO (100 nm) / α-NPD hole-transport layer (HTL) (35 nm) / mCP electron-blocking layer (EBL) (10 nm) / 5 mol% 2CzPN- or ACRXTN-doped mCP (15 nm) emitting layer (EML) / PPT hole-blocking layer (HBL) (10 nm) / TPBi electron-transport layer (ETL) (40 nm) / LiF (0.8 nm) / Al (100 nm), where α-NPD, mCP, PPT, and TPBi are 4,4'-bis[*N*-(1-naphthyl)-*N*-phenyl-amino]biphenyl, *N*,*N*'-dicarbazolyl-3,5-benzene, 2,8-bis(di-phenylphosphoryl)dibenzo-[b,d]thiophene, and 2,2',2"-(1,3,5-benzinetriyl)-tris[1-phenyl-1-*H*-benzimidazole], respectively. The molecular structures of α-NPD, mCP, PPT, and TPBi are shown in Fig. 2-1(b).

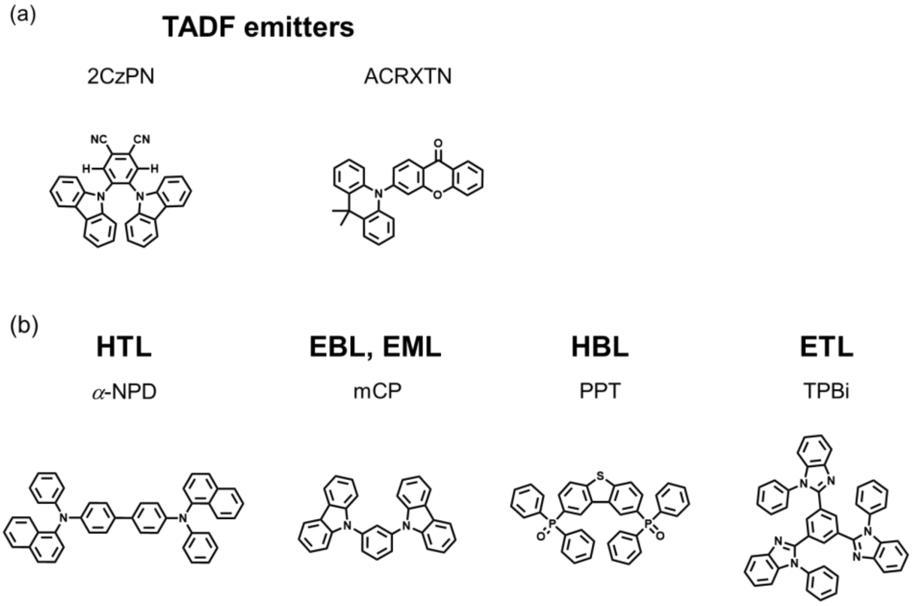

Figure 2-1. Molecular structures of (a) 2CzPN, ACRXTN, (b) α-NPD, mCP, PPT, and TPBi.

For optical measurements, 100-nm-thick mCP films doped with 5 mol% 2CzPN or ACRXTN were fabricated on quartz substrates by vacuum deposition. Photoluminescence (PL) spectra and PL quantum yields (PLQYs) of these films were measured by a spectrofluorometer (FluoroMax-4, Horiba Jobin Yvon) and PLQY measurement system (C9920-02, Hamamatsu Photonics), respectively. PL lifetimes of the films were measured under vacuum using a streak camera (C4334, Hamamatsu Photonics), and a nitrogen-gas laser (MNL200, Lasertechnik) with an excitation wavelength of 337 nm and pulse width of 500 ps as an excitation source. The rate constants shown in Fig. 2-1(b) were calculated from the values of PLQY and PL lifetime as previously reported [10].

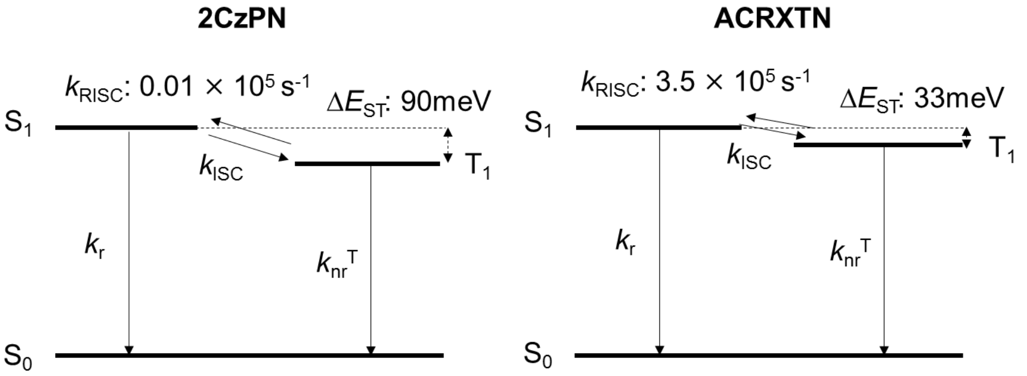

Figure 2-2. Illustration of intramolecular relaxation processes of TADF materials. The rate constants of each intramolecular relaxation process are summarized in Table 2-1.

Table 2-1. Summary of λ_{max}, ΔE_{ST}, Φ_{PL}, Φ_{prompt}, $\Phi_{delayed}$, τ_{prompt}, $\tau_{delayed}$, k_r, k_{ISC}, k_{RISC}, and k_{nr}^T of 2CzPN and ACRXTN molecules.

TADF emitters	λ_{max} [nm]	ΔE_{ST} [meV]	Φ_{PL} [%]	Φ_{prompt} [%]	$\Phi_{delayed}$ [%]	τ_{prompt} [ns]	$\tau_{delayed}$ [ms]	k_r [10^7 s^{-1}]	k_{ISC} [10^7 s^{-1}]	k_{RISC} [10^5 s^{-1}]	k_{nr}^T [10^5 s^{-1}]
2CzPN	471	90	81	66	15	19	164	3.5	1.8	0.011	0.0097
ACRXTN	478	33	92	74	18	26	2.4	2.2	0.79	3.5	1.0

Current density (J)–voltage (V)–external quantum efficiency (η_{EQE}) characteristics and EL spectra of the OLEDs were measured using an integrating sphere connected to a source meter (2400, Keithley Instruments) and photonic multichannel analyzer (PMA-12, Hamamatsu Photonics). The transient EL response of the OLEDs during long pulse voltage excitation was also measured using a photomultiplier tube (C9525-02, Hamamatsu Photonics) and pulse generator (WF 1974, NF corporation). The pulse width was 500 μs and the repetition frequency was 0.5 Hz for this measurement.

2-3. Results and discussion

2-3-1. Efficiency roll-off characteristics

EL spectra of the OLEDs containing 2CzPN and ACRXTN as emitters and PL spectra of the doped films are presented in Fig. 2-3. These OLEDs showed almost the same sky-blue EL spectra. The slight red shift of EL spectra compared with the PL spectra of the composite films was ascribed to an optical microcavity effect.

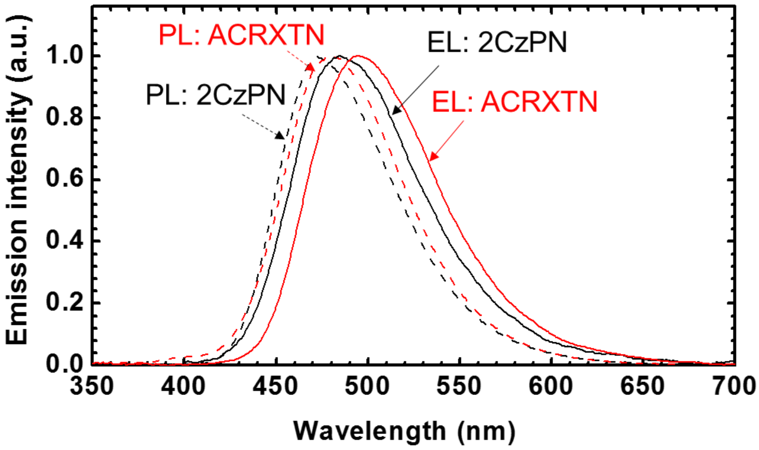

Figure 2-3. EL spectra of the OLEDs containing 2CzPN and ACRXTN as emitters measured at 50 mA cm^{-2} and PL spectra of the doped films.

J-*V* and η_{EQE}-*J* characteristics of the OLEDs with 2CzPN and ACRXTN are presented in Fig. 2-4. The maximum η_{EQE} ($\eta_{\mathrm{EQE,\,max}}$), current density when η_{EQE} decreases to half of the initial η_{EQE} (J_0), η_{EQE} at 1,000 cd m^{-2}, rate constant of STA (k_{STA}), and rate constant of TTA (k_{TTA}) are summarized in Table 2-2. Before the onset of the η_{EQE} roll-off, the $\eta_{\mathrm{EQE,\,max}}$ values of the OLEDs with 2CzPN and ACRXTN were similar values of 10.3% and 12.1%, respectively. The small difference in $\eta_{\mathrm{EQE,\,max}}$ originates from the different PLQYs of 2CzPN (81%) and ACRXTN (92%). Because both OLEDs showed similar *J*-*V* characteristics [Fig. 2-4(a)], it is expected that the carrier balance factor would have a small influence on $\eta_{\mathrm{EQE,\,max}}$.

However, J_0 of the OLEDs with ACRXTN and 2CzPN differed markedly. At L = 1,000 cd m^{-2}, η_{EQE} of the OLED with ACRXTN (η_{EQE} = 11.0%) was about five times larger than that of the OLED with 2CzPN (η_{EQE} = 2.2%), indicating that the roll-off at high current density was strongly suppressed using ACRXTN.

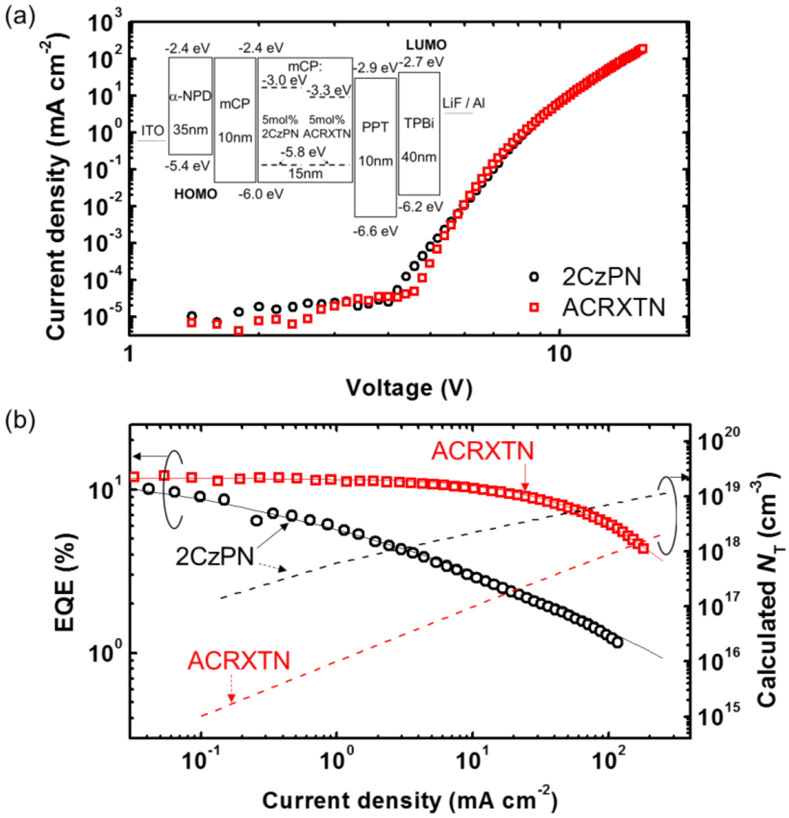

Figure 2-4. (a) J-V and (b) η_{EQE}-J characteristics of the OLEDs with 2CzPN and ACRXTN. The inset of (a) is an energy-level diagram of the OLEDs containing 2CzPN and ACRXTN as emitters. The solid and dashed lines in (b) are the fitting results and calculated N_T using the rate eqs. (2-1) and (2-2) based on STA and TTA models [ref. 10].

Table 2-2. Summary of $\eta_{\mathrm{EQE,\,max}}$, J_0, η_{EQE} at 1,000 cd m^{-2}, k_{STA}, and k_{TTA} of the OLEDs containing 2CzPN and ACRXTN as emitters.

TADF emitters	$\eta_{\mathrm{EQE,\,max}}$ [%]	J_0 [mA cm^{-2}]	η_{EQE} at 1,000 cd m^{-2} [%]	k_{STA} [10^{-11} cm^3 s^{-1}]	k_{TTA} [10^{-15} cm^3 s^{-1}]
2CzPN	10.3	1.6	2.2	2.1	5.0
ACRXTN	12.1	104	11.0	1.9	5.1

Here, k_{STA} and k_{TTA} were estimated using rate equations based on STA and TTA models [10],

$$\frac{dN_{\mathrm{S}}}{dt} = -(k_{\mathrm{r}} + k_{ISC})N_{\mathrm{S}} + k_{\mathrm{RISC}}N_{\mathrm{T}} - k_{\mathrm{STA}}N_{\mathrm{S}}N_{\mathrm{T}} + \alpha k_{\mathrm{TTA}}N_{\mathrm{T}}^{2} + \frac{J}{4de} \qquad (2\text{-}1)$$

and $$\frac{dN_{\mathrm{T}}}{dt} = k_{\mathrm{ISC}}N_{\mathrm{S}} - (k_{\mathrm{RISC}} + k_{\mathrm{nr}}^{\mathrm{T}})N_{\mathrm{T}} - (1+\alpha)k_{\mathrm{TTA}}N_{\mathrm{T}}^{2} + \frac{3J}{4de}, \qquad (2\text{-}2)$$

where N_{S} and N_{T} are the singlet and triplet exciton densities, respectively, k_{r} is the rate constant of radiative emission from S_1, k_{ISC} is the rate constant of ISC from S_1 to T_1, $k_{\mathrm{nr}}{}^{\mathrm{T}}$ is the rate constant of non-radiative decay from T_1 to S_1, and α is the singlet exciton production ratio *via* TTA, which is 0.25 according to spin statistics [10]. In practical devices, the temperature increase induced by Joule-heating would affect $k_{\mathrm{nr}}{}^{\mathrm{T}}$, k_{TTA}, and k_{RISC}. However, the mechanisms of the temperature dependence in the rate equations are quite complicated due to the competition of all inter- and intramolecular processes. Here, the author neglects the effect of the temperature increase because the maximum injected current density in the devices is relatively low and the generated Joule-heating should be same in the devices of 2CzPN and ACRXTN. The relationship between the temperature increase and the efficiency roll-off should be investigated in detail in the future. Fitting the experimental η_{EQE}-J data with eqs. (2-1) and (2-2) [Fig. 2-4(b)] yields $k_{\mathrm{STA}} = 2.1 \times 10^{-11}$ cm^3 s^{-1} and $k_{\mathrm{TTA}} = 5.0 \times 10^{-15}$ cm^3 s^{-1} for 2CzPN, and $k_{\mathrm{STA}} = 1.9 \times 10^{-11}$ cm^3 s^{-1} and $k_{\mathrm{TTA}} = 5.1 \times 10^{-15}$ cm^3 s^{-1} for ACRXTN [Table 2-2]. Although k_{STA} and k_{TTA} of the OLEDs with ACRXTN and 2CzPN are quite similar, a large difference in their roll-off characteristics was observed. Actually, N_{T} in the OLEDs with ACRXTN, calculated using eqs. (2-1) and (2-2), is much smaller than that in the OLEDs with 2CzPN at all current densities [Fig. 2-4(b)]. The experimental J, η_{EQE}, and $\eta_{\mathrm{EQE}}/\eta_{\mathrm{EQE,\,max}}$ for the OLEDs containing ACRXTN and 2CzPN at different N_{T} are summarized in Table 2-3. It is interesting that the $\eta_{\mathrm{EQE}}/\eta_{\mathrm{EQE,\,max}}$ values for 2CzPN are the same as those for ACRXTN at the same N_T while there is no clear relationship between other parameters, indicating that the roll-off characteristics are essentially controlled by N_T.

Table 2-3. Summary of J, η_{EQE}, and $\eta_{EQE}/\eta_{EQE,max}$ of the OLEDs containing 2CzPN and ACRXTN at different N_T.

TADF emitters	N_T [10^{17} cm^{-3}]	J [mA cm^{-2}]	η_{EQE} [%]	$\eta_{EQE}/\eta_{EQE,\max}$
2CzPN	1.0	0.1	8.7	0.84
	5.0	0.6	6.6	0.64
	10.0	1.8	4.8	0.47
ACRXTN	1.0	7.8	10.3	0.85
	5.0	51.0	7.7	0.64
	10.0	100	6.0	0.49

2-3-2. Investigation of suppressed efficiency roll-off

To investigate the origin of the suppressed roll-off behavior and lower N_T for ACRXTN than 2CzPN, the intramolecular exciton relaxation processes of ACRXTN and 2CzPN were examined. The rate constants of the intramolecular relaxation processes were calculated from the PLQYs and PL lifetimes of the doped films according to ref. 10. Table 2-1 summarizes the calculated λ_{max}, ΔE_{ST}, Φ_{PL}, Φ_{prompt}, $\Phi_{delayed}$, τ_{prompt}, $\tau_{delayed}$, k_r, k_{ISC}, k_{RISC}, and k_{nr}^T for ACRXTN and 2CzPN, where λ_{max} is the PL peak wavelength; ΔE_{ST} is the energy gap between S_1 and T_1; Φ_{PL}, Φ_{prompt}, and $\Phi_{delayed}$ are the PLQYs of the total, prompt, and delayed components, respectively; and τ_{prompt} and $\tau_{delayed}$ are the PL lifetimes of the prompt and delayed components, respectively. Although there is no large difference in k_r and k_{ISC} between 2CzPN and ACRXTN, it is noteworthy that k_{RISC} of ACRXTN is about 300 times higher than that of 2CzPN because of its smaller ΔE_{ST} of 33 meV. The larger k_{RISC} makes it possible to decrease the N_T under electrical excitation, resulting in the suppression of STA and TTA as shown in Fig. 2-5.

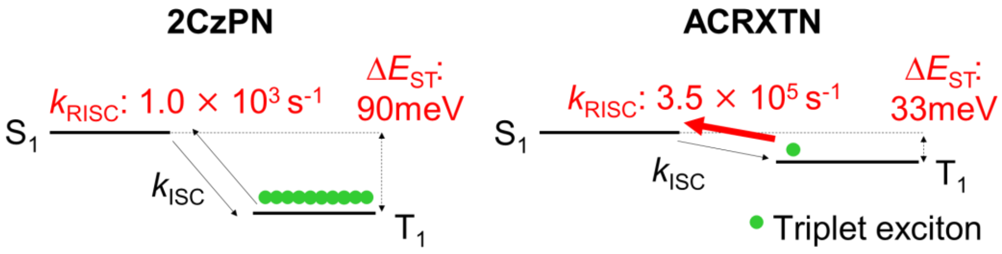

Figure 2-5. Energy level diagrams showing S_1 and T_1 of 2CzPN and ACRXTN.

To further investigate how k_{RISC} affects the STA and TTA characteristics of the emitters at high current densities, the roll-off characteristics when the OLEDs were driven under pulse voltage excitation were measured [Fig. 2-6]. The author assumes that the OLED breakdown observed at high current densities and voltages is caused by melting of organic layers due to

Joule heating. The Joule heating-induced breakdown is suppressed by a reduction of device active areas and use of high-thermal-conductivity substrates and short pulse voltages because of suppressed Joule heating [11,12]. Therefore, a very high voltage of up to 48 V could be applied to the OLEDs under the pulse voltage excitation, enabling very high current injection of up to 4.5 A cm^{-2} without irreversible device breakdown. The *J*-*V* characteristics of both the OLEDs measured under the pulse voltage excitation agree well each other [Fig. 2-6(a)]. The η_{EQE}-J curves measured under pulse voltage excitation exhibited roll-off characteristics similar to those measured under DC conditions below 100 mA cm^{-2}. At high current density (over 100 mA cm^{-2}), the roll-off was still greater for the 2CzPN-based OLEDs than the ACRXTN-based ones. Here, we calculated N_{RISC} (= $k_{\mathrm{RISC}} \times N_{\mathrm{T}}$), N_{STA} (= $k_{\mathrm{STA}} \times N_{\mathrm{S}} \times N_{\mathrm{T}}$), and N_{TTA} [= $(1+\alpha) \times k_{\mathrm{TTA}} \times N_{\mathrm{T}}^2$] using eqs. (2-1) and (2-2), which are plotted as a function of current density in Figs. 2-6(b) and 2-6(c). N_{RISC} is the number per unit time of the decrease of triplet excitons or increase of singlet excitons by RISC. N_{STA} is the number per unit time of the decrease of singlet excitons by STA, while N_{TTA} is the number per unit time of the decrease of triplet excitons by TTA. N_{STA} and N_{TTA} were higher than N_{RISC} at most current densities for the OLEDs with 2CzPN, resulting in the observed marked efficiency roll-off. Conversely, at most current densities, N_{RISC} was higher than N_{STA} and N_{TTA} in the OLEDs with ACRXTN and N_{STA} and N_{TTA} in the OLEDs with ACRXTN were lower than those of the OLEDs with 2CzPN, effectively suppressing the efficiency roll-off in ACRXTN based OLEDs. These results suggest that RISC, STA, and TTA compete during operation of the OLEDs, and that the faster RISC overcomes STA and TTA in the OLEDs with ACRXTN.

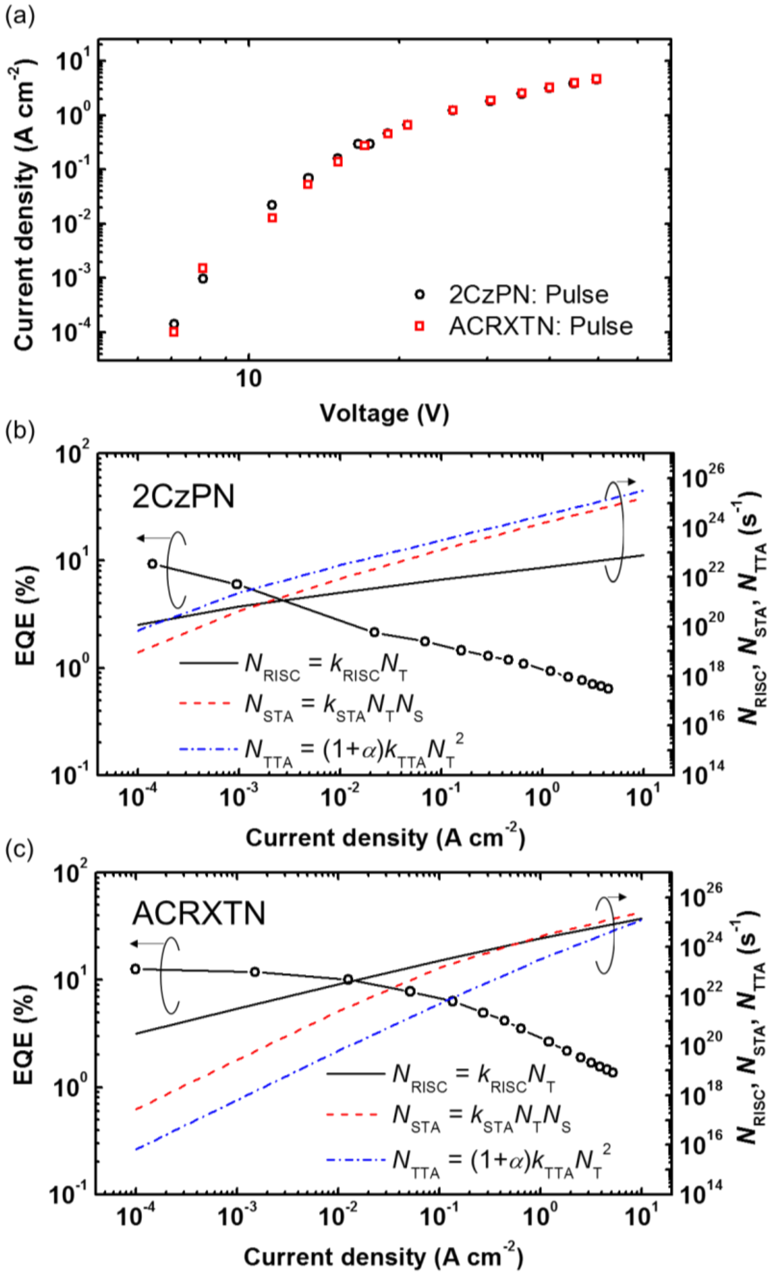

Figure 2-6. (a) *J*-*V* characteristics of the OLEDs with 2CzPN and ACRXTN and η_{EQE}-J characteristics of the OLEDs containing (b) 2CzPN and (c) ACRXTN. These devices were driven by pulsed voltages with a pulse width of 500 μs and repetition frequency of 0.5 Hz. The solid, dashed, and dot-dashed lines in (b,c) are N_{RISC} (= $k_{\mathrm{RISC}} \times N_{\mathrm{T}}$), N_{STA} (= $k_{\mathrm{STA}} \times N_{\mathrm{S}} \times N_{\mathrm{T}}$), and N_{TTA} [= $(1+\alpha) \times k_{\mathrm{TTA}} \times N_{\mathrm{T}}^2$], respectively, calculated using eqs. (2-1) and (2-2). EQE on the y-axis in (b,c) stands for external quantum efficiency.

2-3-3. Evidence of singlet-triplet annihilation

Additionally, an initial change in EL intensity during pulse voltage excitation at a high current density of 4.5 A cm^{-2} was observed between the OLEDs with 2CzPN and ACRXTN [Fig. 2-7]. The EL intensity suddenly decreased after an initial increase in EL intensity for the 2CzPN-based OLEDs while the ACRXTN-based OLEDs showed no such EL decrease. Similar decreases in EL and PL intensities have been observed for fluorescent OLEDs and composite films of TADF materials and attributed to STA [6,13,14].

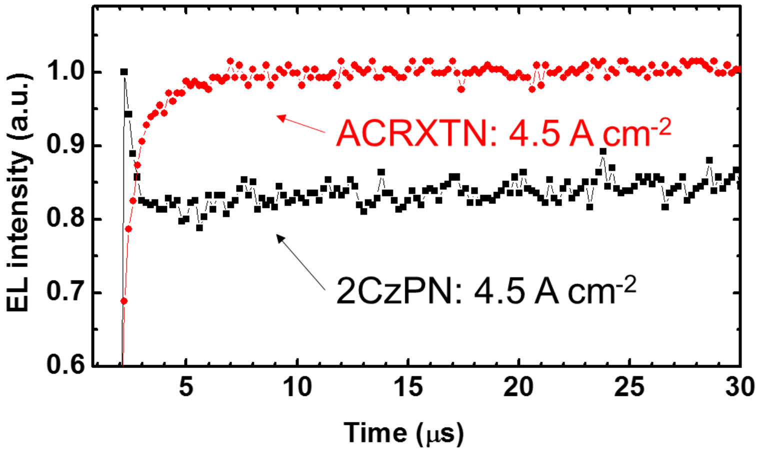

Figure 2-7. Change of EL intensity of the OLEDs containing 2CzPN and ACRXTN under pulse voltage excitation at a high current density of 4.5 A cm^{-2}.

The author also investigated the PL decay characteristics of the doped films measured using a long pulse excitation, as shown in Fig. 2-8. In the 2CzPN films photoexcited at the lower light intensities of 4.5 and 6.1 W cm^{-2}, the PL intensities gradually increased because populated triplet excitons are converted into singlet excitons *via* a slow TADF process. However, the PL intensities began to decrease at longer time period when using excitation light intensities higher than 15 W cm^{-2} because the STA and TTA processes become dominant over the conversion to singlet excitons. In contrast, such a decrease in PL intensity was not observed for the ACRXTN films, indicating that STA and TTA do not occur in them. These results show that a larger k_{RISC} leads to smaller efficiency roll-off because of lower triplet population. Therefore, the author concludes that the initial decrease of the EL and PL intensities observed for 2CzPN is further proof of the occurrence of strong STA.

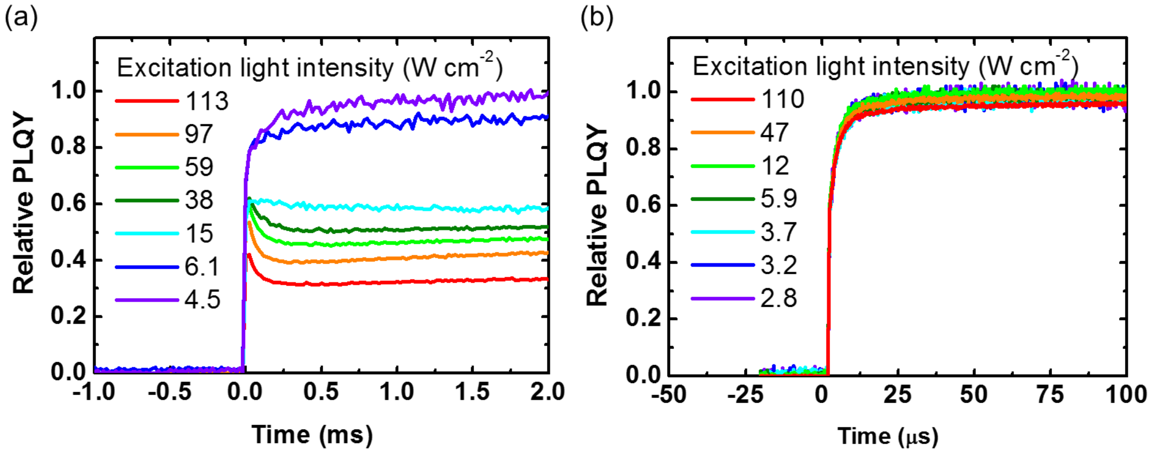

Figure 2-8. Dependence of excitation light intensities on the PL decay curves of mCP films doped with 5 mol% (a) 2CzPN and (b) ACRXTN. The relative PLQYs on the Y-axis were estimated by dividing PL intensities by each excitation light intensity.

2-3-4. Possibility of triplet-polaron annihilation

K. Masui et al., calculated N_S, N_T, and polaron density (N_P) by using the Langevin recombination model and demonstrated that TTA mainly contributes to efficiency roll-off in 2CzPN [10] because N_T is two or four orders of magnitude larger than N_P and N_S. Moreover, TTA is known to be the main cause of efficiency roll-off in phosphorescence emitters [1,15,16]. These results agree with this result which shows that N_{TTA} is the largest in 2CzPN as shown in Fig. 2-6(b). On the other hand, there is a possibility that TPA also causes efficiency roll-off due to larger N_P than N_S on the basis of the Masui's result. However, the contribution of TPA would be smaller than that of STA because k_{TPA} is usually smaller than the other quenching rate constants ($< 1.0 \times 10^{-12}$ cm^{-3} s^{-1}) [6,10,15-19].

2-4. Summary

The author investigated the roll-off characteristics of TADF-OLEDs with 2CzPN and ACRXTN as emitters. The author revealed that efficient RISC is an important factor to suppress efficiency roll-off in TADF-OLEDs. In fact, the large k_{RISC} of 3.5×10^5 s^{-1} of ACRXTN dramatically suppressed both STA and TTA processes. The author concludes that the molecular design of TADF materials with small ΔE_{ST} is requisite for not only obtaining high η_{EQE} but also suppressing efficiency roll-off. In addition to small ΔE_{ST}, the temperature increase induced by Joule-heating in the device would enhance k_{RISC} under high current densities. The relationship between the temperature increase and the efficiency roll-off should be investigated in detail in the future.

References

[1] C. Murawski, K. Leo, M. C. Gather, Adv. Mater. **25** (2013) 6801.

[2] N. C. Giebink, S. R. Forrest, Phys. Rev. B **77** (2008) 235215.

[3] M. A. Baldo, D. F. O'Brien, Y. You, A. Shoustikov, S. Sibley, M. E. Thompson, S. R. Forrest, Nature **395** (1998) 151.

[4] M. A. Baldo, C. Adachi, S. R. Forrest, Phys. Rev. B **62** (2000) 10967.

[5] C. Adachi, M. A. Baldo, M. E. Thompson, S. R. Forrest, J. Appl. Phys. **90** (2001) 5048.

[6] Y. Zhang, M. Whited, M. E. Thompson, S. R. Forrest, Chem. Phys. Lett. **495** (2010) 161.

[7] A. Endo, M. Ogasawara, A. Takahashi, D. Yokoyama, Y. Kato, C. Adachi, Adv. Mater. **21** (2009) 4802.

[8] S. Y. Lee, T. Yasuda, H. Nomura, C. Adachi, Appl. Phys. Lett. **101** (2012) 093306.

[9] H. Uoyama, K. Goushi, K. Shizu, H. Nomura, C. Adachi, Nature **492** (2012) 234.

[10] K. Masui, H. Nakanotani, C. Adachi, Org. Electron. **14** (2013) 2721.

[11] Y. Setoguchi, C. Adachi, J. Appl. Phys. **108** (2010) 064516.

[12] H. Yamamoto, H. Kasajima, W. Yokoyama, H. Sasabe, C. Adachi, Appl. Phys. Lett. **86** (2005) 083502.

[13] T. Furukawa, H. Nakanotani, M. Inoue, C. Adachi, Sci. Rep. **5** (2015) 8429.

[14] H. Nakanotani, T. Furukawa, C. Adachi, Adv. Opt. Mater. **3** (2015) 1381.

[15] M. A. Baldo, C. Adachi, S. R. Forrest, Phys. Rev. B **62** (2000) 10967.

[16] M. A. Baldo, S. R. Forrest, Phys. Rev. B **64** (2001) 085201.

[17] J. Kalinowski, W. Stamor, J. Mezyk, M. Cocchi, D. Virgili, V. Fattori, P. Di Marco, Phys. Rev. B **66** (2002) 235321.

[18] S. Reineke, G. Scwartz, K. Leo, Phys. Rev. B **75** (2007) 125328.

[19] D. Kasemann, R. Brückner, H. Fröb, K. Leo, Phys. Rev. B **84** (2011) 115208.

Chapter 2

Chapter 3

Incorporation of oxygen into organic thin films with the aim of suppressing singlet-triplet annihilation

The equipment for cold isostatic pressing

(this figure was obtained from the web page of NPa SYSTEM. http://www.npasystem.co.jp/)

Munetomo Inoue, Toshinori Matsushima, Hajime Nakanotani, and Chihaya Adachi

Chemical Physics Letters, **624** (2015) 43-46.

Abstract

Efficient incorporation of oxygen into a solid-state organic film is demonstrated by applying a high oxygen pressure of 200 MPa to the film. The oxygen-incorporated film shows strong suppression of STA because triplet excitons are quenched by oxygen incorporated inside the film. It is demonstrated that oxygen molecules are uniformly distributed in the film and that oxygen molecules are left in the film to some extent when the film is in a vacuum. The concentration of oxygen inside the film is calculated to be a very high value of the order of 4.4×10^{20} cm^{-3}.

3-1. Introduction

One of the most serious problems making the realization of OSLDs difficult is a rapid decrease in η_{EQE} at high current densities (efficiency roll-off as the author discussed earlier). The roll-off is in-part due to quenching of singlet excitons by inevitably populated triplet excitons [1]. Exciton quenching of this sort is termed STA. Three-times as many triplet excitons as single excitons are generated after recombination of injected electrons and holes in OLEDs because of the laws of spin statistics [2,3]. Moreover, triplet excitons have a much longer lifetime (μs to ms) than singlet excitons have (ns) [4]. Therefore, simulations have shown that a density of triplet excitons becomes five orders of magnitude larger than that of singlet excitons inside OLEDs operated at 0.8 A cm^{-2} [1]. The large density of triplet excitons is the cause of not only strong STA but also triplet-triplet (T_1-T_n) absorption [5]. T_1-T_n absorption also impedes the realization of OSLDs because T_1-T_n absorption results in a waveguide loss for light amplification [5]. On the other hand, only singlet excitons are formed under optical pumping unless ISC from S_1 to T_1 occurs. In this case, since STA no longer contributes to a decrease in PLQY, optically pumped lasers based on organic solutions and solid-state organic films have been easily realized [6-8]. Therefore, a decrease of triplet exciton density under electrical operation at high current density is very important for the realization of OSLDs.

To suppress STA, cyclooctatetraene (COT) [9-12] and oxygen [9,13] have been used as triplet quenchers because COT has a low T_1 level and very short triplet lifetime [11] and oxygen has a triplet ground state without absorption in the visible region [14]. By using these triplet quenchers, cw lasing from a dye solution [15] and quenching of phosphorescence and delayed fluorescence of a conjugated polymer [12] have been reported. However, since COT and oxygen are in liquid and gas states, respectively, at common temperatures and pressures, incorporating these triplet quenchers into solid-state organic films is difficult. In this study, a modified cold isostatic pressing (CIP) technique is used to efficiently incorporate oxygen into solid-state films.

CIP has been widely used to compress and mold metal, ceramic, plastic, and composite powders [16-18]. The powders are enclosed in a flexible, sealed polymer bag and loaded in a pressure vessel filled with a liquid. A high pressure is applied to the bag through the liquid medium by pushing a metal piston into the vessel with an external pressurization source. Since CIP applies isostatic pressure to the powders in all directions, moldings with uniform mass densities are obtained because there is little friction with the liquid medium. This standard CIP technique was modified to introduce oxygen into organic films. First, an organic film is vacuum-deposited on a substrate [Fig. 3-1(a)]. The film is enclosed in a polymer bag, which is filled with pure oxygen [Fig. 3-1(b)]. Then, the bag is immersed in room-temperature water [Fig. 3-1(c)]. A high pressure is applied to the bag in the same manner as with CIP [Fig. 3-1(d)]. Oxygen molecules are expected to penetrate the film under the application of the high oxygen pressure. The difference between the standard and modified CIP techniques is whether the bag is not filled or filled with oxygen. It is known that, under optical pumping, triplet excitons are easily accumulated in a film of tris(8-hydroxyquinolinato)aluminum (Alq_3) doped with (*E*)-2-(2-(4-(dimethylamino)styryl)-6-methyl-4*H*-pyran-4-ylidene)malononitrile (DCM) [19,20]. Therefore, in this study, the author attempted to incorporate oxygen into this film using the modified CIP technique. As the results, the author demonstrated that the oxygen-incorporated film exhibits efficient suppression of STA.

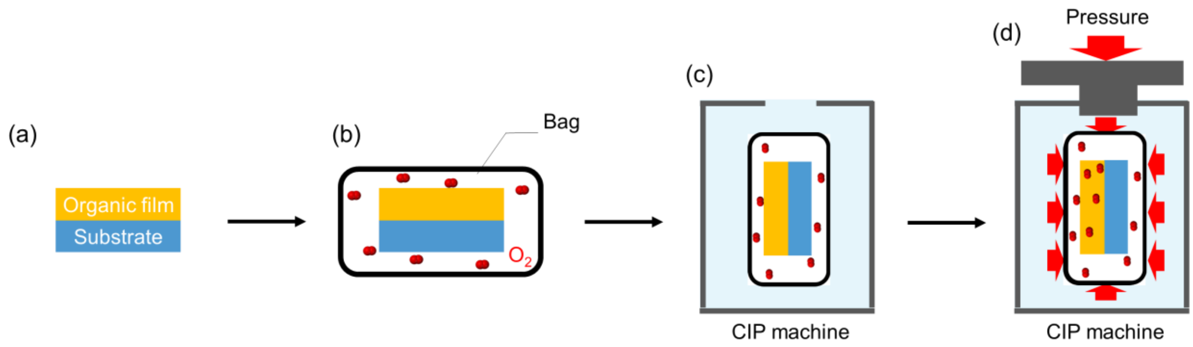

Figure 3-1. Schematic views of modified CIP technique. (a) The organic film is deposited on the substrate. (b) The organic film is enclosed in a flexible, polymer bag, which is filled with oxygen. (c) The bag is immersed in a pressure vessel filled with room-temperature water. (d) A high pressure of 200 MPa is applied to the bag.

3-2. Experimental

In this study, the author used a solid-state film of Alq_3 doped with DCM at 3 wt% because this doped film is one of the candidates for the laser application [21]. The molecular structures of DCM and Alq_3 are shown in Fig. 3-2. A 100-nm-thick DCM-doped Alq_3 film was vacuum-deposited onto a glass substrate at a deposition rate of 0.30 nm s^{-1} under a base pressure of 7×10^{-4} Pa. Then, the modified CIP was performed on this sample with the room-temperature water as a pressurization medium as shown in Fig. 3-1. The applied pressure and treatment time were 200 MPa and 15 min, respectively.

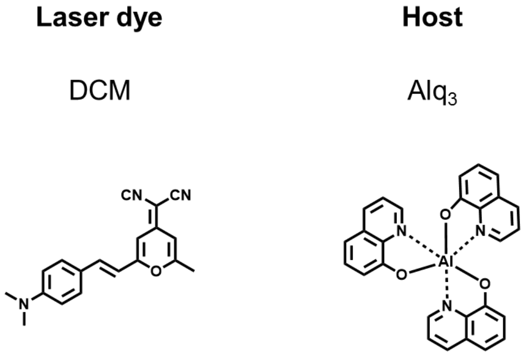

Figure 3-2. Molecular structures of DCM and Alq_3.

The transient PL characteristics of the film were measured to investigate how oxygen inside the film affects the STA characteristics. The rectangular pulse excitation light from a laser diode (a wavelength of 405 nm and pulse width of 40 μs) was irradiated to the film from the film side at the normal to the substrate. The focus diameter and power of the excitation light were 60 μm at 1.4 kW cm^{-2}, respectively. This excitation light intensity was very strong and almost corresponded to an ASE threshold energy (2.2 kW cm^{-2}) of this film [22]. The transient PL from the film was measured at an angle of 45° using a photomultiplier tube (C9525-02, Hamamatsu Photonics). The above-mentioned measurement conditions were used to investigate the STA characteristics unless otherwise mentioned. The PLQY of the film was measured by using an absolute PLQY measurement system (C11347 Quantaurus-QY, Hamamatsu Photonics).

3-3. Results and discussion

3-3-1. Suppression of singlet-triplet annihilation with oxygen

Figure 3-3(a) shows the transient PL characteristics of the Alq_3 film doped with 3 wt% DCM. The ratios of the PL intensities at 40 μs to those at 0 μs (I_{PL}/I_{PL_0}) are plotted in Fig. 3-3(b). If STA does not occur in the film, a decrease in PL intensity is not observed in the transient PL characteristics. However, the as-deposited unpressed film that was measured in a nitrogen atmosphere showed a strong decrease in PL intensity down to 53% of the initial value because of the occurrence of strong STA. This is due to the sufficient accumulation of triplet excitons generated with a quantum efficiency of intersystem crossing of 0.15 in the DCM-doped Alq_3 film [20]. When this unpressed film was placed in oxygen, the STA was slightly suppressed because the physisorbed oxygen on the film surface quenches triplet excitons near the film surface. On the other hand, the modified CIP with oxygen enabled the STA of the film to be most significantly suppressed because triplet excitons are effectively quenched by oxygen incorporated inside the films by the high pressure. Because there was no big difference in PLQY between the unpressed and oxygen-pressed films (55 and 57%, respectively), the icorporated oxygen in the film does not quench singlet excitons.

The oxygen-pressed film was placed in vacuum for 30 min. Then, the STA properties were measured again in vacuum. The suppression of the STA was still observed from this film [Fig. 3-3]. This result shows that it is difficult that once incorporated oxygen is immediately removed from the film even after the vacuum treatment because of the Van der Waals force between the incorporated oxygen and the Alq_3 molecules and that additional organic and electrode layers can be vacuum-deposited on top of the DCM-doped Alq_3 layer including oxygen for the fabrication of organic devices. In fact, T. Matsushima and C. Adachi reported oxygen molecules remain in the once oxygen-exposed Alq_3 films by using a thermally stimulated current technique [23]. Zhang *et al.* have used 9,10-di(naphth-2-yl)anthracene (ADN) as a triplet quencher in an Alq_3 film doped with 4-(dicyanomethylene)-2-methyl- 6-julolidyl-9-enyl-4*H*-pyran (DCM2) at 2 vol% [22]. Here, the author compares this STA properties with those of the reported ADN-doped film [Fig. 3-3(b)]. It was found that the oxygen-pressed films without and with the vacuum treatment showed the same effect for the suppression of STA as the ADN doping concentrations of 50 and 30 vol%, respectively, indicating the effectiveness of the modified CIP technique.

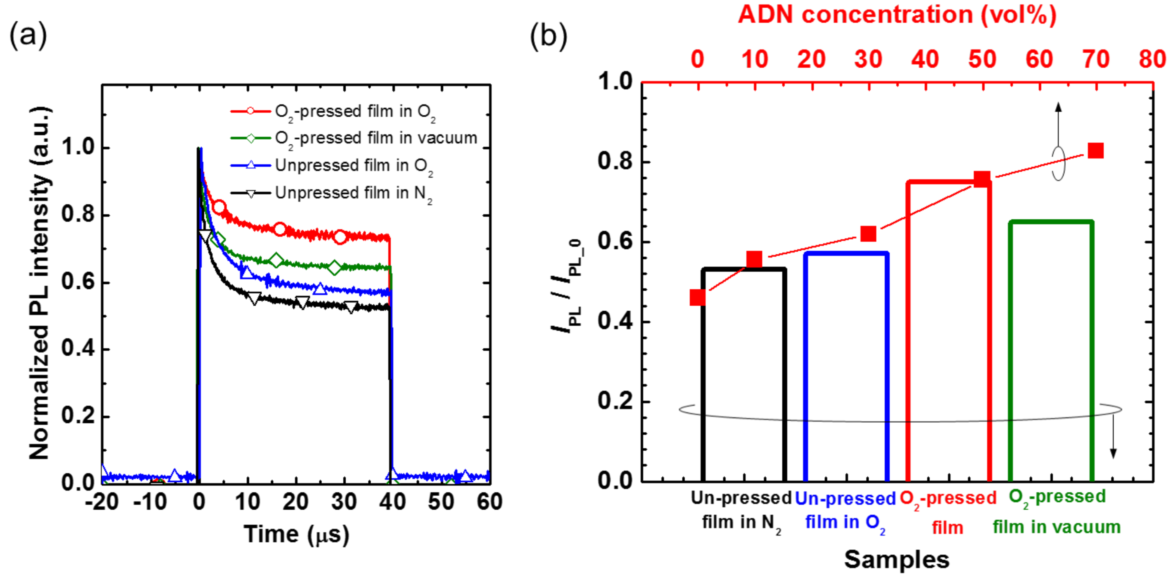

Figure 3-3. (a) Transient PL characteristics of the 3 wt% DCM-doped Alq_3 films. (b) Comparison of the I_{PL}/I_{PL_0} ratios of the DCM-doped Alq_3 films with those of the films where DCM2, ADN and Alq_3 were ternary-mixed [Ref. 22].

3-3-2. Incorporation of xenon and nitrogen into organic films

A heavy-atom effect is known to enhance intersystem crossing between S_1 and T_1 and a radiative decay process from T_1 because the spin-orbit coupling is enhanced [24]. It has been reported that xenon shows a small heavy-atom effect [24]. Therefore, the author also tried to incorporate xenon into the same film with the modified CIP technique. However, there was no difference in the transient PL curves between the unpressed and xenon-pressed films [Fig. 3-4], probably indicating that the heavy-atom effect of xenon is not high enough to suppress the STA. The author also confirmed that introduction of nitrogen into the film did not affect the STA properties [Fig. 3-4].

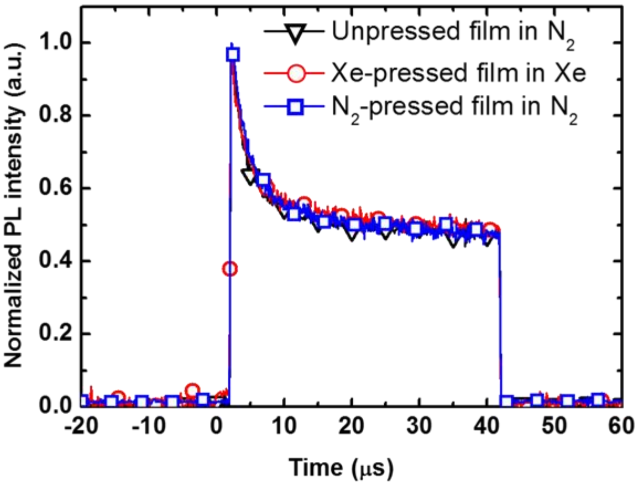

Figure 3-4. Transient PL properties of the unpressed film placed in nitrogen, xenon-pressed film placed in xenon, and nitrogen-pressed film placed in nitrogen. No differences in the transient PL curves were observed between them.

3-3-3. Distribution of oxygen in organic films

For a better understanding of the oxygen distribution inside the film, the author investigated the dependence of incidence directions of excitation light from the glass and film sides on STA properties. The STA properties of the unpressed film placed in nitrogen were independent of the light incidence directions [Fig. 3-5(a)]. However, for the unpressed film placed in oxygen, the suppression of the STA was more significant under the light incidence from the film side than that from the substrate side [Fig. 3-5(b)] because of quenching of triplet excitons by the physicsorbed oxygen on the film surface. The dependence of the light-incidence directions was not observed from the oxygen-pressed film placed in oxygen, indicating that oxygen molecules incorporated by the modified CIP technique are uniformly distributed in the 100-nm-thick film [Fig. 3-5(c)].

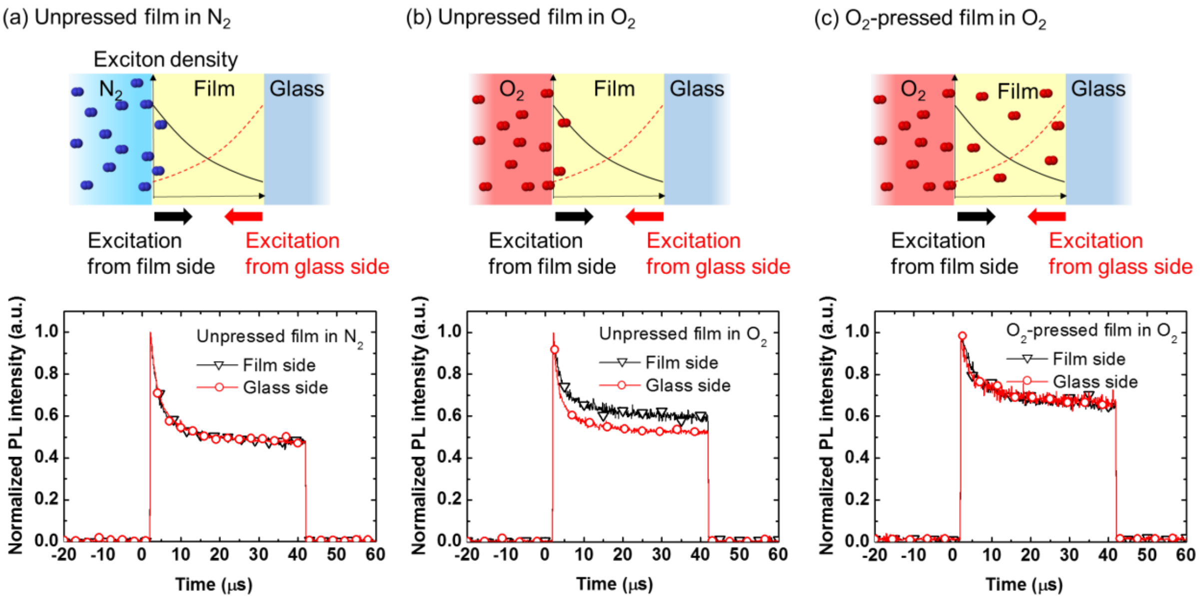

Figure 3-5. Dependence of incidence directions of excitation light on STA properties for (a) the unpressed film placed in nitrogen, (b) unpressed film placed in oxygen, and (c) oxygen-pressed film placed in oxygen before the vacuum treatment.

3-3-4. Estimation of oxygen concentration

The dependence of excitation light intensities ranging from 10^{-1} to 10^{3} W cm^{-2} on STA properties of the unpressed film measured in nitrogen and the oxygen-pressed film before the vacuum treatment was investigated [Fig. 3-6]. Below 1 W cm^{-2}, the $I_{\mathrm{PL}}/I_{\mathrm{PL\_0}}$ ratios of both the unpressed and oxygen-pressed films were unity, indicating that the triplet exciton density at low excitation light intensities is not high enough to induce STA. The threshold excitation light intensity, where the $I_{\mathrm{PL}}/I_{\mathrm{PL\_0}}$ begins to decrease, is about 1 W cm^{-2} for the unpressed film and about 10 W cm^{-2} for the oxygen-pressed film. The STA properties of the oxygen-pressed film were found to be more effectively suppressed than those of the unpressed film at the high excitation light intensities over 1 W cm^{-2}.

The STA properties of the doped films were next analyzed using several rate equations [22]. Based on the rate equations and reported rate constants, the $I_{\mathrm{PL}}/I_{\mathrm{PL\_0}}$ plots were fitted as shown in Fig. 3-6 to estimate the saturated triplet population (N_0) of the guest molecules. The fitting yielded $N_0 = 4.0 \times 10^{18}$ cm^{-3} for the unpressed film and $N_0 = 2.2 \times 10^{18}$ cm^{-3} for the oxygen-pressed film.

To estimate the oxygen density of the oxygen-pressed film, the Perrin model equation was used [25]:

$$\ln\left(\frac{N_{0,\mathrm{N_2}}}{N_{0,\mathrm{O_2}}}\right) = \frac{4\pi}{3} r^{3}[\mathrm{O_2}], \qquad (3-1)$$

where $N_{0,\mathrm{N2}}$ is N_0 of the unpressed film, $N_{0,\mathrm{O2}}$ is N_0 of the oxygen-pressed film, and r is the quenching radius of Dexter transfer from triplet excitons to oxygen molecules. When assuming r = 1 nm, the oxygen concentration inside the oxygen-pressed film can be calculated to be 4.4×10^{20} cm^{-3}. Moreover, the molecular density of the $\mathrm{Alq_3}$ neat film is calculated to be 1.7 × 10^{21} cm^{-3} from its mass density and molecular mass [26]. Therefore, the molecular density of DCM doped in the Alq_3 film is roughly estimated to be about 7.6 × 10^{19} cm^{-3} from the molecular density of the Alq_3 neat film (1.7 × 10^{21} cm^{-3}) and molar doping concentration of DCM [4.5 mol% (= 3 wt%)]. Comparing these values, the number of incorporated oxygen molecules in the oxygen-pressed film is clearly much higher than that of the doped DCM molecules, resulting in the effective quenching of triplet excitons.

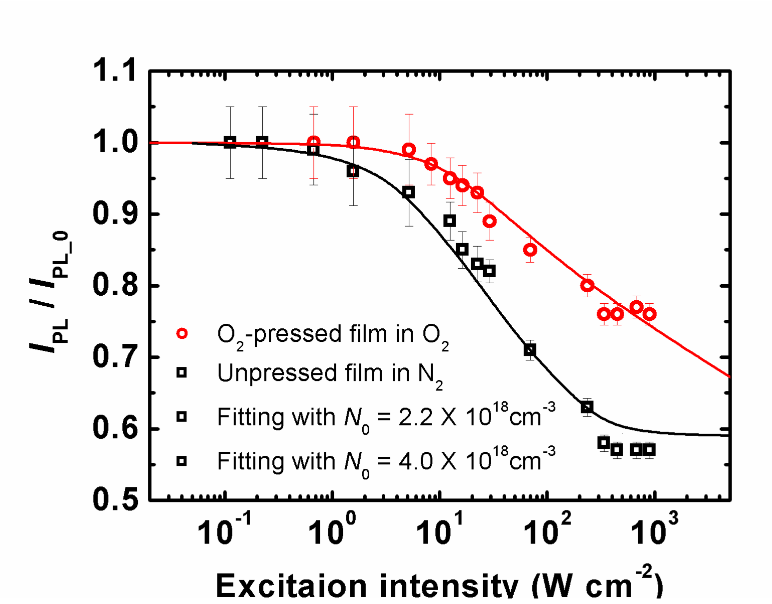

Fig. 3-6. Plots of the I_{PL}/I_{PL_0} ratios of the unressed film placed in nitrogen and oxygen-pressed film placed in oxygen as a function of excitation light intensity.

3-4. Summary

The modified CIP technique was demonstrated to be very effective for introducing oxygen into organic films. Modified CIP with oxygen enabled the STA to be effectively suppressed because triplet excitons are quenched by oxygen incorporated inside the film. Since the STA properties were independent of incidence directions of excitation light, incorporated oxygen molecules were uniformly distributed in the film. From the rate equation analysis, the oxygen density in the O_2-pressed film was estimated to be 4.4×10^{20} cm^{-3}, which is higher than the molecular density of the DCM doped in the Alq_3 film.

References

[1] Y. Zhang, M. Whited, M. E. Thompson, S. R. Forrest, Chem. Phys. Lett. **495** (2010) 161.

[2] M. Pope, H. P. Kallmann, P. Magnante, J. Chem. Phys. **38** (1963) 2042.

[3] L. J. Rothberg, A. J. Lovinger, J. Mater. Res. **11** (1996) 3174.

[4] C. Murawski, K. Leo, M. C. Gather, Adv. Mater. **25** (2013) 6801.

[5] T. G. Pavlopoulos, Prog. Quantum Electron. **26** (2002) 193.

[6] P. P. Sorokin, J. R. Lankard, IBM J. Res. Dev. **10** (1966) 162.

[7] Y. Setoguchi, C. Adachi, J. Appl. Phys. **108** (2010) 064516.

[8] M. Inoue, K. Goushi, K. Endo, H. Nomura, C. Adachi, J. Lumin. **143** (2013) 754.

[9] J. B. Marling, D. W. Gregg, L. Wood, Appl. Phys. Lett. **17** (1970) 527.

[10] R. Pappalardo, H. Samelson, A. Lempicki, Appl. Phys. Lett. **16** (1970) 267.

[11] T. Sommerfeld, J. Am. Chem. Soc. **124** (2002) 1119.

[12] S. Schols, A. Kadashchuk, P. Heremans, A. Helfer, U. Scherf, Chem. Phys. Chem. **10** (2009) 1071.

[13] J. B. Marling, D. W. Gregg, S. J. Thomas, IEEE J. Quantum Electron. QE **6** (1970) 570.

[14] K. Watanabe, E. C. Y. Inn, M. Zelikoff, J. Phys. Chem. A **101** (1997) 5509.

[15] O. G. Peterson, S. A. Tuccio, B. B. Snavely, Appl. Phys. Lett. **17** (1970) 245.

[16] C. D. Turner, M. F. Ashby, Acta. Mater. **44** (1996) 4521.

[17] D. Tadic, M. Epple, Biomaterials **24** (2003) 4565.

[18] M. Kanari, T. Wakamatsu, R. G. G. Fatt, I. Ihara, Appl. Phys. Express **4** (2011) 111603.

[19] H. D. Burrows, M. Fernandes, J. S. de Melo, A. P. Monkman, S. Navaratnam, J. Am. Chem. Soc. **125** (2003) 15310.

[20] N. C. Giebink, S. R. Forrest, Phys. Rev. B **79** (2009) 073302.

[21] S. Chénais, S. Forget, Polym. Int. **61** (2012) 390.

[22] Y. Zhang, S. R. Forrest, Phys. Rev. B **84** (2011) 241301.

[23] T. Matsushima, C. Adachi, Jpn. J. Appl. Phys. **47** (2008) 1748.

[24] M. R. Wright, R. P. Frosch, G. W. Robinson, J. Chem. Phys. **33** (1960) 934.

[25] B. C. Daglen, D. R. Tyler, Macromolecules **41** (2008) 9525.

[26] H. F. Xiang, Z. X. Xu, V. A. L. Roy, C. M. Che, P. T. Lai, Rev. Sci. Instrum. **78** (2007) 034104.

Chapter 3

Chapter 4

Low amplified spontaneous emission threshold and suppression of singlet exciton quenching in layers doped with ter(9,9’-spirobifluorene)

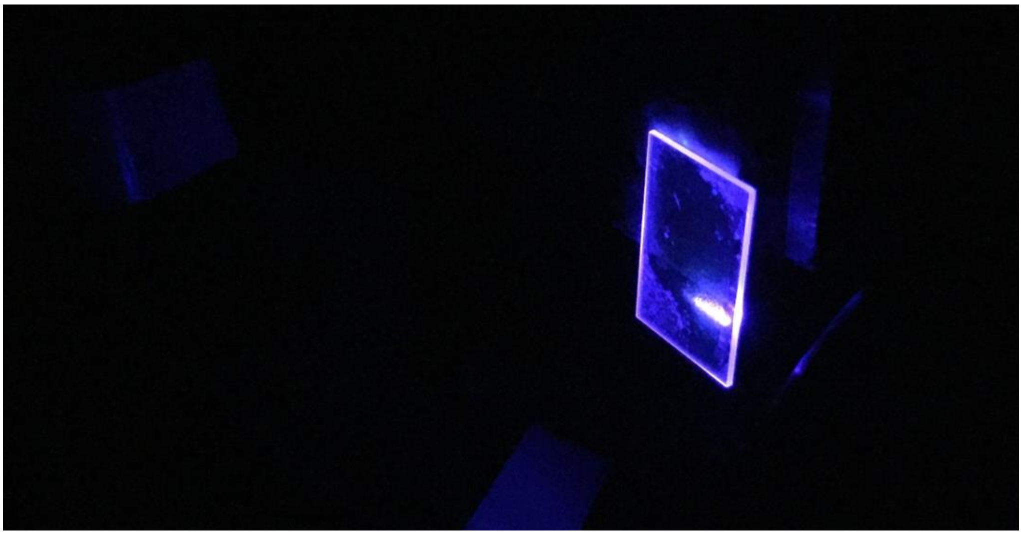

Munetomo Inoue, Toshinori Matsushima, and Chihaya Adachi

Applied Physics Letters, submitted

Abstract

The author demonstrates that TSBF doped in a host matrix layer of 4,4'-bis(carbazol-9-yl)biphenyl (CBP) shows a remarkably low ASE threshold (E_{th} = 1.0 μJ cm^{-2}) and suppressed EL efficiency roll-off at high current densities (no roll-off up to 100 mA cm^{-2}). One origin of the low ASE threshold is that the TSBF-doped CBP layer possesses a very large radiative decay constant ($k_{\mathrm{r}} = 1.1 \times 10^9$ s^{-1}). STA is almost suppressed in the TSBF-doped CBP layer, which can be ascribed to the small absorption coefficient of the triplet excitons. Also, the small energy level difference between TSBF and CBP minimizes carrier trapping in TSBF, leading to the suppression of SPA. TSBF showed one of the lowest E_{th} and the most suppressed efficiency roll-off among organic laser dyes investigated in this study and, therefore, is believed to be a promising candidate to realize electrically pumped OSLDs in the future.

4-1. Introduction

Electrically pumped OSLDs, which have many potential advantages, such as being flexible, lightweight and printable with wide tunability of emission wavelength [1-8], have not yet been realized. Many researchers have attempted to develop OSLDs and find suitable organic materials for them. However, there are still multiple critical issues that need to be addressed to realize OSLDs, including a decrease of ASE threshold [9-12], suppression of the rapid decrease of EL efficiency at high current densities, namely, roll-off [13-15], and injection of very high current density to achieve quite high exciton density in devices [16-20]. The efficiency roll-off has been ascribed to quenching of singlet excitons by other singlet excitons [singlet–singlet annihilation (SSA)], triplet excitons (STA), polarons (SPA), Joule heating (SHQ), and electric fields [13-15,21-23]. In most cases, SSA is not important for efficiency roll-off because molecules with no spectral overlap between emission and excited-state absorption can easily be obtained. In addition, singlet exciton density is much lower than the densities of triplet excitons and polarons because of the short lifetimes of singlet excitons and 25% branching ratio of singlet excitons under electrical excitation [22]. In contrast, STA and SPA strongly induce efficiency roll-off because the densities of polarons and triplet excitons are quite high [13,15,22]. Therefore, the decrease of ASE threshold and suppression of efficiency roll-off are crucial for lowering current threshold to realize ASE under electrical excitation. It has been well established that ASE threshold can be lowered by using an organic laser dye with a large k_r on the basis of an established theory [24] [Eqs. A4-1 – A4-4 in Appendix A on page 76]; i.e., a proportional relationship exists between ASE threshold and $1+k_{nr}k_r^{-1}$.

In a previous study, Adachi et al., demonstrated that BSB-Cz shows an extremely low ASE threshold [9]. In this study, the author investigates the ASE characteristics and efficiency roll-off behavior of various organic laser dyes including BSB-Cz. Among the organic laser dyes the author examines, the author finds that TSBF has superior characteristics to BSB-Cz. TSBF shows the most suppressed efficiency roll-off of the dyes considered, with almost perfectly suppressed STA, while the ASE thresholds of TSBF and BSB-Cz are very similar.

4-2. Experimental

Figure 4-1(a) shows the molecular structures of the laser dyes: TSBF, BSB-Cz, 4,4’-bis[4-(diphenylamino)styryl]biphenyl (BDAVBi), 2,3,6,7-tetrahydro-1,1,7,7-tetramethyl-1*H*,5*H*,11*H*-10-(2-benzothiazolyl)quinolizino[9,9a,1gh]coumarin (C545T), DCM, DCM2, and 4-(di-cyanomethylene)-2-tert-butyl-6-(1,1,7,7-tetramethyljulolidin-4-yl-vinyl)-4H-pyran (DCJTB). OLEDs containing the laser dyes as emitters with a structure of glass substrate / ITO anode layer (100 nm) / α-NPD HTL (35 nm) / mCP EBL (10 nm) / 3 wt% laser dye-doped CBP EML (15 nm) / PPT HBL (10 nm) / TPBi ETL (40 nm) / LiF electron injection layer (0.8 nm) / Al cathode layer (100 nm) were fabricated by conventional vacuum deposition with the deposition rates of 0.1–0.15 nm s^{-1} for the organic layers, 0.01 nm s^{-1} for LiF and 0.1–0.2 nm s^{-1} for Al under a base pressure of around 7×10^{-4} Pa. The molecular structures of all the materials are shown in Fig. 4-1(b). Glass substrates pre-coated with the ITO layers were purchased from Atsugi Micro Co. and cleaned by conventional ultrasonication and UV-ozone treatment before use. The device size was 2 × 2 mm. Steady-state J-V-η_{EQE} characteristics and EL spectra of the OLEDs under direct current (DC) condition were measured using an integrating sphere connected to a source meter (2400, Keithley Instruments) and a photonic multichannel analyzer (PMA-12, Hamamatsu Photonics). The same OLEDs were pulse-driven using a pulse generator (WF 1974, NF Co) and photomultiplier tube (C9525-02, Hamamatsu Photonics) with a pulse width of 50 μs and repetition frequency of 0.5 Hz.

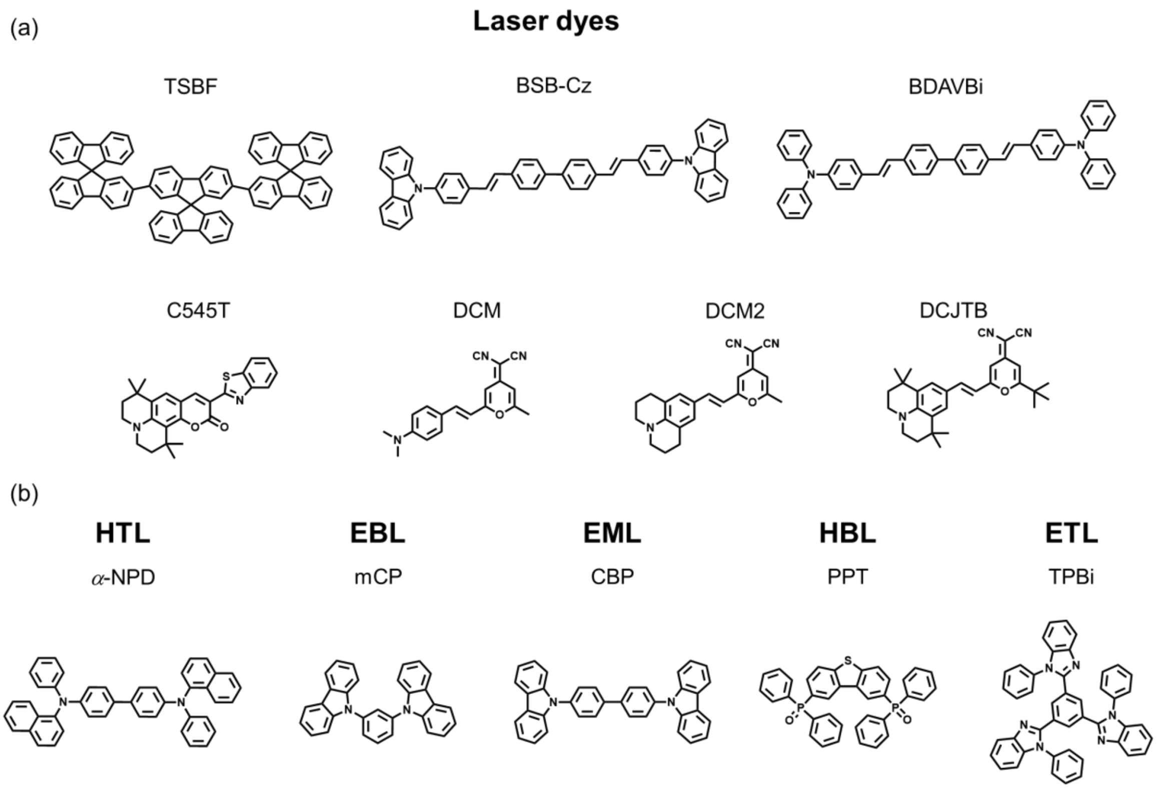

Figure 4-1. Molecular structures of (a) TSBF, BSB-Cz, BDAVBi, C545T, DCM, DCM2, DCJTB, (b) α-NPD, mCP, CBP, PPT, and TPBi.

Table 4-1. Summary of Φ_{PL}, τ, k_{r}, k_{nr}, E_{th}, and λ_{ASE} of the CBP films doped with 3 wt% of different laser dyes.

Dye	Φ_{PL} [%]	τ [ns]	k_{r} [10^8 s^{-1}]	k_{nr} [10^8 s^{-1}]	E_{th} [μJ cm^{-2}]	λ_{ASE} [nm]
TSBF	87	0.8	10.9	1.6	1.0	426
BSB-Cz	90	0.9	10.0	1.1	0.9	465
BDAVBi	88	1.2	7.3	1.0	1.5	497
C545T	80	3.1	2.6	0.65	3.1	543
DCJTB	46	2.2	2.1	2.5	7.0	624
DCM2	47	2.2	2.1	2.4	6.5	623
DCM	37	2.0	1.9	3.2	11	620

PL spectra and Φ_{PL} of 100-nm-thick CBP films doped with 3 wt% of the laser dyes, which were vacuum-deposited on quartz substrates in the same manner as for the OLED fabrication, were measured with a spectrofluorometer (FluoroMax-4, Horiba Jobin Yvon) and PLQY measurement system (C9920-02, Hamamatsu Photonics), respectively. τ of the doped films were measured under vacuum using a streak camera (C4334 or C10627, Hamamatsu Photonics) and a nitrogen gas laser (MNL200, USHO) with an excitation wavelength of 337 nm, pulse width of 500 ps, and repetition rate of 20 Hz or a Ti-sapphire laser (Millennia Prime, Spectra Physics) with an excitation wavelength of 378 nm, pulse width of 10 ps, and repetition rate of 80 MHz as an excitation source. The k_{r} and k_{nr} were calculated from the values of Φ_{PL} and τ by using the equations of $\Phi_{\mathrm{PL}} = \tau k_{\mathrm{r}}$ and $\tau = (k_{\mathrm{r}}+k_{\mathrm{nr}})^{-1}$. For the ASE measurement, 3 wt% dye-doped CBP films were vacuum-deposited on glass substrates. The nitrogen gas laser was used as the excitation source with an excitation wavelength of 337 nm, pulse width of 800 ps and repetition rate of 8 Hz. The excitation light with a stripe shape with dimensions of 0.08 × 2 cm was irradiated onto the doped films normal to the substrate, and the ASE properties were measured from a substrate edge using a photonic multichannel analyzer (PMA-11, Hamamatsu Photonics). The important optical parameters Φ_{PL}, τ, k_{r}, k_{nr}, E_{th}, and λ_{ASE} for the dyes are summarized in Table 4-1. E_{th} and λ_{ASE} stand for ASE threshold energies and wavelengths of ASE. For the estimation of the highest occupied molecular orbital (HOMO) levels of laser dyes, neat films of laser dyes were prepared and measured by using an ultraviolet photoelectron spectroscope (AC-3, Riken Keiki). The energy gaps of laser dyes were estimated from the results of absorption spectra’s edge measured. The lowest unoccupied molecular orbital (LUMO) levels were calculated from the results of HOMO levels and energy gaps. For the transient absorption measurements, solutions of the laser dyes with a concentration of 1–5 × 10^{-5} M in dichloromethane were prepared. Pump light from a Nd:YAG laser (355 nm, 10 Hz, 5–8 ns pulse width) and probe light from a xenon lamp were irradiated onto the solutions at the same time. Time-resolved transient absorption spectra of triplet excitons in the solutions were measured with and without the pump light irradiation using a streak camera system (C8484-03G, Hamamatsu Photonics) and HPD-TA 8.3.0 software (Hamamatsu Photonics).

4-3. Results and discussion

4-3-1. Amplified spontaneous emission characteristics

Figures 4-2 and 4-3 display ASE spectra and plots of the emission intensity and full width at half maximum (FWHM) of the PL spectra of the doped films as a function of excitation light intensity, respectively. At certain excitation light intensities, all the laser dyes showed light amplification with a narrowing of FWHM. Table 4-1 (page 55) summarizes E_{th} estimated from the intersection of the two straight lines used for fitting in the low and high excitation intensity regions and λ_{ASE} obtained from the ASE spectra measured beyond E_{th}.

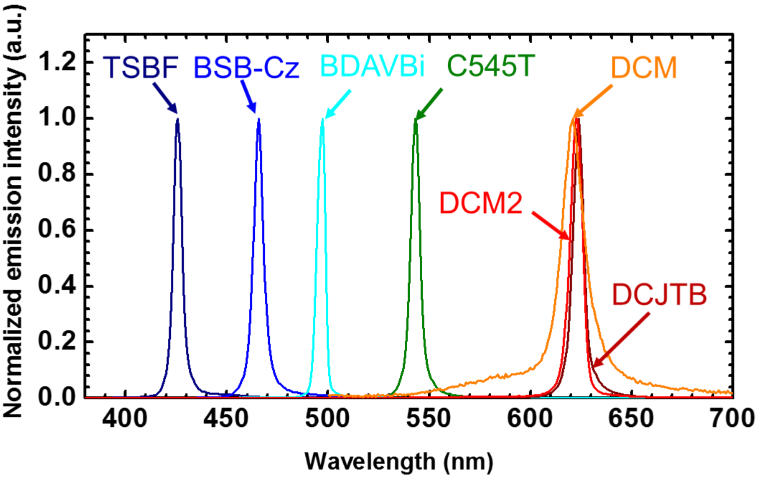

Figure 4-2. ASE spectra of 100-nm-thick CBP films doped with 3 wt% TSBF, BSB-Cz, BDAVBi, C545T, DCM, DCM2, and DCJTB. The excitation light intensities used to measure the ASE spectra were 20 μJ cm^{-2} for TSBF, BSB-Cz, BDAVBi, and C545T and 50 μJ cm^{-2} for C545T, DCM, DCM2, and DCJTB.

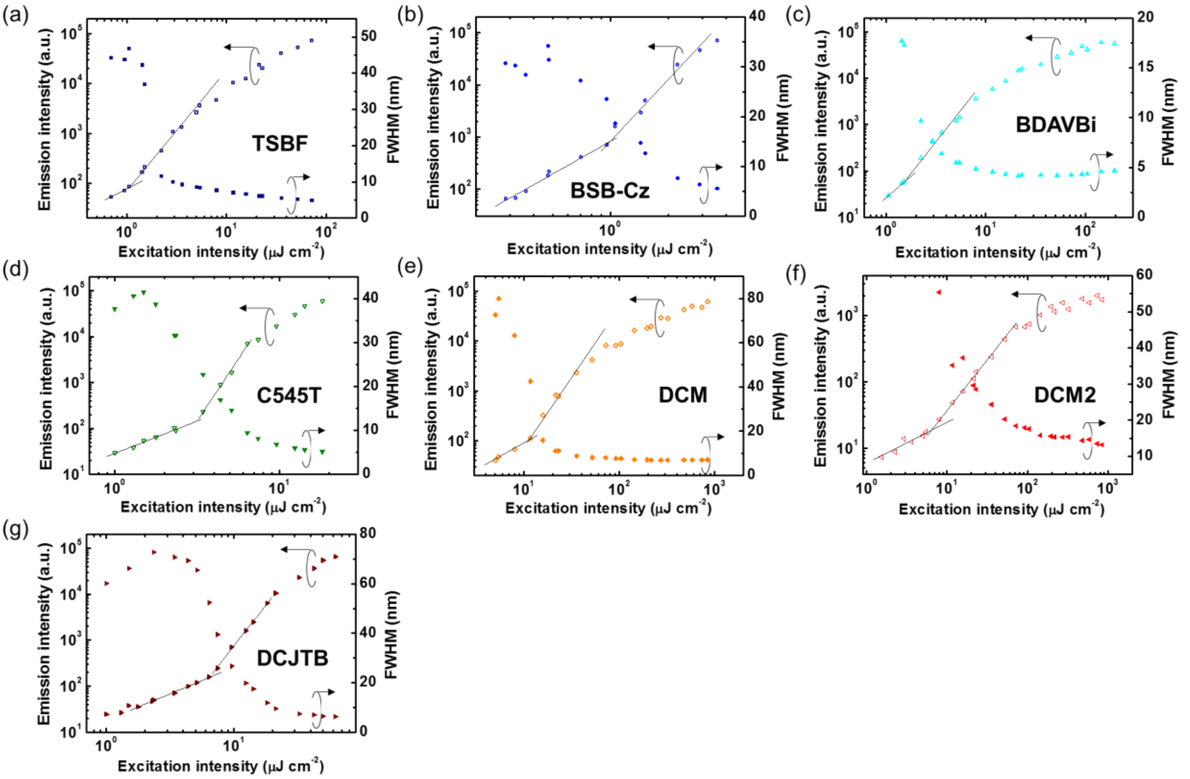

Figure 4-3. Plots of emission intensity and FWHM as a function of excitation light intensity for 100-nm-thick CBP films doped with 3 wt% (a) TSBF, (b) BSB-Cz, (c) BDAVBi, (d) C545T, (e) DCM, (f) DCM2, and (g) DCJTB. The E_{th} values summarized in Table 4-1 were estimated from the intersection of the two solid lines for the emission intensities in each figure.

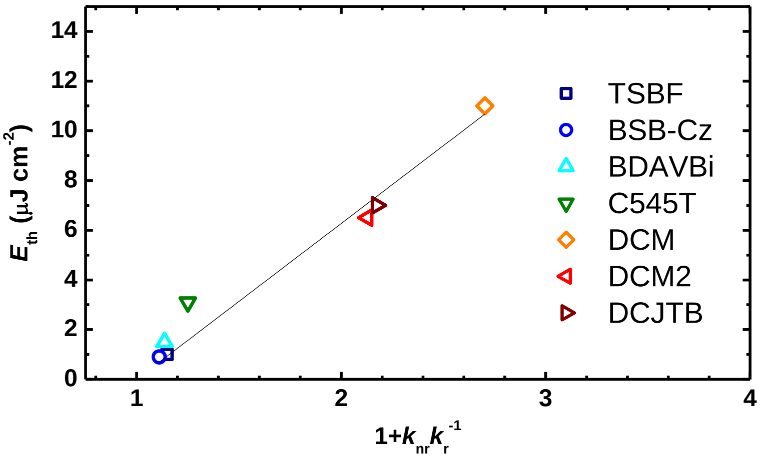

Figure 4-4. Plots of E_{th} *versus* $1 + k_{\mathrm{nr}}k_{\mathrm{r}}^{-1}$ for the laser dye-doped CBP films.

The almost linear correlation between E_{th} and $1 + k_{\mathrm{nr}}k_{\mathrm{r}}^{-1}$ of the films as shown in Fig. 4-4 clearly indicates that a larger k_{r} causes E_{th} to decrease, which agrees with this expectation according to the theoretical equation described in Appendix A. The author notes that both TSBF and BSB-Cz have very low E_{th} of close to 1.0 μJ cm^{-2} [Table 4-1] due to their quite high k_{r}. For obtaining a large k_{r}, the molecular design to enhance oscillator strength is important [25]. In fact, oligofluorene derivatives showed a large k_{r} and a large oscillator strength due to the large overlaps between the HOMO and LUMO on the fluorene units [26]. Therefore, TSBF also has the large overlaps between the HOMO and LUMO, leading to the large k_{r}.

4-3-2. Efficiency roll-off characteristics

When the OLEDs were operated under DC conditions, some devices showed breakdown at around 1 A cm^{-2} and strong roll-off behavior was observed for all the OLEDs [Fig. 4-5(a) and (b)]. These characteristics can mainly be ascribed to Joule heating-induced device breakdown combined with the presence of unwanted pinholes [17].

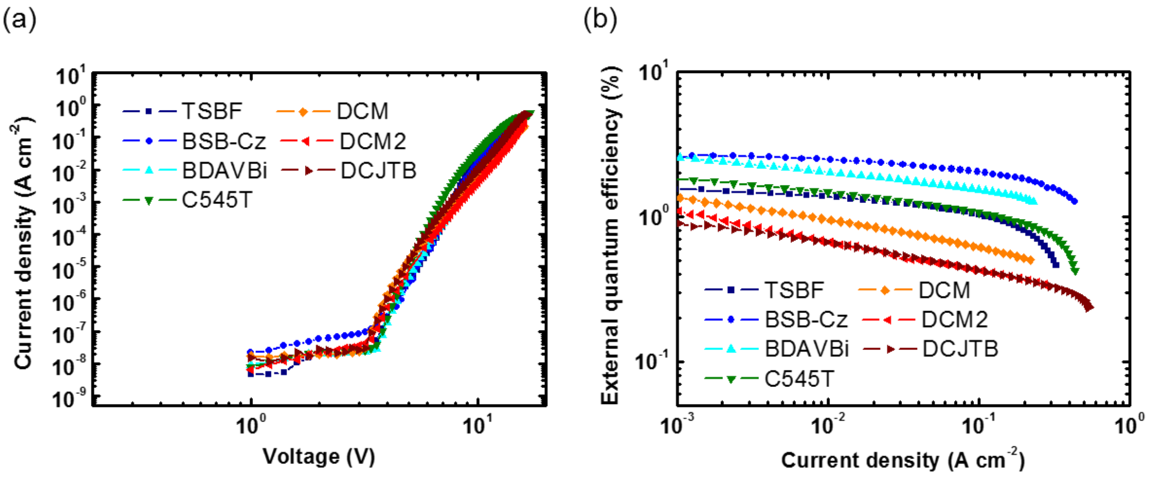

Figure 4-5. (a) J-V and (b) η_{EQE}-J characteristics of OLEDs containing the laser dyes as emitters operated under DC-driven conditions.

To relax Joule heating, the OLEDs were pulse-driven, resulting in injection of higher current density approaching 10 A cm^{-2} [Fig. 4-6(a)] and the observation of a clear difference of roll-off characteristics at high current densities [Fig. 4-6(b)]. Pulse-driven operation made it possible to compare the roll-off characteristics of the devices because of the reduced influence of Joule heating compared with that under DC operation. At low current densities, the J-V characteristics of the DC- and pulse-driven OLEDs agreed with each other [Fig. 4-7]. To quantitatively analyze the roll-off characteristics of the OLEDs, the author estimated J_{60} (the current density where η_{EQE} decreases to 60% of the initial η_{EQE}) for each OLED, the values of which are summarized in Fig. 4-6(c). The OLEDs with TSBF showed the largest J_{60} of those examined. Using TSBF increased J_{60} by about 10 and 100 times compared with that of BSB-Cz and DCM. A decrease in carrier balance factor should not be the main reason for the efficiency roll-off because the double heterostructured device architecture shown in Fig. 4-6(d) ensures balanced injection and transport of electrons and holes.

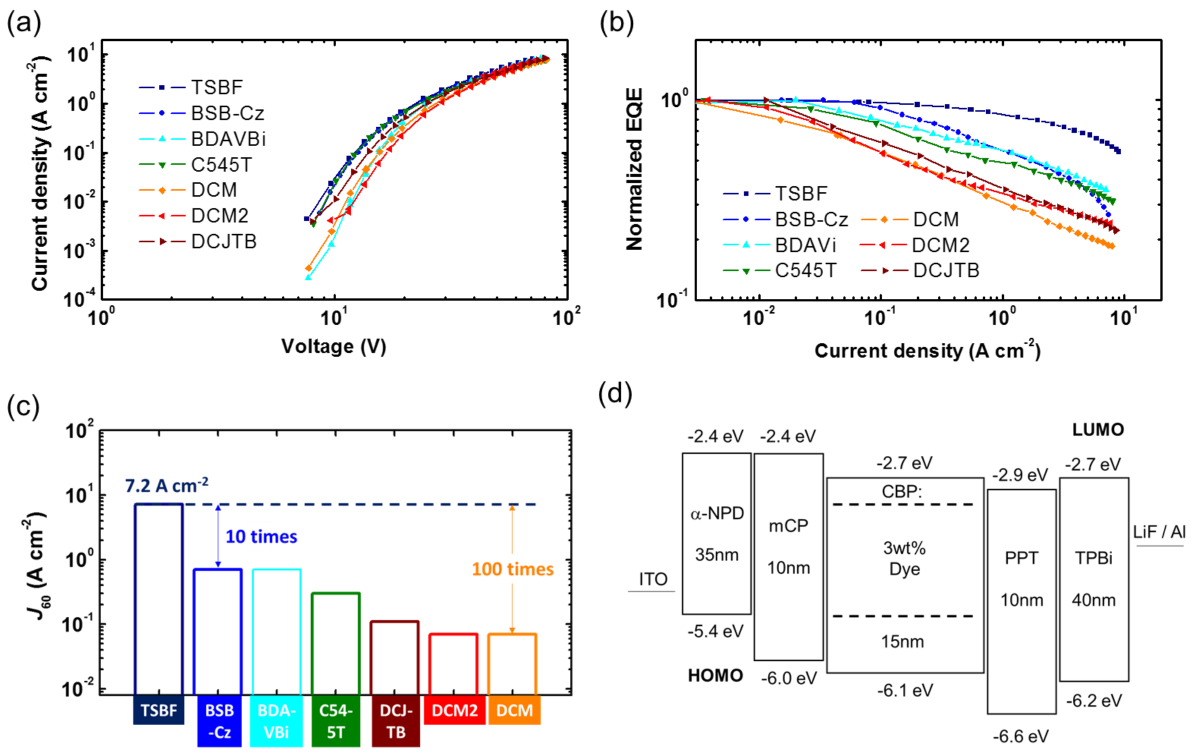

Figure 4-6. (a) *J*-*V* and (b) η_{EQE}-*J* characteristics and (c) J_{60} values of OLEDs containing the laser dyes operated under pulse-driven conditions and (d) energy level diagrams of OLEDs.

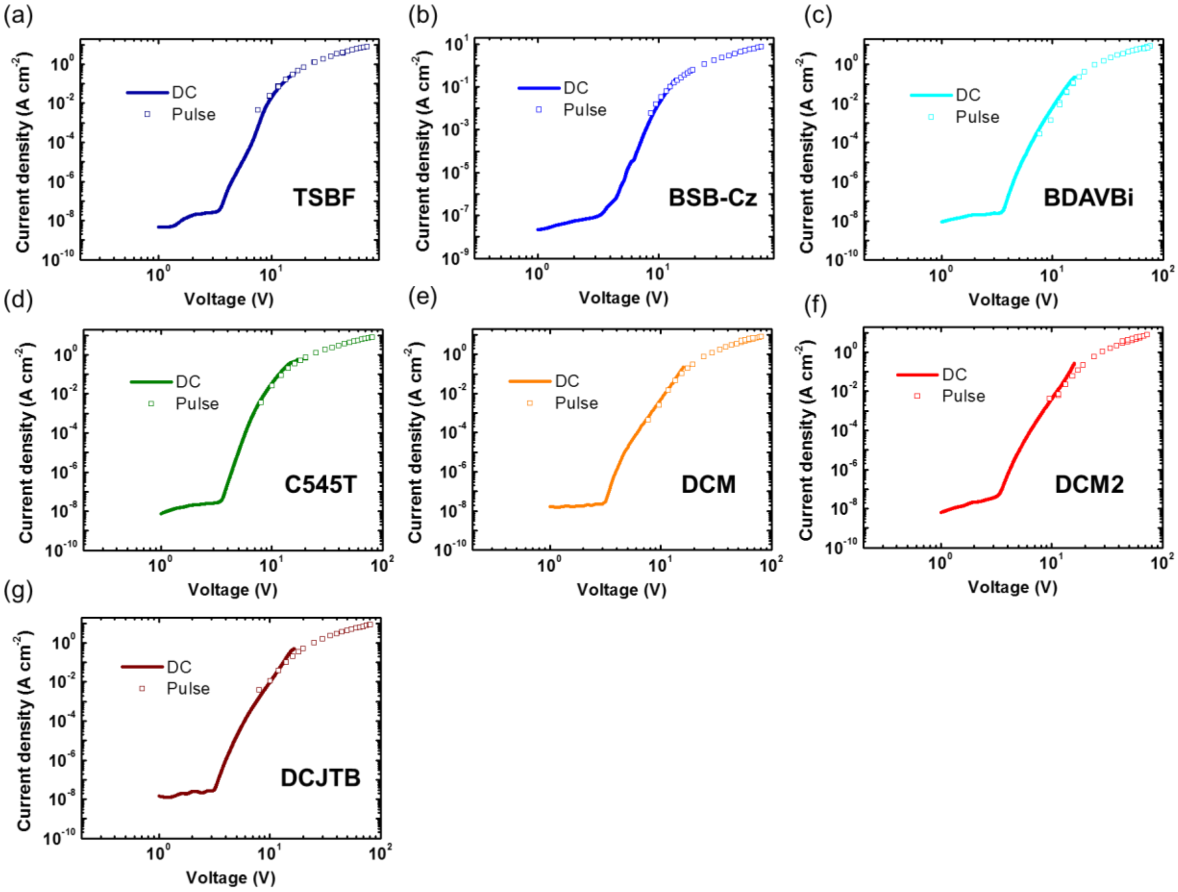

Figure 4-7. *J*-*V* characteristics of OLEDs containing (a) TSBF, (b) BSB-Cz, (c) BDAVBi, (d) C545T, (e) DCM, (f) DCM2, and (g) DCJTB as emitters operated under DC- and pulse-driven conditions.

4-3-3. Investigation of efficiency roll-off

To further investigate the roll-off characteristics of the devices, the author evaluated the transient EQE responses of the OLEDs during long electrical pulse excitation for 50 μs, which were obtained by dividing the transient EL intensity responses by the steady-state current densities at 50 μs. Figures 4-8(a) and 4-8(b) depict representative transient EQE responses of OLEDs containing TSBF and DCM2 as emitters, which were measured at current densities of 0.003–0.004 A cm^{-2} with no efficiency roll-off and at 3.0–3.2 A cm^{-2} after efficiency roll-off, respectively. All of the transient EQE responses of the OLEDs are shown in Fig. 4-9. Under weak excitation of 0.003–0.004 A cm^{-2}, the EQE of both OLEDs gradually increased and was saturated at around 50 μs. Thus, this EQE at 50 μs corresponds to the initial η_{EQE} ($\eta_{\mathrm{EQE,initial}}$) of the OLEDs operated at 0.003–0.004 A cm^{-2} with no efficiency roll-off. Conversely, in the case of high current excitation at 3.0–3.2 A cm^{-2}, the EQE abruptly lowered after the initial spike and decrease, and became constant at around 50 μs. This behavior can be ascribed to numerous triplet excitons with long lifetimes that accumulated during the long pulse excitation at high current density and effectively quenched singlet excitons [23]. This EQE at 50 μs corresponds to η_{EQE} of the OLEDs operated at 3.0–3.2 A cm^{-2}. Here, the difference between the EQE at the peak and the EQE at 50 μs measured at 3.0–3.2 A cm^{-2} is termed α_{STA} [see Fig. 4-8], corresponding to the component of EQE decreased by STA. Moreover, the difference between the EQE at the peak and EQE at 50 μs measured at 0.003–0.004 A cm^{-2} is termed α_{others}, corresponding to the proportion of EQE decreased by other quenching mechanisms, such as SPA, SHQ, and electric field-induced exciton quenching. Therefore, under steady-state conditions, η_{EQE} can be expressed as

$$\eta_{\mathrm{EQE}} = \eta_{\mathrm{EQE,\,initial}} - \alpha_{\mathrm{STA}} - \alpha_{\mathrm{others}}\,. \qquad (4\text{-}1)$$

The transient EQE responses of the other OLEDs were measured [Fig. 4-9] to obtain the values of $\alpha_{\mathrm{STA}}+\alpha_{\mathrm{others}}$, α_{STA} and α_{others} using the above technique, which are summarized in Fig. 4-10. Figure 4-10 reveals a tendency that laser dyes with smaller $\alpha_{\mathrm{STA}}+\alpha_{\mathrm{others}}$ show larger J_{60}. However, the author did not observe a clear relationship between J_{60} and α_{STA} or J_{60} and α_{others}, indicating that the contributions of STA, SPA, SHQ, and electrical field-induced quenching to efficiency roll-off are different for each laser dye.

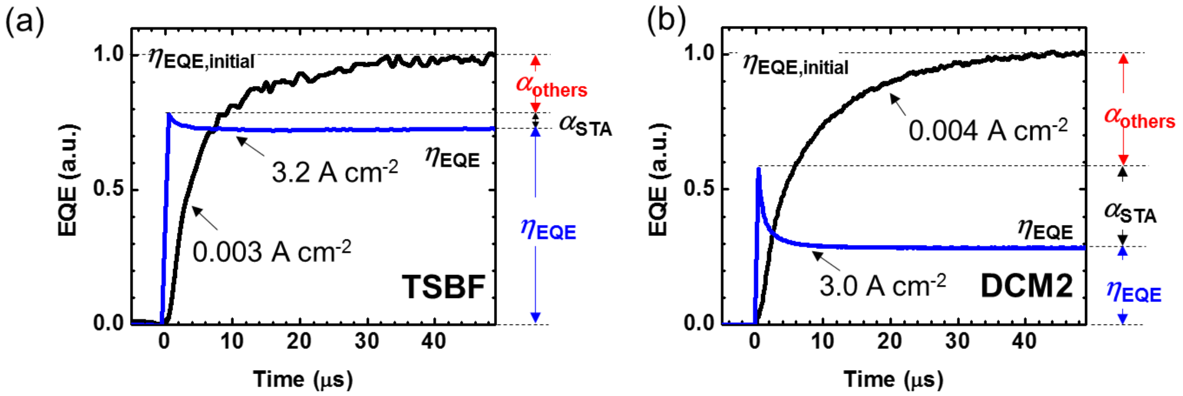

Figure 4-8. Representative transient EQE responses of OLEDs containing (a) TSBF and (b) DCM2 as emitters under 50-μs pulsed voltage excitation at current densities of 0.003–0.004 and 3.0–3.2 A cm^{-2}.

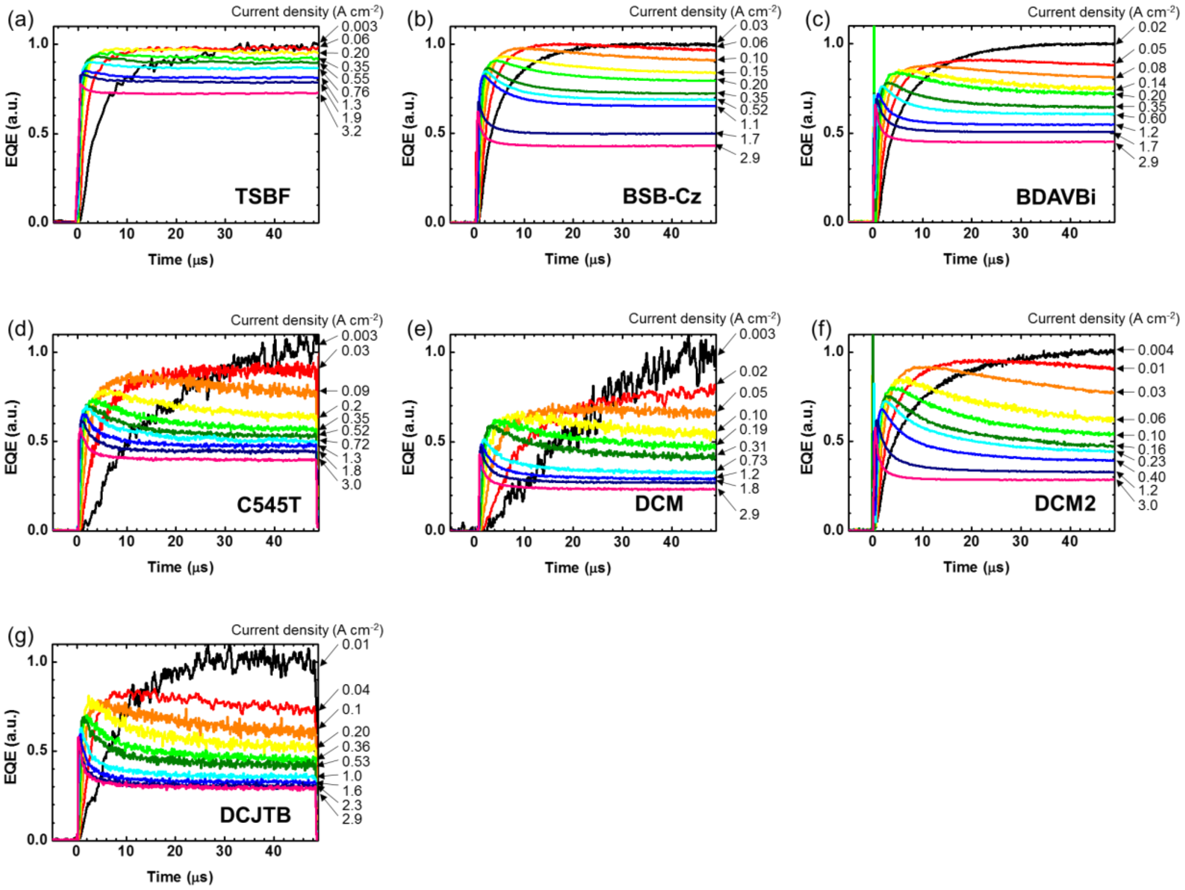

Figure 4-9. Transient EQE responses of OLEDs containing (a) TSBF, (b) BSB-Cz, (c) BDAVBi, (d) C545T, (e) DCM, (f) DCM2 and (g) DCJTB as emitters at different current densities.

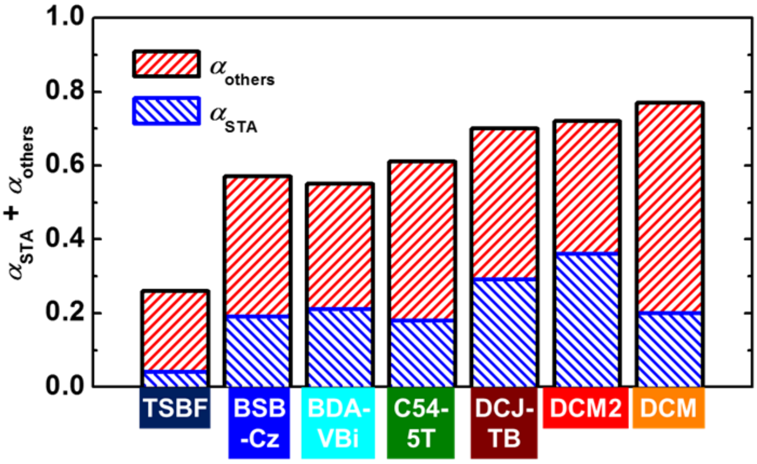

Figure 4-10. Summary of $\alpha_{STA}+\alpha_{others}$, α_{STA}, and α_{others} values of the OLEDs with laser dyes.

4-3-4. Origin of suppressed efficiency roll-off

The OLEDs with TSBF exhibited quite small α_{STA} compared with those of the OLEDs containing the other dyes as shown in Fig. 4-10. Because the spectral overlap between emission and triplet absorption is an important factor that governs STA [27-29], the transient absorption spectra of triplet excitons were measured using solutions containing the laser dyes [Fig. 4-11]. All solutions displayed spectral overlaps between emission and transient absorption spectra. Here, it is important to estimate the absorption coefficient of triplet excitons to quantify the STA efficiency. However, the estimation of absorption coefficient was unsuccessful because it was difficult to precisely calculate the number of triplet excitons formed in the solutions under the pump light irradiation. However, according to the experimental results, the author stresses that because α_{STA} is only 0.04 for the OLEDs with TSBF, STA is almost suppressed in these devices. Meanwhile, the OLEDs with BSB-Cz, which show the second-highest suppression of efficiency roll-off of the devices, have a larger α_{STA} of 0.19 than TSBF. However, the densities of triplet excitons are supposed to be same in TSBF and BSB-Cz because the lifetime of triplet excitons are almost same in TSBF and BSB-Cz. Therefore, the author supposes that the difference between α_{STA} of TSBF and BSB-Cz is because of the small absorption coefficient of triplet excitons of TSBF. For further investigation of the STA efficiency, transient PL responses in dye-doped films were measured as shown in Fig. 4-12. In the PL responses, the STA efficiency without the effect of charge carriers can be discussed. The smallest PL decrease was observed in the TSBF-doped film and the second smallest STA efficiency was observed in the BSB-Cz-doped film, showing similar trend comparing to the results of the transient EQE responses.

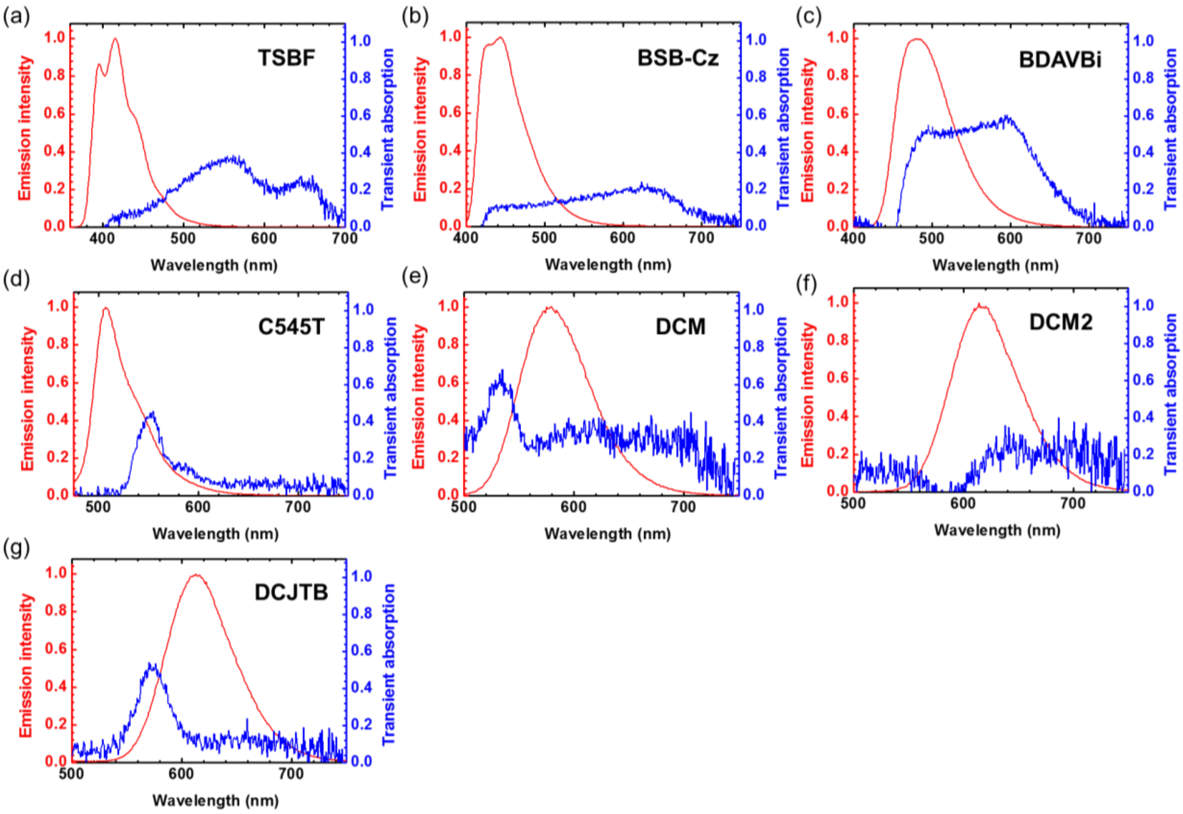

Figure 4-11. Emission (red) and transient absorption (blue) spectra of dichloromethane solutions of (a) TSBF, (b) BSB-Cz, (c) BDAVBi, (d) C545T, (e) DCM, (f) DCM2, and (g) DCJTB. Transient absorption spectra were obtained in the time range from 0.1 to 1 ms after the pump excitation.

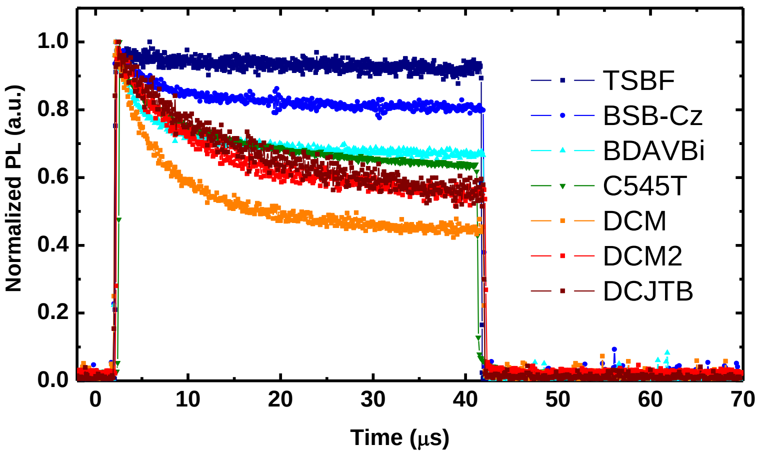

Figure 4-12. Transient PL response of the doped films under pulse light excitation at a pump intensity of 100 W cm^{-2}.

In addition, α_{others} of the OLEDs with TSBF was also small compared with those of the OLEDs containing the other dyes. The values of $\alpha_{\mathrm{STA}}+\alpha_{\mathrm{others}}$, α_{STA}, and α_{others}, are summarized in Table 4-2. Two factors are considered to cause the small α_{others} for TSBF. The first factor is the low possibility of carrier trapping in TSBF doped in CBP. HOMO and LUMO levels of dopant molecules often lie inside those of a host layer. In such a case, strong carrier trapping in the dopants takes place, resulting in the occurrence of strong SPA because the number of carriers (polarons) in the carrier recombination zone becomes high [30]. In fact, T. Matsushima and C. Adachi previously demonstrated that the energy level alignment of HOMO and LUMO levels of dopant and host molecules leads to suppressed efficiency roll-off caused by SPA [31]. To examine the carrier trapping behavior of the OLEDs, the author estimated the HOMO–HOMO difference (ΔE_{HOMO}) and LUMO–LUMO difference (ΔE_{LUMO}) between each laser dye and CBP [see Table 4-2]. Because the TSBF-doped CBP layer has the smallest $\Delta E_{\mathrm{HOMO}} = 0.08$ eV and $\Delta E_{\mathrm{LUMO}} = 0.06$ eV of the dye-doped CBP layers, the STA induced by carrier trapping can be minimized.

The other factor that results in the small α_{others} for TSBF is its large k_{r}. SPA and STA generally occur through a Förster-type energy transfer process [27-29]; therefore, rate constants of SPA and STA are proportional to k_{r} when considering the previously established theory [27-29] [see Eqs. (A4-5) – (A4-7) in Appendix A on page, 76 and 77]. On the other hands, if k_{r} of a laser dye is large enough to allow prompt emission before singlet excitons are quenched, SHQ and electrical field-induced quenching can be suppressed. Therefore, the author supposes that the large k_{r} of TSBF can overcome the SHQ and electrical field-induced quenching in the TSBF-doped CBP films because k_{r} of TSBF is the highest of the dyes, as shown in Table 4-2. Especially, SHQ is expected to be perfectly suppressed because TSBF shows the temperature-independence of PLQYs, originated from the quite high k_r like BSB-Cz [9].

Table 4-2. Summary of J_{60}, $\alpha_{STA}+\alpha_{others}$, α_{STA}, α_{others}, HOMO, LUMO, ΔE_{HOMO}, ΔE_{LUMO}, and k_r of the laser dyes. ΔE_{HOMO} and ΔE_{LUMO} represent HOMO–HOMO and LUMO–LUMO differences between the laser dyes and CBP, where the HOMO and LUMO of CBP are −6.08 and −2.68 eV, respectively.

	J_{60} [A cm^{-2}]	$\alpha_{STA}+\alpha_{others}$	α_{STA}	α_{others}	HOMO [eV]	LUMO [eV]	ΔE_{HOMO} [eV]	ΔE_{LUMO} [eV]	k_r [10^8 s^{-1}]
TSBF	7.2	0.26	0.04	0.22	-6.00	-2.74	0.08	0.06	10.9
BSB-Cz	0.7	0.57	0.19	0.38	-5.90	-3.05	0.18	0.37	10.0
BDAVBi	0.7	0.55	0.21	0.34	-5.49	-2.74	0.59	0.06	7.3
C545T	0.3	0.61	0.18	0.43	-5.46	-3.03	0.62	0.35	2.6
DCJTB	0.1	0.70	0.29	0.41	-5.25	-3.11	0.83	0.43	2.1
DCM2	0.07	0.72	0.36	0.36	-5.40	-3.26	0.68	0.58	2.1
DCM	0.07	0.77	0.20	0.57	-5.49	-3.19	0.59	0.51	1.9

4-3-5. Efficiency roll-off under extremely high current

The author demonstrated that the OLEDs with TSBF show the most suppressed efficiency roll-off behavior among those with the other laser dyes investigated in this study. To understand the achievable singlet exciton density, the TSBF-based OLEDs with quite small active areas (0.04 and 0.0004 cm^{-2}) were operated under quite short pulse widths (50, 5, and 0.5 μs). The author assumes that the OLED breakdown observed at high current densities and voltages is caused by melting of organic layers due to Joule heating. The Joule heating-induced breakdown is suppressed by a reduction of device active areas and use of high-thermal-conductivity substrates and short pulse voltages because of suppressed Joule heating [13,31]. The J-V and η_{EQE}-J characteristics of the TSBF-based OLEDs with the active areas of 0.04 and 0.0004 cm^{-2} are displayed in Fig. 4-13. At the low current densities, the J-V and η_{EQE}-J characteristics of both the OLEDs agreed each other. Use of the smaller active area and shorter pulse width enabled injection of higher current density approaching 1 kA cm^{-2} with the efficiency roll-off. Here, the author compares the efficiency roll-off of the TSBF-based OLEDs with those of the previously reported BSB-Cz-based OLEDs with a nano-patterned or special single-layer architecture which are known to show significantly suppressed efficiency roll-off under high current density [13,15]. Figure 4-14 (a) and (b) show the efficiency roll-off characteristics of the TSBF- and BSB-Cz-based OLEDs. The active area (S), pulse width, and η_{EQE}, $\eta_{\mathrm{EQE}}/\eta_{\mathrm{EQE,max}}$ and singlet exciton densities under electrical excitation at certain current densities ($N^{\mathrm{S}}_{\mathrm{EL}}$), and singlet exciton densities estimated from the ASE thresholds under optical excitation ($N^{\mathrm{S}}_{\mathrm{th}}$) are summarized in Table 4-3. $N^{\mathrm{S}}_{\mathrm{EL}}$ and $N^{\mathrm{S}}_{\mathrm{th}}$ were calculated by using previously reported equations [13] [see A4-8 and A4-9 in Appendix A on page 75]. The current densities of around 100, 550, and 2000 A cm^{-2} were chose in

Table 4-3 because the TSBF-based OLEDs, nano-patterned OLEDs, and single-layer OLEDs reached the maximum current densities of around 550, 2000, and 100 A cm^{-2}, respectively. Since the nano-patterned OLEDs have nano-size active areas, they exhibit the highest current density among the three devices. Moreover, the nano-patterned OLEDs strongly suppressed efficiency roll-off because some singlet excitons can partly escape from a carrier flow and exciton generation region where SPA and STA occur [Figs. 4-14(b) and (c)] [15]. In the previous study, it is well established that the accumulation of carriers in the EML is suppressed in the single-layer OLEDs because of no hetero-interfaces included, resulting in suppression of SPA and efficiency roll-off as well [Figs. 4-14(b) and (d)] [13]. Whereas the TSBF-based OLEDs is a conventional multilayers device structure, they showed the similar $\eta_{\rm EQE}/\eta_{\rm EQE,max}$ values to those of the BSB-Cz-based nano-patterned and single-layer OLEDs at the similar current densities [Fig. 4-14(a)], indicating that charge trapping is well suppressed in the multilayered TSBF- OLEDs. Moreover, $N^{\rm S}_{\rm EL}$ of the TSBF-based OLEDs at 553 A cm^{-2} was 4.8 × 10^{24} cm^{-3} s^{-1}, indicating that the difference between $N^{\rm S}_{\rm EL}$ and $N^{\rm S}_{\rm th}$ is getting the closer value of 60. After the further suppression of efficiency roll-off and/or the reduction of ASE threshold, the author expects to realize electrical lasing.

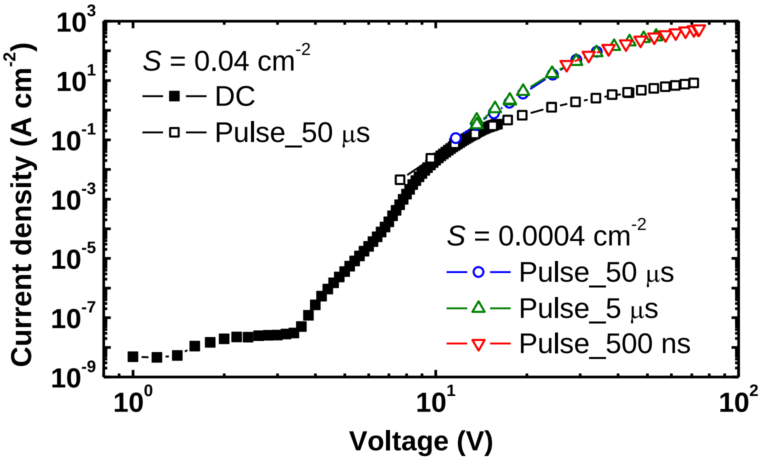

Figure 4-13. *J-V* characteristics of OLEDs containing TSBF operated under DC- and pulse-driven conditions.

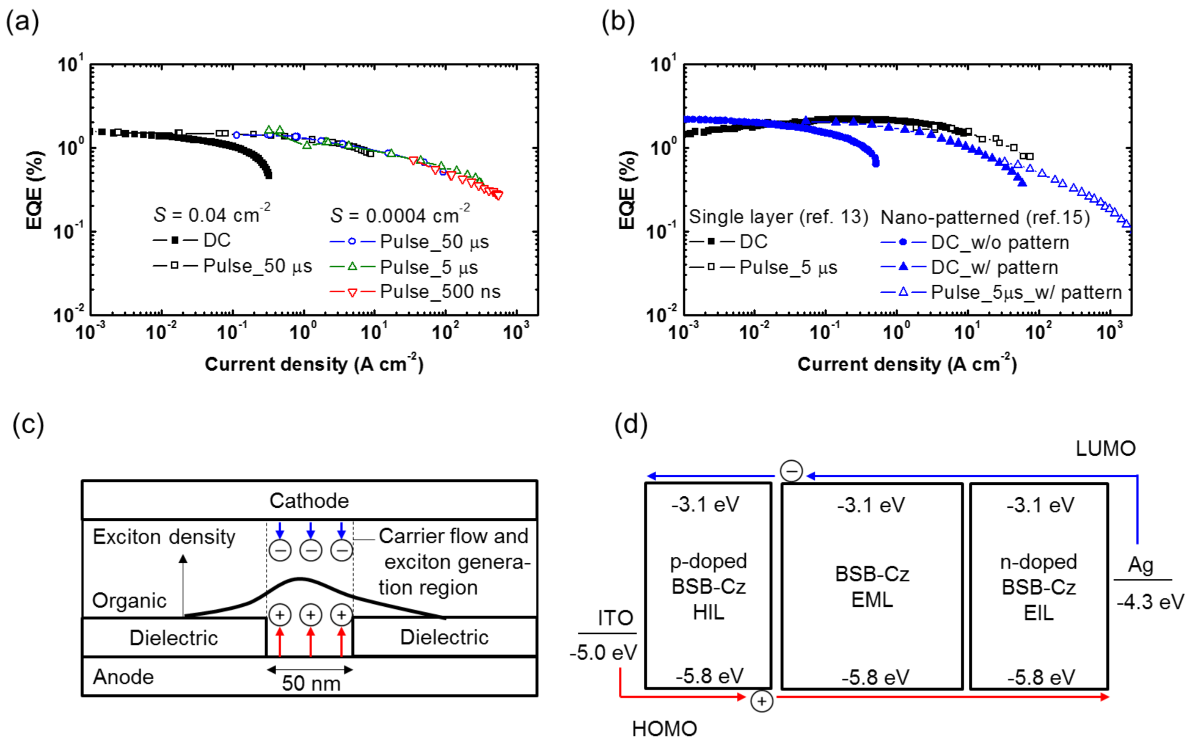

Figure 4-14. η_{EQE}-J characteristics of (a) TSBF-based OLEDs and (b) BSB-Cz-based OLEDs with nano-patterned and single-layer architectures operated under DC- and pulse-driving conditions. Illustrations of the device structures with (c) nano-patterned and (d) single-layer architectures. The plots in (b) were obtained from refs. [13] and [15]. HIL and EIL in (d) stand for a hole injection layer and electron injection layer, respectively.

Table 4-3. Summary of S, pulse width, J, η_{EQE}, $\eta_{\mathrm{EQE}}/\eta_{\mathrm{EQE,max}}$, N^{S}_{EL}, and N^{S}_{th} of the TSBF and BSB-Cz-based OLEDs.

Emitter	Structure	S [cm^2]	Pulse width [sec]	J [A cm^{-2}]	η_{EQE} [%]	η_{EQE} / $\eta_{\mathrm{EQE,max}}$	N^{S}_{EL} [10^{24} cm^{-3} s^{-1}]	N^{S}_{th} [10^{26} cm^{-3} s^{-1}]
TSBF	Double-hetero	4×10^{-4}	5×10^{-7}	100	0.50	0.34	1.6	2.7
				553	0.27	0.18	4.8	
BSB-Cz (ref. 15)	Nano-patterned	1×10^{-6}	5×10^{-6}	550	0.26	0.12	3.7	2.3
				2000	0.10	0.05	5.3	
BSB-Cz (ref. 13)	Single layer	4×10^{-4}	5×10^{-6}	100	0.77	0.36	1.1	2.3

4-4. Summary

In summary, the author demonstrated that TSBF is an excellent laser dye, displaying the highest k_r, one of the lowest E_{th}, and OLEDs with the most suppressed efficiency roll-off among the laser dyes investigated in this study. The author attributes the most suppressed efficiency roll-off of the OLEDs with TSBF to the suppression of exciton quenching by processes such as STA, SPA, and SHQ and electrical field-induced quenching, which is probably related to the small absorption coefficient of triplet excitons of TSBF, the smallest ΔE_{HOMO} and ΔE_{LUMO} between TSBF and CBP, and the largest k_r of TSBF. The author believes that the remarkably low E_{th} and suppressed efficiency roll-off obtained using TSBF will lead to the realization of OSLDs in the future.

4-5. Appendix A

The ASE threshold E_{th} is given by [24]

$$E_{\mathrm{th}} = C' \frac{1}{\Gamma n_{\mathrm{F}} \Phi_{\mathrm{PL}}} \left(\int \frac{\sigma_{\mathrm{a}}}{\lambda} d\lambda \right)^{-2}, \qquad \text{(A4-1)}$$

where *C’* is the constant factor, Γ is the confinement factor, n_{F} is the refractive index in a fluorescent region, Φ_{PL} is the PL quantum efficiency, σ_{a} is the absorption cross-section, and λ is the wavelength. Here, Φ_{PL} is given by

$$\phi_{\mathrm{PL}} = \frac{k_{\mathrm{r}}}{k_{\mathrm{r}} + k_{\mathrm{nr}}}, \qquad \text{(A4-2)}$$

where k_{r} and k_{nr} are the radiative and non-radiative decay constants, respectively. Here,

$$\text{if} \quad \int \frac{\sigma_{\mathrm{a}}}{\lambda} d\lambda = \text{constant}, \qquad \text{(A4-3)}$$

E_{th} is in inverse proportion to k_{r} as shown below,

$$E_{\mathrm{th}} \propto 1 + \frac{k_{\mathrm{nr}}}{k_{\mathrm{r}}}. \qquad \text{(A4-4)}$$

The rate constants of SPA and STA (k_{A}) as described by the Förster-type energy transfer process are given by [27-29]

$$k_{\mathrm{A}} = \frac{1}{\tau} \left(\frac{r_0}{r} \right)^6, \qquad \text{(A4-5)}$$

where τ is the lifetime of singlet excitons, r_0 is the Förster radius, and r is the distance between a singlet exciton and triplet exciton (for STA) or polaron (for SPA). Here, r_0 is given by

$$r_0^6 = \frac{9000 c^4 \ln 10 k^2 \Phi_{\mathrm{PL}}}{128 \pi^5 {n_{\mathrm{F}}}^4 N_{\mathrm{A}}} \int f_{\mathrm{D}}(\nu) \varepsilon_{\mathrm{A}}(\nu) \frac{d\nu}{\nu^4}, \qquad \text{(A4-6)}$$

where c is the speed of the light, k is the orientation factor, N_{A} is the Avogadro constant, $\int f_{\mathrm{D}}(\nu) \varepsilon_{\mathrm{A}}(\nu) \frac{d\nu}{\nu^4}$ is the spectral overlap factor, $f_{\mathrm{D}}(\nu)$ is the emission spectrum shape function, and $\varepsilon_{\mathrm{A}}(\nu)$ is the molar absorption coefficient of triplet excitons (for STA) or polarons (for SPA). Here, Φ_{PL} is given by $\Phi_{\mathrm{PL}} = \tau\, k_{\mathrm{r}}$. Therefore, k_{A} is proportional to k_{r} and the spectral overlap as shown below,

$$k_{\mathrm{A}} \propto k_r \int f_{\mathrm{D}}(\nu)\varepsilon_{\mathrm{A}}(\nu)\frac{d\nu}{\nu^4}\,. \qquad \text{(A4-7)}$$

The singlet exciton density in the OLEDs under electrical excitation ($N^{\mathrm{S}}_{\mathrm{EL}}$) was calculated by using the equation [13],

$$N^{\mathrm{S}}_{\mathrm{EL}} = \frac{J}{e}\times\eta_{\mathrm{EQE}}\times\frac{1}{\eta_{\mathrm{out}}}\times\frac{1}{\Phi_{\mathrm{PL}}}\times\frac{1}{L}\,, \qquad \text{(A4-8)}$$

where e is the elementary charge, η_{out} is the light out-coupling efficiency of the OLEDs, and L is the width of waveguide. For the $N^{\mathrm{S}}_{\mathrm{EL}}$ calculation, the author assumed η_{out} = 20% [33,34]. The singlet exciton densities (N^{S}_{th}) at the E_{th} of the ASE were also calculated by using the equation [13],

$$N^{\mathrm{S}}_{\mathrm{th}} = E_{\mathrm{th}}\times\frac{\lambda_{\mathrm{ASE}}}{hc}\times\frac{1}{\tau}\times\frac{1}{d}\,, \qquad \text{(A4-9)}$$

where h is the Planck constant, c is the speed of light, and d is the thickness of the doped films.

References

[1] J. H. Burroughes, D. D. C. Bradley, A. R. Brown, R. N. Marks, K. Mackay, R. H. Friend, P. L. Burns, A. B. Holmes, Nature **347** (1990) 539.

[2] W. Holzer, A. Penzkofer, S.-H. Gong, A. Bleyer, D. D. C. Bradley, Adv. Mater. **8** (1996) 974.

[3] N. Tessler, G. J. Denton, R. H. Friend, Nature **382** (1996) 695.

[4] F. Hide, M. A. Diaz-Garcia, B. J. Schwartz, M. R. Andersson, Q. Pei, A. J. Heeger, Science **273** (1996) 1833.

[5] R. H. Friend, R. W. Gymer, A. B. Holmes, J. H. Burroughes, R. N. Marks, C. Taliani, D. D. C. Bradley, D. A. D. Santos, J. L. Bredas, M. Logdlund, W. R. Salaneck, Nature **397** (1999) 121.

[6] M. D. McGehee, A. J. Heeger, Adv. Mater. **12** (2000) 1655.

[7] T. Sekitani, H. Nakajima, H. Maeda, T. Fukushima, T. Aida, K. Hata, T. Someya, Nature **8** (2009) 494.

[8] D. S. Hecht, L. Hu, G. Irvin, Adv. Mater. **23** (2011) 1482.

[9] T. Aimono, Y. Kawamura, K. Goushi, H. Yamamoto, H. Sasabe, C. Adachi, Appl. Phys. Lett. **86** (2005) 071110.

[10] T. Oyamada, C. H. Chang, T. C. Chao, F. C. Fang, C. C. Wu, K. T. Wong, H. Sasabe, C. Adachi, J. Phys. Chem. C **111** (2007) 108.

[11] H. Nakanotani, N. Matsumoto, H. Uchiuzou, M. Nishiyama, M. Yahiro, C. Adachi, Opt. Mater. **30** (2007) 630.

[12] C. Karnutsch, C. Pflumm, G. Heliotis, J. C. deMello, D. D. Bradley, J. Wang, T. Weimann, V. Haug, C. Gärtner, U. Lemmer, Appl. Phys. Lett. **90** (2007) 131104.

[13] Y. Setoguchi, C. Adachi, J. Appl. Phys. **108** (2010) 064516.

[14] Y. Zhang, M. Slootsky, S. Forrest, Appl. Phys. Lett. **99** (2011) 223303.

[15] K. Hayashi, H. Nakanotani, M. Inoue, K. Yoshida, O. Mikhnenko, T. Q. Nguyen, C. Adachi, Appl. Phys. Lett. **106** (2015) 093301.

[16] H. Nakanotani, T. Oyamada, Y. Kawamura, H. Sasabe, C. Adachi, Jpn. J. Appl. Phys. **44** (2005) 3659.

[17] T. Matsushima, H. Sasabe, C. Adachi, Appl. Phys. Lett. **88** (2006) 033508.

[18] T. Matsushima, C. Adachi, Jpn. J. Appl. Phys. **46** (2007) L861.

[19] T. Takenobu, S. Z. Bisri, T. Takahashi, M. Yahiro, C. Adachi, Y. Iwasa, Phys. Rev. Lett. **100** (2008) 066601.

[20] K. Sawabe, T. Takenobu, S. Z. Bisri, T. Yamao, S. Hotta, Y. Iwasa, Appl. Phys. Lett. **97** (2010) 043307.

[21] H. Nakanotani, H. Sasabe, C. Adachi, Appl. Phys. Lett. **86** (2005) 213506.

[22] C. Murawski, K. Leo, M. C. Gather, Adv. Mater. **25** (2013) 6801.

[23] Y. Zhang, M. Whited, M. E. Thompson, S. R. Forrest, Chem. Phys. Lett. **495** (2010) 161.

[24] T. Komino, H. Nomura, M. Yahiro, K. Endo, C. Adachi, J. Phys. Chem. C **115** (2011) 19890.

[25] Y. Sagara, K. Shizu, H. Tanaka, H. Miyazaki, K. Goushi, H. Kaji, C. Adachi, Chem. Lett. **44** (2015) 360.

[26] E. Y. Choi, L. Mazur, L. Mager, M. Gwon, D. Pitrat, J. C. Mulatier, C. Monnereau, A. Fort, A. J. Attias, K. Dorkenoo, J. E. Kwon, Y. Xiao, K. Matczyszyn, M. Samoc, D.-W. Kim, A. Nakao, B. Heinrich, D. Hashizume, M. Uchiyama, S. Y. Park, F. Mathevet, T. Aoyama, C. Andraud, J. W. Wu, A. Barsell, J. C. Ribierre, Phys. Chem. Chem. Phys. **16**

(2014) 16941.

[27] M. Yokota, O. Tanimoto, J. Phys. Soc. **22** (1967) 779.

[28] S. M. Menke, W. A. Luhman, R. J. Holmes, Nature Mater. **12** (2013) 152.

[29] X. Liu, Y. Zhang, S. R. Forrest, Phys. Rev. B **90** (2014) 085201.

[30] Y. Luo, H. Aziz, G. Xu, Z. D. Popovic, Chem. Mater. **19** (2007) 2288.

[31] T. Matsushima and C. Adachi, Appl. Phys. Lett. **92** (2008) 063306.

[32] H. Yamamoto, H. Kasajima, W. Yokoyama, H. Sasabe, C. Adachi, Appl. Phys. Lett. **86** (2005) 083502.

[33] S. W. Liu, J. X. Wang, Y. Divayana, K. Dev, S. T. Tan, H. V. Demir, X. W. Sun, Appl. Phys. Lett. **102** (2013) 053305.

[34] Z. B. Wang, M. G. Helander, J. Qiu, D. P. Puzzo, M. T. Greiner, Z. M. Hudson, S. Wang, Z. W. Liu, Z. H. Lu, Nature Photon. **5** (2011) 753.

Chapter 5

Summary of this thesis

Summary of this thesis

In this thesis, exciton quenching processes were investigated to suppress efficiency roll-off in OLEDs through the analyses of PL and EL characteristics.

In Chapter 2, efficiency roll-off observed in OLEDs with TADF emitters was investigated. The author identified that STA and TTA induced by the accumulation of triplet excitons formed under electrical excitation are the main sources of efficiency roll-off in TADF-OLEDs. The use of ACRXTN as a TADF emitter significantly reduced triplet exciton density that induces STA and TTA because ACRXTN has an efficient RISC rate from triplet to singlet excitons due to its small ΔE_{ST}. Therefore, the OLEDs with ACRXTN showed very small efficiency roll-off. On the other hand, the OLEDs with another TADF emitter of 2CzPN showed relatively large efficiency roll-off because of the inefficient RISC associated with its large ΔE_{ST} while the maximum efficiencies before efficiency roll-off are very similar in both the OLEDs with ACRXTN and 2CzPN. In the future, a further acceleration of k_{RISC} is required to suppress efficiency roll-off completely.

In Chapter 3, a modified CIP process was developed to incorporate oxygen into organic solid films doped with laser dyes. The oxygen-incorporated films showed effective suppression of STA because oxygen is known to work as efficient triplet quenchers in organic films. The incorporated oxygen was found to be uniformly distributed in the films from the results of the dependence of incidence directions of excitation light. The concentration of the incorporated oxygen in the films was estimated by several rate equations and the Perrin model. The estimated oxygen concentration was very high beyond the concentration of the doped laser dye molecules. However, the perfect suppression of STA was not achieved here, probably because the singlet excited states of oxygen molecules generated by quenching of organic triplet excitons no longer have an ability for triplet quenching. 1,4-Diazabicyclo[2.2.2]octane (DABCO) is well-known as a quencher for singlet excited states of oxygen [1,2]. Since immediate quenching of the singlet-excited-state oxygen molecules by DABCO enables oxygen molecules to be reused as a triplet quencher [1,2], ternary mixing of organic laser dyes, oxygen, and DABCO can be useful for further suppression of STA.

In Chapter 4, roll-off characteristics of OLEDs with the laser dyes of TSBF, BSB-Cz, BDAVBi, C545T, DCM, DCM2, and DCJTB were investigated and compared. TSBF was demonstrated to most effectively suppress efficiency roll-off characteristics among the laser dyes investigated in this study through the suppression of STA, SPA, SHQ, and electric field-induced quenching, which could be ascribed to a small absorption coefficient of the triplet excitons of TSBF, little carrier trapping by TSBF, and a quite large radiative rate constant of TSBF. In addition, the TSBF-based OLEDs with quite small active areas showed the similar efficiency roll-off to previously reported nano-patterned and single-layer OLEDs with BSB-Cz under high current densities of around 500 A cm^{-2}. However, the efficiency roll-off still remains although STA and SHQ are almost perfectly suppressed in TSBF. On the other hands, the detailed mechanisms and contributions of SPA and electric field-induced quenching are unclear under high current densities. For further suppression of efficiency roll-off, SPA and electric field-induced quenching should be investigated in detail. In the future, fluorene-based materials are promising and should be investigated because the fluorene-based materials tend to show large k_r induced by their large oscillator strength [3,4].

The author hopes that these findings will be useful for the suppression of EL efficiency roll-off characteristics in future high-brightness OLEDs and OSLDs.

Future perspective

In TADF emitters, the material design to enhance k_{RISC} is crucial for realizing the suppression of exciton annihilation and efficiency roll-off. For obtaining a large k_{RISC}, the author suggests two ideas. The first idea is the thermally induced enhancement of a RISC process. Here, the detailed mechanism of a RISC process is shown in Fig. 5-1. Since only thermally activated-triplet excitons having same energy to S_1 can convert to the singlet excitons through the RISC process, k_{RISC} is represented by an Arrhenius equation considering Boltzmann distribution while k_{ISC} is independent on the temperature in case of the ISC from S_1 to T_1 (However, the ISC from S_1 to a higher lying triplet excited state is based on an Arrhenius equation) [5,6]. Therefore, a temperature increase induced by Joule-heating in the device or an externally heating from the outside of the device would enhance k_{RISC} under high current densities [7] while $k_{\mathrm{nr}}^{\mathrm{T}}$ and k_{TTA} are also enhanced by temperature increase [7,8], indicating that the temperature increase shows the trade-off effect for efficiency roll-off. However, in a TADF assisted delayed fluorescence (TAF) system which employs a TADF molecule as an assistant dopant for a triplet harvester and a fluorescence molecule as an end emitter [9,10], the deactivation processes from the triplet excited state such as the nonradiative decay and the TTA would be suppressed under high temperature because the once upconverted triplet energy from T_1 to S_1 is immediately transferred to the end emitter before the re-conversion from S_1 to T_1 through ISC. Here, the author notes that if the fluorescence molecule as an end emitter has a large k_{r}, the PLQY decrease will be suppressed under high temperature. Therefore, the effect of temperature increase in TAF system with a large k_{r} should be investigated in the future.

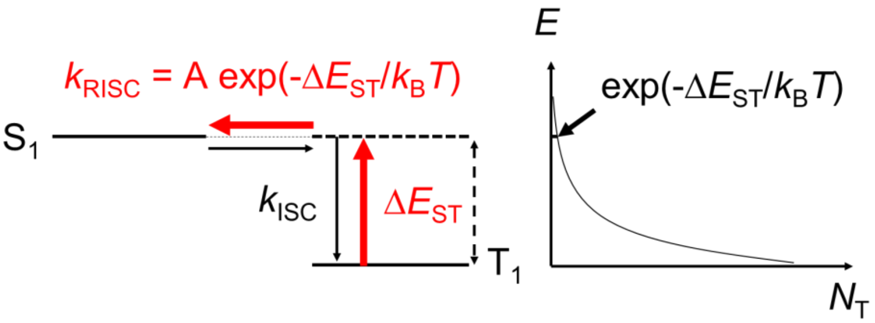

Figure 5-1. The detailed mechanism of RISC process. The equation of the Arrhenius equation shows the RISC rate. *A* is related with the spin orbital coupling. k_B and *T* are Boltzmann constant and temperature.

The other is the molecular designs for a small ΔE_{ST} and a large spin conversion efficiency. Figure 5-2 shows the relationship between k_{RISC} and ΔE_{ST} of the TADF emitters previously reported [11-22]. k_{RISC} tends to be increased with a decrease of ΔE_{ST}, indicating that smaller ΔE_{ST} enhances the RISC processes. However, the red solid curves obtained from the Arrhenius equation predict saturation of k_{RISC} at small ΔE_{ST}, indicating that ΔE_{ST} of about 0.01 eV is enough to obtain the maximum k_{RISC}. The reported k_{RISC} and ΔE_{ST} are strongly dependent upon TADF materials and are present in the two red curves calculated with $A = 10^5$ and 10^8 in the Arrhenius equation shown in Fig. 5-2. *A* is related with the spin orbital coupling. This suggests that obtaining large *A* is important as well as obtaining small ΔE_{ST} to increase k_{RISC}. To reduce STA and TTA-induced efficiency roll-off, triplet exciton density must be reduced to a level comparable to singlet exciton density in TADF-OLEDs by increasing k_{RISC} to a level at least comparable to k_r (e.g. 10^8 s^{-1}). To obtain $k_{RISC} = 10^8$ s^{-1}, TADF materials with $A = 10^8$ are required [see Fig. 5-2]. The key to increase *A* is to enhance spin conversion efficiency of TADF materials. Therefore, the author suggests that the incorporation of a heavy atom in TADF molecules is a possible way to enhance spin conversion efficiency because the heavy atom enhances the spin-orbital coupling [23]. For example, Ir(ppy)$_3$ shows large intersystem crossing rate constant from S$_1$ to T$_1$ (k_{ISC} ~ 10^{12} s^{-1}) and radiative emission rate constant from T$_1$ (k_r^{T} ~ 10^6 s^{-1}) due to the enhanced spin-orbital coupling [24]. The k_{ISC} value exceeds the k_r^{T} by more than six orders of magnitude. If TADF materials incorporated with Ir are obtained, quite high k_{RISC} will be achieved as well as k_{ISC} due to the energy alignment of singlet and triplet excited levels. Additionally, small ΔE_{ST} generally forces to reduce k_r and PLQY because of the weak interaction between HOMO and LUMO. Therefore, a reduction of ΔE_{ST} with maintaining large k_r (larger oscillator strength) is required through careful quantum chemical calculation before synthesizing TADF molecules.

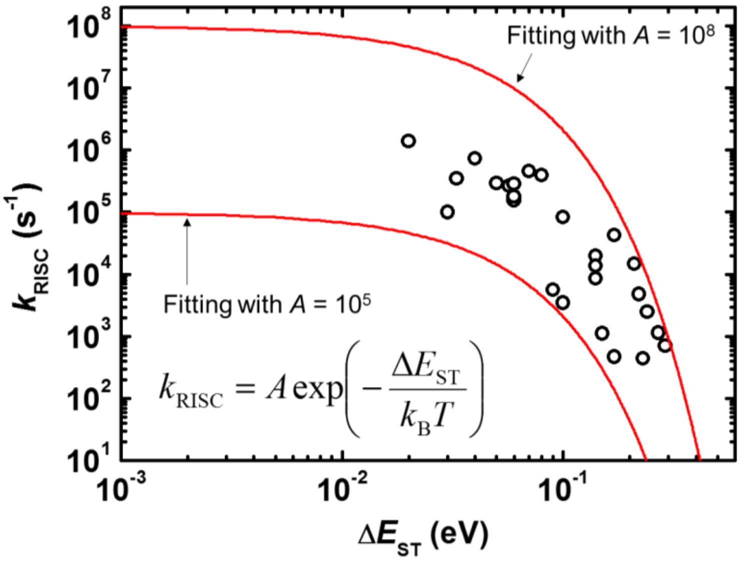

Figure 5-2. Relationship between k_{RISC} and ΔE_{ST} of the TADF emitters. The k_{RISC} and ΔE_{ST} values were picked up from refs [11-22]. The red solid curves are fitting results with the Arrhenius equation as shown in the inset. A is related with the spin orbital coupling.

The TADF process might be expected to be useful for the realization of OSLDs because not only singlet excitons but also triplet excitons can be harvested for light emission with suppressed STA and TTA. However, k_r is usually small for TADF molecules as the author explained earlier, preventing lasing from TADF molecules. A previous report shows a possibility of electrically pumped lasing from OLEDs with a TAF system which employs a TADF molecule as an assistant dopant for triplet harvester and a laser dye as an end emitter [9,10]. ASE was observed from this TAF system under optical pumping although the contribution of harvested energy from triplet excitons is small under a short pulse (800 ps) excitation condition used in the reference [9] because the up-conversion from T_1 to S_1 is still unfinished in comparison with emission from laser dyes. If k_{RISC} over 10^8 s^{-1} is obtained, the singlet excitons upconverted from triplet excitons can contribute to ASE or lasing. Furthermore, k_{r} of laser dyes as an end emitter is also important to obtain small efficiency roll-off and low ASE threshold. Therefore, the TAF system using high k_{RISC} of TADF molecules and high k_{r} of end emitters is strongly required to reduce ASE and lasing thresholds under electrical excitation and obtain quite high η_{EQE} at high current density because STA, TTA, SHQ, and electric-field induced quenching are suppressed based on the results presented in this thesis.

However, other challenges still must need to finally realize OSLDs. ASE threshold measured in device structures is always higher than that measured in films under optical pumping because of a strong propagation loss originating from metal electrodes. Therefore, it need to find other electrodes or other device structures that minimize the propagation loss. The author demonstrated the relaxation of the increase of the ASE threshold in OLEDs structure by inserting an exciton blocking layer between an active layer and metal cathode layer. The results are shown in Appendix B. Moreover, small-active-area devices with μm-order diameters are usually used to inject high current densities because the small active area can reduce Joule heating inducing device breakdown. However, the small active area also leads to an increase of ASE threshold because of a small gain in the waveguide. To prevent the increased ASE threshold following the reduced active area, incorporation of a distributed feedback structure into organic devices is also promising. A well-known mixed order DFB structure, which makes it possible to obtain quite low ASE threshold (for example, 0.032 μJ cm^{-2} in ref. [25]), is the most effective among DFB structures. By combining the above techniques, the author expects that OSLDs can be realized in the future.

References

[1] C. Ouannes, T. Wilson, J. Am. Chem. Soc. **90** (1968) 6527.

[2] E. Baciocchi, T. D. Giacco, F. Elisei, M. F. Gerini, M. Guerra, A. Lapi, P. Liberali, J. Am. Chem. Soc. **125** (2003) 16444.

[3] T. Oyamada, C. H. Chang, T. C. Chao, F. C. Fang, C. C. Wu, K. T. Wong, H. Sasabe, C. Adachi, J. Phys. Chem. C **111** (2007) 108.

[4] E. Y. Choi, L. Mazur, L. Mager, M. Gwon, D. Pitrat, J. C. Mulatier, C. Monnereau, A. Fort, A. J. Attias, K. Dorkenoo, J. E. Kwon, Y. Xiao, K. Matczyszyn, M. Samoc, D.-W. Kim, A. Nakao, B. Heinrich, D. Hashizume, M. Uchiyama, S. Y. Park, F. Mathevet, T. Aoyama, C. Andraud, J. W. Wu, A. Barsell, J. C. Ribierre, Phys. Chem. Chem. Phys. **16** (2014) 16941.

[5] J. B. Birks, "Photophysics of Aromatic Molecules", John Wiley (1970) 143ff.

[6] L. Song, M. D. Fayer, Journal of Luminescence **50** (1991) 75.

[7] A. Endo, M. Ogasawara, A. Takahashi, D. Yokoyama, Y. Kato, C. Adachi, Adv. Mater. **21** (2009) 4802.

[8] X. Liu, Y. Zhang, S. R. Forrest, Phys. Rev. B **90** (2014) 085201.

[9] H. Nakanotani, T. Furukawa, C. Adachi, Adv. Opt. Mater. **3** (2015) 1381.

[10] T. Furukawa, H. Nakanotani, M. Inoue, C. Adachi, Sci. Rep. **5** (2015) 8429.

[11] S. Y. Lee, T. Yasuda, H. Nomura, C. Adachi, Appl. Phys. Lett. **101** (2012) 093306.

[12] G. Mehes, H. Nomura, Q. Zhang, T. Nakagawa, C. Adachi, Angew. Chem. Int. Ed. **51** (2012) 11311.

[13] T. Nakagawa, S. Y. Ku, K. T. Wong, C. Adachi, Chem. Comm. **48** (2012) 9580.

[14] H. Tanaka, K. Shizu, H. Miyazaki, C. Adachi, Chem. Comm. **48** (2012) 11392.

[15] J. Y. Kim, T. Yasuda, Y. S. Yang, C. Adachi, Adv. Mater. **25** (2013) 3319.

[16] K. Nasu, T. Nakagawa, H. Nomura, C. J. Lin, C. H. Cheng, M. R. Tseng, T. Yasuda, C. Adachi, Chem. Comm. **49** (2013) 10385.

[17] J. Lee, K. Shizu, H. Tanaka, H. Nomura, T. Yasuda, C. Adachi, J. Mater. Chem. C **1** (2013) 4599.

[18] K. Masui, H. Nakanotani, C. Adachi, Org. Electron. **14** (2013) 2721.

[19] K. Sato, K. Shizu, K. Yoshimura, A. Kawada, H. Miyazaki, C. Adachi, Phys. Rev. Lett. **110** (2013) 247401.

[20] S. Y. Lee, T. Yasuda, Y. S. Yang, Q. Zhang, C. Adachi, Angew. Chem. **126** (2014) 6520.

[21] B. Li, H. Nomura, H. Miyazaki, Q. Zhang, K. Yoshida, Y. Suzuna, A. Orita, J. Otera, C. Adachi, Chem. Lett. **3** (2014) 319.

[22] Q. Zhang, H. Kuwabara, W. J. Potscavage Jr, S. Huang, Y. Hatae, T. Shibata, C. Adachi, J. Am. Chem. Soc. **136** (2014) 18070.

[23] N. J. Turro, K. C. Liu, M. F. Chow, P. Lee, J. Am. Chem. Soc. **95** (1973) 6709.

[24] M. Kleinschmidt, C. van Wüllen, C. M. Marian, J. Chem. Phys. **142** (2015) 094301.

[25] C. Karnutsch, C. Pflumm, G. Heliotis, J. C. deMello, D. D. C. Bradley, J. Wang, T. Weimann, V. Haug, C. Gärtner, U. Lemmer, Appl. Phys. Lett. **90** (2007) 131104.

Appendix B

Realization of lower amplified spontaneous emission threshold and smaller electroluminescence efficiency roll-off in an organic semiconductor laser structure

Munetomo Inoue, Kenichi Goushi, Kuniaki Endo, Hiroko Nomura, and Chihaya Adachi

Journal of Luminescence, **143** (2013) 153302.

Abstract

The author demonstrated that lower ASE threshold and smaller EL efficiency roll-off were realized at the same time in an OSLD structure by inserting a phenyl-dipyrenylphosphine oxide ($POPy_2$) layer between a BSB-Cz active layer and metal cathode layer. The insertion of $POPy_2$ caused unfavorable BSB-Cz-to-metal energy transfer to significantly reduce, minimizing an increase of ASE threshold caused by the metal. Additionally, since the electron injection barrier is downward and hole injection barrier is very small at the BSB-Cz/$POPy_2$ heterointerface, extra carriers does not accumulate at this heterointerface. Therefore, SPA caused by accumulated carriers was not pronounced in the device structure with $POPy_2$, resulting in smaller efficiency roll-off.

Introduction

OSLDs have a great potential as novel light sources for information and communication device applications because of their emission wavelength tunability, large bandwidth, compact size, and high speed sensing capability [1-6]. However, to realize lasing by electrical pumping using organic semiconductors, EL efficiency roll-off caused by exciton quenching processes under high current densities must be suppressed. In a recent paper, Y. Setoguchi and C. Adachi reported that OLEDs consisting of a single EML of BSB-Cz which was locally doped with strong donors and acceptors near a metal cathode and ITO anode show improved efficiency roll-off characteristics under high current densities of over 100 A cm^{-2} [7] because no inclusion of organic-organic heterointerfaces in this device can avoid extra carrier accumulation which is expected to be one of the sources of SPA [8]. However, the ASE threshold estimated in this single-layer OLED structure under optical pumping was significantly increased to E_{th} = 24 μJ cm^{-2} compared with E_{th} = 0.6 μJ cm^{-2} measured from a neat BSB-Cz film vacuum-deposited on a glass substrate [9]. The increased E_{th} is because of energy transfer from BSB-Cz to the metal [10-12]. It has been demonstrated that the ASE threshold increased by the metal cathode can be relaxed by inserting an organic ETL or EBL between the EML and metal cathode layer [13], while the roll-off characteristics observed under high-current operation became significant because of significant carrier accumulation at the heterointerface. Therefore, the development of new OLED structures with both lower ASE threshold and smaller efficiency roll-off at high current densities is strongly required. In this study, the author demonstrated that lower ASE threshold and smaller efficiency roll-off are realized at the same time by inserting a $POPy_2$ layer between the BSB-Cz and metal cathode layers. Since $POPy_2$ works as a spacer to prevent energy transfer from BSB-Cz to the metal layer, the increase of the ASE threshold was relaxed. Additionally, since the insertion of $POPy_2$ does not cause carrier accumulation in terms of better energy level alignment, the smaller efficiency roll-off was observed in the device with $POPY_2$.

Experimental

The organic and metal films used in the ASE measurements were deposited by conventional thermal evaporation under a high vacuum condition (ca. 7×10^{-4} Pa) on 30-nm ITO-coated glass substrates. These films were optically pumped from the ITO side using focused excitation light with a radiation area of 0.06 × 2 cm from a nitrogen gas laser (USHO, KEN-2020) with an excitation wavelength of 337 nm, pulse width of ~800 ps, and repetition rate of 20 Hz. A detector (Hamamatsu Photonics, PMA-11) to observe the PL spectra was located on the edge of the films. The propagation loss characteristics were also measured by gradually separating the excitation position from the edge of an optical waveguide [14]. All measurements were conducted under a nitrogen atmosphere to prevent degradation of the films by moisture and oxygen.

The OLEDs were fabricated by thermal evaporation under a high vacuum (ca. 7×10^{-4} Pa) on 30-nm ITO-coated sapphire substrates. The sapphire substrates were used because they have a higher thermal conductivity and achieve high current densities [15]. A cathode layer was deposited through a shadow mask with 200 μm-diameter openings. The *J-V-L* characteristics under DC driving were obtained by using a semiconductor parameter analyzer (Agilent, E5273A) and optical power meter (Newport, 1930C). The *J-V-L* characteristics under pulse driving were measured using a pulse generator (Agilent, B114A) and the optical power meter. For measurement of the *J-V-L* characteristics under pulse driving, short pulse excitation with a repetition rate of 100 Hz was used.

Results and discussions

Figure A-1 shows the emission intensity-excitation intensity characteristics in the stacked organic films that include a neat BSB-Cz film as an active layer. In a 270 nm thick BSB-Cz film deposited on the ITO (30 nm) coated glass substrate, an ASE threshold of E_{th} = 1.3 μJ cm^{-2} was obtained (Film A). On the other hand, by depositing an 80 nm thick Ag layer on Film A, E_{th} increased up to 19 μJ cm^{-2} (Film B). The increased E_{th} level can be ascribed to exciton quenching resulting from energy transfer from BSB-Cz to Ag [10-12]. The E_{th} in Film C, which is composed of a 5 wt% MoO_3-doped BSB-Cz layer (10 nm) between the neat BSB-Cz layer and the ITO anode in Film B, was similar to that of Film B. However, by inserting a 70 nm $POPy_2$ layer between the BSB-Cz layer and the Ag cathode, E_{th} was significantly reduced to 3.5 μJ cm^{-2} (Film D). In addition, the E_{th} in Film E, produced by inserting a 5 wt% MoO_3-doped BSB-Cz layer (10 nm) and a 10 wt% Cs-doped $POPy_2$ (10 nm) layer to act as a p-doping layer and an n-doping layer, respectively, was also significantly reduced compared with that of Film B.

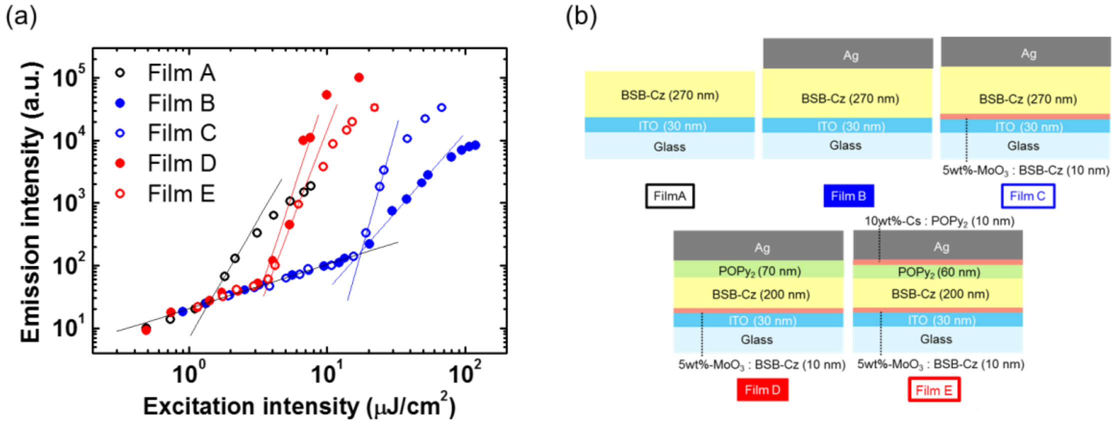

Figure A-1. (a) ASE characteristics of the stacked organic films including a neat BSB-Cz film as the ASE active layer and (b) stacked organic film structures studied here.

The author investigated the mechanism of the ASE threshold reduction by insertion of a POPy2 layer. The E_{th} is given by [16]

$$E_{\mathrm{th}} = \frac{dh\nu\alpha}{\Gamma\phi_{\mathrm{PL}}\sigma_{\mathrm{all}}}, \qquad \text{(A5-1)}$$

where α is the propagation loss, Γ is the confinement factor, d is the excitation zone produced by photo-excitation, h is Planck's constant, v is the frequency of the ASE, Φ_{PL} is the PLQY, and σ_{all} is the summation of the cross-sections, including the stimulated emission cross-section, self-absorption cross-section, SSA cross-section, SPA cross-section, and STA cross-section [16-21]. Here, the ratio of the ASE thresholds of the different films is given by

$$\frac{E_{\mathrm{th,E}}}{E_{\mathrm{th,C}}} = \frac{\alpha_{\mathrm{E}}\Gamma_{\mathrm{C}}\phi_{\mathrm{PL,C}}\sigma_{\mathrm{all,C}}}{\alpha_{\mathrm{C}}\Gamma_{\mathrm{E}}\phi_{\mathrm{PL,E}}\sigma_{\mathrm{all,E}}}. \qquad \text{(A5-2)}$$

The subscript letter of each value represents the particular film structure. Figure A-2(a) shows the excitation position dependence of the 0-1 peak emission intensities in Films C and E, which were obtained from the edge emission spectra. From these results, the author estimated values of $\alpha_{\mathrm{C}} = 6.5\ \mathrm{cm}^{-1}$ and $\alpha_{\mathrm{E}} = 5.0\ \mathrm{cm}^{-1}$ at the ASE wavelength [14]. In addition, the Γ_{C} and Γ_{E} values were evaluated by the transfer matrix method [22]. The evaluation is shown in Fig. A-3. As a result, the author obtained values of $\Gamma_{\mathrm{C}} = 0.89$ and $\Gamma_{\mathrm{E}} = 0.79$. Therefore, the $\Phi_{\mathrm{PL,E}} \times \sigma_{\mathrm{all,E}}$ product is estimated to be approximately 4.0 times higher than the $\Phi_{\mathrm{PL,C}} \times \sigma_{\mathrm{all,C}}$ product.

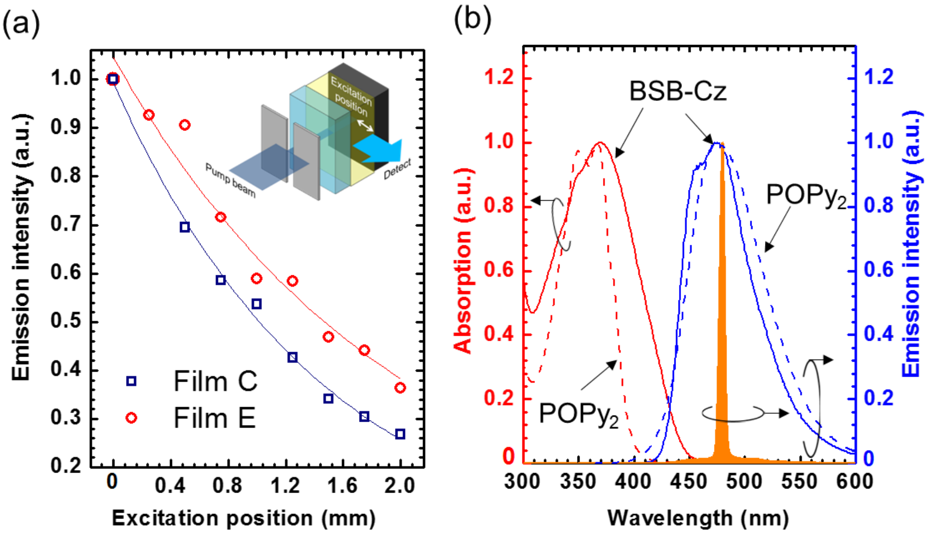

Figure A-2. (a) Edge emission characteristics of Film C and Film E below the ASE threshold. Inset: Measurement of the edge emission spectra depending on excitation position. (b) UV-visible absorption fluorescence and ASE spectra of the neat BSB-Cz film, and the UV-visible absorption and fluorescence spectra of the neat POPy$_2$ film.

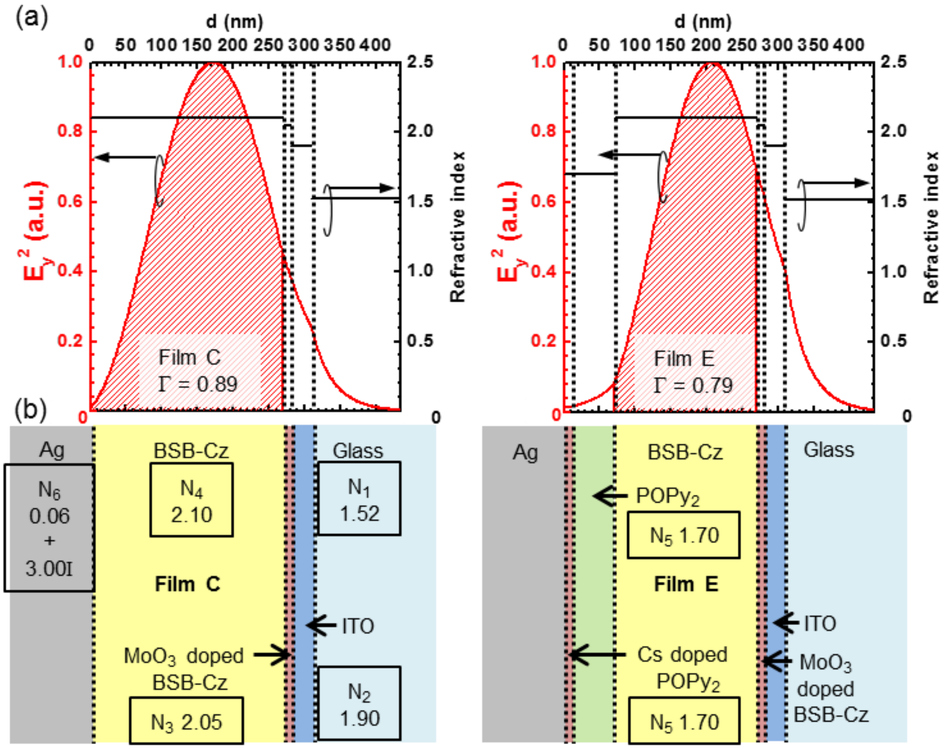

Figure A-3. (a) Electric field distributions in Film C and Film E. (b) Structures of Film C and Film E, showing the refractive indexes for each layer.

The value of $\sigma_{\mathrm{all,E}}$ should be similar to $\sigma_{\mathrm{all,C}}$, because σ_{all} is determined by the emitter material. The author therefore concludes that Φ_{PL} is enhanced by insertion of the POPy$_2$ layer. Here, the author discusses Φ_{PL} in these structures, which is affected by the self-absorption properties of BSB-Cz during light propagation. Figure A-2(b) shows the UV-visible absorption, fluorescence and ASE spectra of the BSB-Cz layers. There is a weak overlap between the fluorescence and absorption spectra around the 0-0 transition, which indicates that excitons can be transferred through self-absorption, i.e., the Förster mechanism. After photo-excitation, excitons are mainly generated near the ITO side with an exponential distribution from the edge and 90% of the excitation light is absorbed within a depth of 130 nm. A number of the generated excitons are, however, transferred to the other BSB-Cz molecules located near the Ag electrode through the self-absorption process between the 0-0 transitions during emitted light propagation [23,24], leading to a lower $\Phi_{\mathrm{PL,C}}$ because of radiationless deactivation by energy transfer to the metal electrode. In contrast, by inserting a POPy$_2$ layer at the interface between the BSB-Cz layer and Ag cathode, excitons are confined inside the BSB-Cz layer without energy transfer into the metal electrode because of the presence of the wider band gap of the POPy$_2$ layer rather than that of the BSB-Cz layer [11,25]. Indeed, the energy transfer from the BSB-Cz layer to the POPy$_2$ layer can be suppressed because of the significantly small overlap between the emission spectrum of the BSB-Cz film and the absorption spectrum of the POPy$_2$ film [Fig. A-2(b)]. As a result, exciton confinement is achieved, leading to the higher $\Phi_{\mathrm{PL,E}}$ value and the reduced E_{th} value.

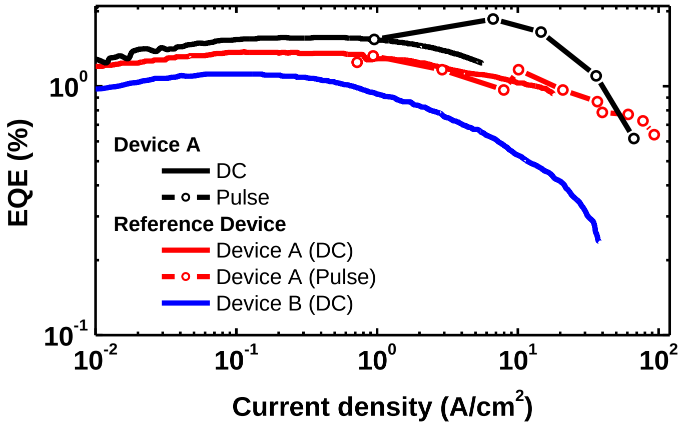

Figure A-4. η_{EQE}-J characteristics of Device A, Reference Device A, and Reference Device B under DC and pulsed operation.

Figure A-4 shows the η_{EQE}-J characteristics of the OLED structure (Device A), consisting of a sapphire substrate / ITO (30 nm) / 5 wt% MoO_3-doped BSB-Cz (10 nm) / BSB-Cz (200 nm) / $POPy_2$ (60 nm) / 10 wt% Cs-doped $POPy_2$ (10 nm) / Ag, which demonstrated a lower ASE threshold (E_{th} = 4.0 μJ cm^{-2}), as shown in Fig. A-1(a), compared with E_{th} = 24 μJ cm^{-2} for the previously reported non-heterostructure device (Reference Device A: sapphire substrate / ITO (30 nm) / 5 wt% MoO_3-doped BSB-Cz (10 nm) / BSB-Cz (200 nm) / 10 wt% Cs-doped $POPy_2$ (70 nm) / Ag) [7]. While the Cs-doped BSB-Cz layer in Reference Device A quenches the BSB-Cz's excitons significantly, the $POPy_2$ layer in Device A confines excitons well, resulting in the lower ASE threshold. Device A also exhibited relaxation of the roll-off characteristics under higher current densities compared with those of the previously reported double-heterostructure device (Reference Device B: sapphire substrate / ITO (30 nm) / MoO_3 (30 nm) / mCP (10 nm) / BSB-Cz (20 nm) / BCP (10 nm) / 20 wt% Cs-doped $POPy_2$ (30 nm) / Al, where BCP is 2,9-dimethyl-4,7-diphenyl-1,10-phenanthroline) [7] and comparable roll-off characteristics to those of Reference Device A. The energy level diagrams of Device A, Reference Device A and Reference Device B are shown in Fig. A-5.

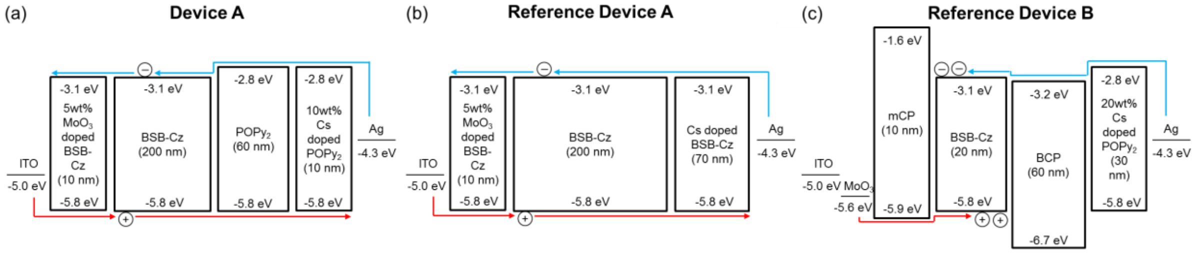

Figure A-5. Energy level diagrams for (a) Device A, (b) Reference Device A, and (c) Reference Device B.

In Reference Device B, carrier accumulation at the heterointerfaces between the BSB-Cz and BCP layers occurred because of the large carrier injection barrier of 0.9 eV at HOMO levels between them. Therefore, the roll-off characteristics would be caused by SPA, as shown in Fig. A-3. On the other hand, in Device A, hole accumulation at the interface between the BSB-Cz and $POPy_2$ layers can be suppressed well because of the no hole injection barrier at the HOMO levels between them. The author can also expect virtually no electron injection barriers between the layers because of the alignment of their LUMO levels. Therefore, the roll-off characteristics caused by SPA can be relaxed, similar to the case of Reference Device A. Here, the author notes that having almost the same η_{EQE} values in Device A and Reference Device A ensures that most of the carrier recombination occurs inside the BSB-Cz layers in both devices.

Summary

The author has demonstrated the lowering of the ASE threshold in OLEDs with low roll-off characteristics under high current densities by the introduction of a $POPy_2$ layer as an ETL/EBL. The ASE threshold was reduced by exciton confinement in the EML. The electrically pumped device also showed relaxation of the roll-off characteristics under high current densities by avoiding carrier accumulation. To realize lasing by electrical excitation, however, further reduction of the threshold by two orders of magnitude and suppression of the roll-off characteristics caused by STA and SHQ must also be overcome.

References

[1] J. H. Burroughes, D. D. C. Bradley, A. R. Brown, R. N. Marks, K. Mackay, R. H. Friend, P. L. Burns, A. B. Holmes, Nature **347** (1990) 539.

[2] W. Holzer, A. Penzkofer, S.-H. Gong, A. Bleyer, D. D. C. Bradley, Adv. Mater. **8** (1996) 974.

[3] N. Tessler, G. J. Denton, R. H. Friend, Nature **382** (1996) 695.

[4] F. Hide, M. A. Diaz-Garcia, B. J. Schwartz, M. R. Andersson, Q. Pei, A. J. Heeger, Science **273** (1996) 1833.

[5] R. H. Friend, R. W. Gymer, A. B. Holmes, J. H. Burroughes, R. N. Marks, C. Taliani, D. D. C. Bradley, D. A. D. Santos, J. L. Bredas, M. Logdlund, W. R. Salaneck, Nature **397** (1999) 121.

[6] M. D. McGehee, A. J. Heeger, Adv. Mater. **12** (2000) 1655.

[7] Y. Setoguchi, C. Adachi, J. Appl. Phys. **108** (2010) 064516.

[8] N. C. Giebink, B. W. D’Andrade, M. S. Weaver, P. B. Mackenzie, J. J. Brown, M. E. Thompson, S. R. Forrest, J. Appl. Phys. **103** (2008) 044509.

[9] D. Yokoyama, M. Moriwake, C. Adachi, J. Appl. Phys. **103** (2008) 123104.

[10] M. Stoessel, G. Wittmann, J. Staudigel, F. Steuber, J. Blässing, W. Roth, H. Klausmann, W. Rogler, J. Simmerer, A. Winnacker, M. Inbasekaran, E. P. Woo, J. Appl. Phys. **87** (2000) 4467.

[11] A. L. Burin, M. A. Ratner, J. Phys. Chem. A **104** (2000) 4704.

[12] H. Yamamoto, T. Oyamada, H. Sasabe, C. Adachi, Appl. Phys. Lett. **84** (2004) 1401.

[13] V. G. Kozlov, V. Bulović, P. E. Burrows, S. R. Forrest, Nature **389** (1997) 362.

[14] T. Rabe, P. Görrn, M. Lehnhardt, M. Tilgner, T. Riedl, W. Kowalsky, Phys. Rev. Lett. **102** (2009) 137401.

[15] H. Nakanotani, H. Sasabe, C. Adachi, Appl. Phys. Lett. **86** (2005) 213506.

[16] T. Komino, H. Nomura, M. Yahiro, K. Endo, C. Adachi, J. Phys. Chem. C **115** (2011) 19890.

[17] D. E. Mccvmber, Phys. Rev. **136** (1964) 954.

[18] S. Singh, R. G. Smith, L. G. Van Uitertt, Phys. Rev. B **10** (1974) 2566.

[19] J. Koetke, G. Huber, Appl. Phys. B **61** (1995) 151.

[20] R. Rolli, M. Montagna, S. Chaussedent, A. Monteil, V. K. Tikhomirov, M. Ferrari, Opt. Mat. **21** (2003) 743.

[21] Y. Zhang, S. R. Forrest, Phys. Rev. B **84** (2011) 241301.

[22] T. Fuhrmann, K. Samse, J. Salbeck, A. Perschke, H. Franke, Org. Electron. **4** (2003) 219.

[23] L. A. Cury, P. S. Guimarães, J. Appl. Phys. **100** (2006) 093105.

[24] J. Baumann, G. Calzaferri, T. Hugentobler, Chem. Phys. Lett. **116** (1985) 66.

[25] M. Ikai, S. Tokito, Y. Sakamoto, T. Suzuki, Y. Taga, Appl. Phys. Lett. **79** (2001) 156.

Abbreviation list

Keywords

Amplified spontaneous emission (ASE)

Cold isostatic pressing (CIP)

Distributed-feedback (DFB)

Direct current (DC)

Electroluminescence (EL)

Electron-blocking layer (EBL)

Electron-transport layer (ETL)

Emitting layer (EML)

External quantum efficiency (EQE)

Full width at half maximum (FWHM)

Highest occupied molecular orbital (HOMO)

Hole-blocking layer (HBL)

Hole-transport layer (HTL)

Intersystem crossing (ISC)

Internal quantum efficiency (IQE)

Lowest singlet excited state (S_1)

Lowest triplet excited state (T_1)

Lowest unoccupied molecular orbital (LUMO)

Organic light-emitting diodes (OLEDs)

Organic semiconductor laser diodes (OSLDs)

Photoluminescence (PL)

Photoluminescence quantum yields (PLQYs)

Reverse intersystem crossing (RISC)

Singlet ground state (S_0)

Singlet-heat annihilation (SHQ)

Singlet-polaron annihilation (SPA)

Singlet-singlet annihilation (SSA)

Singlet-triplet annihilation (STA)

Thermally activated delayed fluorescence (TADF)

Thermally activated delayed fluorescence assisted fluorescence (TAF)

Triplet-polaron annihilation (TPA)

Triplet-triplet annihilation (TTA)

Materials

3-(9,9-Dimethylacridin-10(9H)-yl)-9H-xanthen-9-one (ACRXTN)

9,10-Di(naphth-2-yl)anthracene (ADN)

Tris(8-hydroxyquinolinato)aluminum (Alq_3)

4,4’-Bis[*N*-(1-naphthyl)-*N*-phenyl-amino]biphenyl (α-NPD)

2,9-Dimethyl-4,7-diphenyl- 1,10-phenanthroline) (BCP)

4,4’-Bis[4-(diphenylamino)styryl]biphenyl (BDAVBi)

4,4’-Bis[(*N*-carbazole)styryl]biphenyl (BSB-Cz)

4,4’-Bis(carbazol-9-yl)biphenyl (CBP)

Cyclooctatetraene (COT)

2,3,6,7-Tetrahydro-1,1,7,7,-tetramethyl-1*H*,5*H*,11*H*-10-(2-benzothiazolyl)quinolizino[9,9a,1gh]coumarin (C545T)

(*E*)-2-(2-(4-(dimethylamino)styryl)- 6-methyl-4*H*-pyran-4-ylidene)malononitrile (DCM)

4-(Dicyanomethylene)-2-methyl- 6-julolidyl-9-enyl-4*H*-pyran (DCM2)

4-(Dicyanomethylene)-2-tert-butyl-6-(1,1,7,7-tetramethyljulolidin-4-yl-vinyl)-4H-pyran (DCJTB)

Tris(2-phenylpyridinato)iridium(III) [$Ir(ppy)_3$]

Indium tin oxide (ITO)

N,*N*’-dicarbazolyl-3,5-benzene (mCP)

Phenyl-dipyrenylphosphine oxide ($POPy_2$)

2,8-Bis(di- phenylphosphoryl)dibenzo-[b,d]thiophene (PPT)

2,7-Bis[4-(*N*-carbazole)phenylvinyl]-9,9’-spirobifluorene (spiro-SBCz)

Ter(9,9’-spirobifluorene) (TSBF)

2,2’,2”-(1,3,5-Benzinetriyl)-tris[1-phenyl-1-*H*-benzimidazole] (TPBi)

1,2-Bis(carbazol-9-yl)-4,5-dicyanobenzene (2CzPN)

Physical symbols

Absorption cross-section (σ_a)

ASE threshold energies (E_{th})

Avogadro constant (N_A)

Component of EQE decreased by STA (α_{STA})

Constant factor (C')

Confinement factor (Γ)

Current density (J)

Current density where η_{EQE} decreases to 60% of the initial η_{EQE} (J_{60})

Density of polaron exciton (N_P)

Density of singlet exciton (N_S)

Density of triplet exciton (N_T)

Elementary charge (e)

Emission spectrum shape function ($f_D(\nu)$)

Energy gap between a lowest singlet excited state and a lowest triplet excited state (ΔE_{ST})

External quantum efficiency (η_{EQE})

Förster radius (r_0)

Half of an initial external quantum efficiency (J_0)

HOMO–HOMO difference between each laser dye and CBP (ΔE_{HOMO})

Initial photoluminescence intensity (I_{PL_0})

Internal quantum efficiency (η_{IQE})

Light out-coupling efficiency of OLEDs (η_{out})

Maximum external quantum efficiency ($\eta_{EQE,\ max}$)

Molar absorption coefficient of triplet excitons (for STA) or polarons (for SPA) ($\varepsilon_A(\nu)$)

Photoluminescence intensity at 40 μs (I_{PL})

Photoluminescence lifetime (τ)

Photoluminescence lifetime of delayed component ($\tau_{delayed}$)

Photoluminescence lifetime of prompt component (τ_{prompt})

Photoluminescence peak wavelength (λ_{max})

Photoluminescence quantum yield (Φ_{PL})

Photoluminescence quantum yield of delayed component (Φ_{delayed})

Photoluminescence quantum yield of prompt component (Φ_{prompt})

Planck constant (h)

Proportion of EQE decreased by other quenching mechanisms (α_{others})

Quenching radius of Dexter transfer (r)

Rate constant of intersystem crossing from a lowest singlet excited state to a lowest triplet excited state (k_{ISC})

Rate constant of non-radiative decay from a lowest singlet excited state to ground state (k_{nr})

Rate constant of non-radiative decay from a lowest triplet excited state to ground state ($k_{\mathrm{nr}}^{\mathrm{T}}$)

Rate constant of quenching by electric field and Joule heating (k_{q})

Rate constant of radiative emission from a lowest singlet excited state to a ground state (k_{r})

Rate constant of radiative emission from a lowest triplet excited state to a ground state ($k_{\mathrm{r}}^{\mathrm{T}}$)

Rate constant of reverse intersystem crossing from a lowest triplet excited state to a lowest singlet excited state (k_{RISC})

Rate constant of singlet-polaron annihilation (k_{SPA})

Rate constant of singlet-triplet annihilation (k_{STA})

Rate constant of triplet-polaron annihilation (k_{TPA})

Rate constant of triplet-triplet annihilation (k_{TTA})

Refractive index in a fluorescent region (n_{F})

Saturated triplet population (N_0)

Singlet exciton density estimated from ASE threshold under optical excitation ($N^{\mathrm{S}}{}_{\mathrm{th}}$)

Singlet exciton density under electrical excitation ($N^{\mathrm{S}}{}_{\mathrm{EL}}$)

Singlet exciton production ratio *via* triplet-triplet annihilation (α)

Speed of the light (c)

Summation of cross-sections (σ_{all})

Thickness of film (d)

Wavelength (λ)

Wavelengths of ASE (λ_{ASE})

Width of waveguide (L)

Voltage (V)

Chapter 5

Publication list

Original papers

1) Munetomo Inoue, Kenichi Goushi, Kuniaki Endo, Hiroko Nomura, Chihaya Adachi, **Journal of Luminescence**, **143** (2013) 754-758.
“Reduced amplified spontaneous emission threshold in organic semiconductor laser structure with relaxed roll-off characteristics under high current densities”
doi:10.1016/j.jlumin.2013.04.001

2) Munetomo Inoue, Toshinori Matsushima, Hajime Nakanotani, Chihaya Adachi, **Chemical Physics Letters**, **624** (2015) 43-46.
“Introduction of Oxygen into Organic Thin Films with the Aim of Suppressing Singlet-Triplet Annihilation”
doi:10.1016/j.cplett.2015.02.010

3) Munetomo Inoue, Tomas Serevičius, Hajime Nakanotani, Kou Yoshida, Toshinori Matsushima, Saulius Juršėnas, Chihaya Adachi, **Chemical Physics Letters**, **644** (2016) 62-67.
“Effect of reverse intersystem crossing rate to suppress efficiency roll-off in organic light-emitting diodes with thermally activated delayed fluorescence emitters”
doi:10.1016/j.cplett.2015.11.042

4) Munetomo Inoue, Toshinori Matsushima, Chihaya Adachi, **Applied Physics Letters**

(submitted).

“Low amplified spontaneous emission threshold and suppression of electroluminescence efficiency roll-off in layers doped with ter(9,9’-spirobifluorene)”

Joint papers

1) Kyohei Hayashi, Hajime Nakanotani, Munetomo Inoue, Kou Yoshida, Oleksandr Mikhnenko, Thuc-Quyen Nguyen, Chihaya Adachi, **Applied Physics Letters**, **106** (2015) 093301. Selected as Most Read Articles on May (2015)
"Suppression of roll-off characteristics of organic light-emitting diodes by narrowing current injection/transport area to 50 nm"
doi:10.1063/1.4913461

2) Ju-Hyung Kim, Munetomo Inoue, Li Zhao, Takeshi Komino, Soonmin Seo, Jean-Charles Ribierre, Chihaya Adachi, **Applied Physics Letters**, **106** (2015) 053302.
"Tunable and flexible solvent-free liquid organic distributed feedback lasers"
doi:10.1063/1.4907323

3) Zhao Li, Takeshi Komino, Munetomo Inoue, J.-H. Kim, Jean-Charles Ribierre, Chihaya Adachi, **Applied Physics Letters**, **106** (2015) 063301.
"Horizontal molecular orientation in solution-processed organic light-emitting diodes"
doi:10.1063/1.4907890

4) Taro Furukawa, Hajime Nakanotani, Munetomo Inoue, Chihaya Adachi, **Scientific Reports 5** (2015) 8429.
"Dual enhancement of electroluminescence efficiency and operational stability by rapid upconversion of triplet excitons in OLEDs"
doi:10.1038/srep08429

5) Hiroyuki Kuwae, Atsushi Nitta, Kou Yoshida, Takashi Kasahara, Toshinori Matsushima, Munetomo Inoue, Shuichi Shoji, Jun Mizuno, Chihaya Adachi, **Journal of Applied Physics**, **118** (2015) 155501.
"Suppression of external quantum efficiency roll-off of nanopatterned organic-light emitting diodes at high current densities"
doi: 10.1063/1.4932139

6) Li Zhao, Munetomo Inoue, Kou Yoshida, Atula S. D. Sandanayaka, Ju-Hyung Kim, Jean-Charles Ribierre, Chihaya Adachi, **IEEE JOURNAL OF SELECTED TOPICS IN QUANTUM ELECTRONICS**, **22** (2016) 1.
"Singlet-Triplet Exciton Annihilation Nearly Suppressed in Organic Semiconductor Laser Materials Using Oxygen as a Triplet Quencher"
doi: 10.1109/JSTQE.2015.2473138

(7) Jean-Charles Ribierre, Li Zhao, Munetomo Inoue, Pierre-Olivier Schwartz, Ju-Hyung Kim, Kou Yoshida, Atula S. D. Sandanayaka, Hajime Nakanotani, Loic Mager, Stephane Mery, Chihaya Adachi, **Chemical Communications** (2016) in pless.
"Low threshold amplified spontaneous emission and ambipolar charge transport in non-volatile liquid fluorene derivatives"
doi: 10.1039/C5CC08331A

List of presentations at international conferences

1) Munetomo Inoue, Kenichi Goushi, Hayato Kakizoe, Hiroko Nomura, Chihaya Adachi

Materials Research Society, April 12, 2012, San Francisco, California.

"Suppression of propagation loss in organic semiconductor laser devices having low refractive index layers"

2) Munetomo Inoue, Kenichi Goushi, Kuniaki Endo, Hiroko Nomura, Chihaya Adachi

International Conference on Electroluminescence & Organic Optoelectronics, September 4, 2012, Fukuoka, Japan.

"Optimization of Organic Semiconductor Laser Structures aimed for low ASE threshold"

3) Munetomo Inoue, Kenichi Goushi, Kuniaki Endo, Hiroko Nomura, Chihaya Adachi

International Polymer Conference, December 12, 2012, Kobe, Japan.

"Organic semiconductor laser structure by using a phenyl-dipyrenylphosphine oxide layer as electron injection layer and an exciton blocking layer for the low roll-off characteristics at high current densities and low amplified spontaneous emission threshold"

4) Munetomo Inoue, Hajime Nakanotani, Chihaya Adachi

International Symposium on Novel Aromatic Compounds, August 1, 2013, Taipei, Taiwan.

"High mobility and blue-light-emitting ambipolar field-effect transistors based on an organic single crystal of di(phenylvinyl) anthracene"

5) Munetomo Inoue, Toshinori Matsushima, Hajime Nakanotani, Chihaya Adachi

Asian Conference on Organic Electronics, November 12, 2014, Tainan, Taiwan.

"Introduction of Oxygen into Organic Thin Films Aimed for Suppression of Singlet-Triplet Annihilation"

6) Munetomo Inoue, Tomas Serevičius, Hajime Nakanotani, Kou Yoshida, Toshinori Matsushima, Chihaya Adachi

International Chemical Congress of Pacific Basin Societies, December 17, 2015, Hawaii, USA.

"Study of intramolecular relaxation processes of thermally activated delayed fluorescence materials for suppressing external quantum efficiency roll-off in organic light-emitting diodes"

List of presentations at domestic conferences

1) 井上　棟智, 合志　憲一, 遠藤　晋旦, 野村　洸子, 安達　千波矢

有機 EL 討論会 第１６回例会, ６月２８日, ２０１３年, 東京

“有機半導体レーザーデバイスの実現に向けた ASE 発振閾値の低減及び高電流密度下における Roll-off 抑制の両立”

2) 井上　棟智, 中野谷　一, 安達　千波矢

第３回 CSJ 化学フェスタ２０１３, １０月２３日, ２０１３年, 東京

“2,9-di(phenylvinyl) anthracene を用いた高移動度青色発光トランジスタ”

3) 井上　棟智, 松島　敏則, 安達　千波矢

第６２回応用物理学会春季学術講演会, ３月１２日, ２０１５年, 神奈川

“有機薄膜への酸素の導入による Singlet-Triplet Annihilation の抑制”

4) 井上　棟智, 松島　敏則, 安達　千波矢

第７６回応用物理学会秋季学術講演会, ９月１４日, ２０１５年, 愛知

“有機レーザ色素の分子内緩和過程に関する研究”

Acknowledgements

The studies in this thesis were carried out at Adachi laboratory, Department of Chemistry and Biochemistry, Graduate School of Kyushu University from 2010-2015.

I am deeply grateful to Professor Chihaya Adachi for supervising this thesis, excellent experimental environment, helpful discussion, and exact comments and advice for all of my works. I am also deeply grateful to Professor Hiroyuki Furuta and Professor Yuji Oki for co-supervising of this thesis. I would also like to thank Associate Professor Toshinori Matsushima, Associate Professor Hajime Nakanotani, Assistant Professor Kenichi Goushi and Dr. William Potscavage. They also gave me useful advice and helped in preparing of my papers. Especially, Associate Professor Toshinori Matsushima helped in preparing this thesis. Assistant Professor Ryota Kabe also helped me in many discussion and the comments for the application of research funding. Prof. Takuma Yasuda, Dr. Juro Oshima, Dr. Toshihiro Oda, Dr. Junichi Nishide, Dr. Sandanayaka S. D. Atula, Associate Professor Jean-Charles Ribierre, Dr. Takashi Fujihara, Dr. Masayuki Yahiro, Assistant Professor Shuzo Hirata (Tokyo Institute of Technology), Dr. Shuho Tanimoto, Dr. Hiroki Uoyama, Dr. Youichi Tsuchiya, Mr. Takehiro Takahashi, Mr. Daisuke Goto, Mr. Masataka Mouri, Mr. Kou Inada, Mr. Masayuki Aonuma, Dr. Masaya Hirade, Dr. Yu Seok Yang, Dr. Jun Yun Kim, Dr. Sae Youn Lee, Mr. Hayato kakizoe, Mr. Kou Yoshida, Ms. Hyun Jung Seo, Ms. Miki Kamoto, Mr. Hwang Sun Bin, Ms. Keiko Kusuhara, Ms. Nozomi Nakamura, Ms. Sachiko Higashikawa, Ms. Rei Sasagawa, Ms. Mayumi Kudo, Ms. Hiromi Aizaki, Ms. Nao Onishi, Ms. Sayoko Otomo, Ms. Keiko Ohara, Ms. Yumi Oshima, Ms. Shono Makiko, Ms. Michiko Mouri, and Ms. Chihiro Nakanotani also helped me in experiments and daily life. I would like to acknowledge Ms. Hiroko Nomura for the synthesis of BSB-Cz, Dr. Takeshi Komino and Mr. Kuniaki Endo for calculation of confinement factor in waveguide, Dr Takashi Fujihara and Mr. Toshiya Yonehara for the measurement system for singlet-triplet annihilation and CW lasing, Dr. Tomas Serevičius for the helpful discussions and experiments in the whole of Chapter 2, Professor Katsumi Tokumaru, Assistant Professor Kenichi Goushi and Assistant Professor Katsuyuki Shizu (Kyoto University) for the advises and comments about the relationship between k_{RISC} and ΔE_{ST} in Chapter 5. I also acknowledge all the members of Adachi laboratory and all persons who I met through my works for their supports not only for my work but also my daily life. I would like to thank the Japan Society for the Promotion of Science for a grant and a fellowship that made it possible to complete this study. Finally, I would also like to express my gratitude to my family for their moral support and warm encouragements.

January, 2016 *Munetomo Inoue*